SPIDER ORB WEB, INVESTIGATING STRUCTURAL FEATURES AND USING BIOMIMICRY FOR LATTICE DESIGN

A DISSERTATION SUBMITTED TO
THE GRADUATE SCHOOL OF ENGINEERING AND SCIENCE
OF BİLKENT UNIVERSITY
IN PARTIAL FULFILLMENT OF THE REQUIREMENTS FOR
THE DEGREE OF
DOCTOR OF PHILOSOPHY
IN
MATERIALS SCIENCE AND NANOTECHNOLOGY

By
Koray Yavuz
December 2024

Spider Orb Web, Investigating structural features and using biomimicry for Lattice design

By Koray Yavuz

December 2024

We certify that we have read this dissertation and that in our opinion it is fully adequate, in scope and in quality, as a dissertation for the degree of Doctor of Philosophy.

Seymur Jahangirov(Advisor)

Recep Muhammet Görgülüarslan(Co-Advisor)

İlker Temizer

Aykut Erbaş

İrfan Kandemir

Erdem ACAR

Approved for the Graduate School of Engineering and Science:

Orhan Arıkan
Director of the Graduate School

ABSTRACT

SPIDER ORB WEB, INVESTIGATING STRUCTURAL FEATURES AND USING BIOMIMICRY FOR LATTICE DESIGN

Koray Yavuz
Ph.D. in Materials Science and Nanotechnology
Advisor: Seymur Jahangirov
December 2024

Spider orb web has evolved to fulfil multiple roles, such as catching prey and acting as a sensing tool. For orb-weavers, the web must stop and retain prey, which can fly into it with considerable momentum. Considering orb weaver spiders are mostly blind, the web must also transmit accurate information about the prey's location. There are many web features aiding these roles; some are known, and some are waiting to be shed light on. Considering these two cases, there are also two parts in this thesis, the first part is about a particular web-building behaviour of spiders and how it affects the signal transmittance, and the other is about creating a new lattice design for energy absorption utilizing some of the known structural characteristics of the spider web.

The first part of this study is about designing a new lattice (SW) for energy absorption inspired by the structure of spider webs. Spider orb web comprises four structural elements: anchor, frame, radial, and spiral threads. The first three are the main components that provide structural integrity. These components have a hierarchical nature; the anchors bind to the environment and are generally thickest, while radii form the innermost part with the thinnest threads. The frames make up the connection between the anchor and radii; thus, there is no direct connection between them, and they generally have a thickness value between the radii and anchor threads. These features help the spider orb web to be a resilient, efficient structure for energy absorption, so using the same properties, a 3D lattice was designed for energy absorption. This design is then optimized for improved Energy Absorption Efficiency(EAE) and Energy Absorption(EA) value.

The second part is about web-building behaviour that seems counterintuitive, heavier spiders increase the pretension of the threads as they get heavier, which diminishes the ability of the web to stop and retain prey. To investigate this

behaviour, a spider web model with controllable pretension is needed; thus, a pretension-adjusting algorithm has been developed. A realistic spider web model was created using non-linear material properties to describe the mechanical behaviour of the spider silk and web pretension values seen in nature. Using this model, different scenarios with changing spider weight and web pretension were simulated using a numerical method based on Solid Mechanics. Our results show that this behaviour is likely related to the signal transmittance on the spider web. Spider web evolved to withstand damaging environmental factors such as wind and rainfall while preserving its functionality for trapping prey. Understanding spider web structure could lead us to improve engineering designs by implementing similar resiliency. This thesis presents a study investigating spider webs and a biomimicking application inspired by spider web structure. So, while the two areas are different in the sense that one is closer to biology while the other is to mechanical engineering, they serve the same purpose: understanding how this structure, spider orb-web, functions and how we can take ideas from it.

Keywords: lattice structure, spider web, sensing, energy absorption, biomimicry.

ÖZET

ÖRÜMCEK DAIRESEL AĞININ YAPISAL ÖZELLIKLERININ ARAŞTIRILMASI VE KAFES TASARIMI IÇIN BIYOMIMIKRI KULLANILMASI ÜZERINE

Koray Yavuz
Malzeme Bilimi ve Nanoteknoloji, Doktora
Tez Danışmanı: Seymur Jahangirov
December 2024

Örümcek ağı, av yakalamak ve bir algılama aracı olarak kullanılmak gibi birden fazla rolü yerine getirmek için evrimleşmiştir. Örümcek ağı, önemli bir ivmeyle üzerine uçabilen bir avı durdurabilme özelliklerne sahip olmalıdır. Küre ağı örücü örümceklerin çoğunlukla kör olduğu düşünüldüğünde, ağın ayrıca avın nerede olduğu konusunda doğru bilgi iletmesi gerekir. Bu rollere yardımcı olan ağın bu işlevleri yerine getireblimesi için bir çok yapısal özellikleri bulunmaktadır, bu özelliklerin bazıları bilinmektedir ve bazıları da aydınlatılmayı beklemektedir. Bu durum göz önünde bulundurularak bu tezde iki bölüm bulunmaktadır. lk bölüm örümceklerin belirli bir ağ kurma davranışı ve bunun sinyal iletimini nasıl etkilediğiyle ilgilidir ve diğeri örümcek ağının bilinen yapısal özelliklerinden bazılarını kullanarak enerji emilimi için yeni bir kafes tasarımı oluşturmaktır.

Bu çalışmanın ilk bölümü, örümcek ağlarının yapısından esinlenerek enerji emilimi için yeni bir kafes (SW) tasarlamakla ilgilidir. Örümcek dairesel ağı, dört yapısal elemandan oluşur; çapa, çerçeve, radyal ve spiral iplikler ve ilk üçü yapısal bütünlüğü sağlayan ana bileşenlerdir. Bu bileşenler hiyerarşik bir yapıya sahiptir, ankrajlar ortama bağlanır ve genellikle en kalın bileşendir, radyal ise en ince ipliklerle en içteki kısmı oluşturur. Çerçeveler, ankraj ve yarıçaplar arasındaki bağlantıyı oluşturur, bu nedenle aralarında doğrudan bir bağlantı yoktur ve genellikle yarıçaplar ve ankraj iplikleri arasında bir kalınlık değerine sahiptir. Bu özellikler, örümcek dairesel ağının enerji emilimi için verimli olan dayanıklı bir yapı olmasına yardımcı olur, bu nedenle aynı özellikler kullanılarak enerji emilimi için bir kafes yapısı tasarlanmıştır. Bu tasarım daha sonra üstün Enerji Emilim Verimliliği (EAE) ve Enerji Emilimi (EA) değerine sahip olacak şekilde optimize edilmiştir.

İkinci bölüm, mantığa aykırı görünen bir ağ inşa etme davranışıyla ilgilidir,

örümceklerin ağırlığı arttıkça ipliklerin gerilimini artırır ve bu da ağın avları durdurma ve sabitleme yeteneğini azaltır. Bu davranışı araştırmak amacıyla gerilim değerleri kontrol edilebilir bir örümcek ağı modeline ihtiyaç vardır, bu nedenle bir gerilim ayarlama algoritması geliştirilmiştir. Örümcek ipeğinin mekanik davranışını ve doğada görülen ağ gerilme değerlerini tanımlamak için doğrusal olmayan malzeme özelliklerini kullanarak gerçekçi bir örümcek ağı modeli oluşturulmuştur. Bu model kullanılarak, Katı Mekanik'e dayalı bilişsel bir yöntem kullanılarak değişen örümcek ağırlığı ve ağ gerilme değerlerine sahip farklı senaryolar simüle edilmiştir. Sonuçlarımız, bu davranışın örümcek ağındaki sinyal iletimiyle ilişkili olma olasılığının yüksek olduğunu göstermektedir.

Örümcek ağı, avını yakalama işlevini korurken rüzgar ve yağmur gibi zararlı çevresel faktörlere dayanacak şekilde evrimleşmiştir. Örümcek ağının yapısını anlamak, benzer dayanıklılığı uygulayarak mühendislik tasarımlarını iyileştirmemizi sağlayabilir. Bu tezde hem örümcek ağının incelenmesi için bir çalışma hem de örümcek ağının yapısından esinlenen bir biyomimik uygulaması sunulmaktadır. Konuların birisinin biyolojiye, diğerinin ise makine mühendisliğine daha yakın olması nedeniyle farklı alanlar gibi görülebilir, ama bu iki konu da aynı amaca hizmet ediyor, bu amaç ise dairesel örümcek ağının nasıl işlediğini ve ondan nasıl fikir alabileceğimizi anlamaktır.

Anahtar sözcükler: kafes yapılar, örümcek ağı, algılama, enerji emilimi, biyotaklit.

Acknowledgement

This thesis first started with the idea of studying the spider's web-building process and utilizing it to create a design method for the additive manufacturing of lattice structures. However, I realized, there are many things in the web-making process that we do not know yet, and many parts of it need to be studied extensively. This research area is still in its early stages, and few people are working on it. The lattice structure research is also not done by many people in Türkiye, so finishing PhD became quite a challenge and I need to thank many people who were essential for its completion. First of all, I thank my parents. Without the safety net they created with hard work, I would be much less free to follow what I wanted. I would probably have given up on academia and would have chosen a profession with more "certainty" (which means government worker in Türkiye). I would like to thank Prof. Recep M. Görgülü Arslan which I can thank for basically saving my PhD by teaching me finite element analysis and guiding me on my lattice studies. I would also like to thank Prof. Ramón Eulalio Zaera Polo and Dr. Alejandro Mahy Soler Trujillo for their tremendous help with the biological spider web studies, also for their generosity with both their time and technical knowledge on the subject. I am very grateful to my advisor Prof. Seymur Jahangirov, whose encouragement and positivity kept me going, against all the indications that, to me, looked like I was failing. It was a joy working under him, and it felt more like working alongside him, really. I also would like to thank all of my friends, old and new, who make existence on this earth a joyful experience.

"Tradition is a set of solutions for which we have forgotten the problems. Throw away the solution and you get the problem back."
— Donald Kingsbury

Contents

1 Introduction **1**

1.0.1 Types of Cellular Structures . . . 3

1.0.2 Cellular Structures in nature . . . 5

1.0.3 Biomimickry . . . 5

2 Orb-Weaver Spiders and Their Web **9**

2.0.1 Spiders . . . 9

2.0.2 Spider Orb-web . . . 13

3 Finite Element Methods **18**

3.1 Introduction . . . 18

3.2 Continuum Mechanics . . . 19

3.3 Solid Mechanics . . . 19

3.4 Finite element analysis . . . 19

3.4.1 Static and Dynamic problems . . . 20

3.4.2 Implicit and Explicit methods . . . 20

3.4.3 Newmark-Beta Method . . . 21

3.4.4 Choosing a Solver . . . 24

3.5 Material Models for FEA . . . 24

3.5.1 Differing Measures for Stress and Strain . . . 24

3.5.2 Material Model for PLA . . . 27

3.5.3 Material Model for Ti-6Al-4V alloy . . . 29

3.5.4 Material Model for Spider Silk . . . 30

4 Spider Web Lattice **35**

4.1 Introduction . . . 35

4.2 Materials and Methods 37
4.2.1 Design Strategy 37
4.2.2 Energy Absorption Metrics 40
4.2.3 Finite Element Analysis 42
4.2.4 Experimental Tests 46
4.2.5 Optimization Formulation 46
4.2.6 Results for the PLA based SW Lattice 48
4.2.7 Ashby Map 57
4.2.8 Results for the Ti-6Al-4V based SW Lattice 59
4.2.9 Ashby Map 66
4.2.10 Conclusion 66

5 Effect of spider's weight on signal transmittance in vertical orb webs 68
5.0.1 Introduction 68
5.0.2 Spider Sense 69
5.0.3 Signal Transmittance on Spider Orb-Web 69
5.1 Methods and Models 71
5.1.1 Geometry of the orb web 71
5.1.2 Modeling the silk 72
5.1.3 Pretension procedure 73
5.1.4 Modeling the prey 75
5.2 Effect of spider's inertia and weight on signal transmission 75
5.3 Effect of spider's presence on the hub on signal transmission . . . 78
5.4 Conclusion 83

6 Conclusions and Future work 85

List of Figures

1.1 (a): An impressive catch for a small spider. I took the picture in Giresun, north-east of Turkiye however I don't know what species it is. (b): Spider sitting at its web's hub with wrapped prey. A photo by my friend Begun Erbaba, spider looks like a member of genus Argiope. 2

1.2 Different types of cellular structures are presented. (a) Kagome. (b) Octet truss. (c) MS1 lattice structure. (d) Stochastic foam. (e) Pillar textile. (f) Square collinear/cubic. (g) Re-entrant auxetic. (h) Spatially variant self-collimating lattice. (i) Body-centered cubic (BCC). (j) BCC with vertical strut in z-axis (BCCZ). (k) Face-centered cubic (FCC). (l) FCC with vertical strut in z-axis (FCCZ). (m) Octahedron. (n) Honeycomb. (o) Square. (p) Diamond. (q) TPMS P-type. (r) TPMS gyroid. (s) TPMS D-type. (t) TPMS I-WP type. Reprinted from ref.:[1] with permission. . . 4

1.3 Different types of cellular structures found in nature. (a) Human trabecular bone sgtructure. (b) Honeycomb. (c) Mushroom cap. (d) Stochastic structure of bubbles. (e) Dragonfly wing. (f) Leaf cross-section. Reprinted from ref.:[1] with permission. 6

1.4 Different organisms showing structural hierarchy, (a) Dead trees in the terraces of Mammoth Hot Springs [2]. The trunk is divided into branches with thickness getting smaller with each level. Similar hierarchy is found in (b) *Sialis lutaria* wing venation pattern [3] and (c) *Victoria amazonica* venation pattern [4]. 7

2.1 Different silk types that can be produced from a variety of glands. Reproduced by permission from ref. [5]. 11
2.2 Material properties of different silk types. Reproduced by permission from ref.: [6]. 12
2.3 A collection of different spider webs. Reproduced with permission from ref.:[7]. 13
2.4 Some of the terminology related with orbwebs are shown on diverse nephilid and araneid webs: Top left: *Nephila clavipes* web from Belize, top right: juvenile *Nephila pilipes* from Singapore, bottom left: *Argiope* spider from China, and bottom right:*Poltys* spider from China. Reproduced by permission from ref. [6]. 16
2.5 Web building steps of *Araneus Diadematus*, reproduced from ref.: [8]. 17

3.1 Generalized graph for the stress-strain graph of a dog specimen of a material. 27
3.2 Generalized graph for the stress-strain graph of a dog specimen of a material. 28
3.3 A simplified model for the dragline silk of the spider is shown at (a). A more schematic version is shown on the right, with variation among the amorphous chains are not shown. The dotted lines are the hydrogen bonds, and individual bonds have been replaced by "overall" bonds, with a regular bonding between its neighbours. Figure reproduced by permission from ref.: [9] 31
3.4 Stress strain graph for the Major Ampullate and the Flagelliform silk, showing the loading and unloading behaviour of the material model used in our work, also in [10]. 34

4.1 (a) Main structural elements of a spider orb web of Cyclosa Caroli is shown. Anchor threads (Anc) attach to the surrounding vegetation and connects to frame threads (Fr). Radii (Rad) radiates from hub to frame threads thus there is no direct link to anchor threads. Capture spirals (Cap) are connected to radii. Redrawn with permission, after Hesselberg (2015). (b) 2D design scheme of SW-p lattice is shown which is the view from the top of the 3D lattice. Anchor struts are connected to frame struts which connect to radii with no direct link between radii and anchors. L_a, L_f and L_r are defined as the length from the hub to corner of the unit cell, corner of the frame struts and corner of the radii struts respectively. Then two geometric parameters are defined as their ratios, $fr2an = L_f/L_a$ and $ra2fr = L_r/L_f$ which adjusts the anchor strut length and convexity of the frame struts respectively. (c) The resulting shapes with changing fr2an and ra2fr values are shown. 39
4.2 An exemplary stress-strain curve for compression test. 42
4.3 Lattice meshed by beam elements of different lengths in Abaqus; colours on the beam show the effective thickness taken by the Abaqus in order to calculate the thickness at contact points. Image used by permission from ref.:[11] 44
4.4 Compression test set up. 46
4.5 Representation of FE model with boundary conditions used in optimization scheme. 49
4.6 Mesh convergence analysis for (a) beam elements and (b) 3D tetrahedral elements. 50
4.7 (a) Pareto front generated by the optimization [12], the chosen structure is shown with red dot. (b) Unit cell of the chosen structure, with parameters $rad2fr$: 0.95, $fr2an$: 0.85, $r_{af} = 0.65$, $r_{fr} = 0.80$. The results are for SW lattice made from PLA material. 51

4.8 (a) FEA result utilizing beam elements, showing 3^{rd}, 4^{th}, 5^{th}, and 6^{th} options from the Pareto front (Fig 4.7), (b) FEA result utilizing 3D tetrahedral elements with damage model, for the 3^{rd} and 6^{th} options. 52
4.9 Difference in stress-strain behaviour of simulations done with beam and 3D tetrahedral elements. 53
4.10 Difference in stress-strain behaviour of simulations done with 3D tetrahedral elements, with and without damage model. Linear perturbation simulation shows the elastic modulus of the SW lattice simulations. 54
4.11 Comparison between the compression behaviour of three manufactured samples, and 3D simulation using damage model. 55
4.12 Comparison of the stress-strain curves of different simulations and the experiment. 55
4.13 Mechanical properties of the SW-lattice, with stress-strain graph(blue) and energy efficiency graph (red) shown in (a). Cumulative energy absorption versus stress curve is shown in (b). . . 56
4.14 Comparison of deformation modes between 3D simulation with damage model and experimental tests. 58
4.15 Comparison of mechanical properties of the proposed SW lattice with other architected infill materials presented in literature. . . . 59
4.16 Experimental validation of the numerical simulations. The data of the experiment were shared by Prof. Mustafa Guden, which we are thankful for. 60
4.17 Comparison of the deformation modes between the experiment and simulation. Experiment pictures are from ref:[13], reprinted with permission. 61
4.18 (a) Pareto front generated by the optimization [12], the chosen structure is shown with red dot. (b) Unit cell of the chosen structure, with parameters $rad2fr$: 0.86, $fr2an$: 0.66, $r_{af} = 0.87$, $r_{fr} = 0.81$. The results are for SW lattice using material property of Ti-6Al-4V alloy manufactured with EBM. 61

4.19 Results of the compression behaviour of 3^{rd}, 4^{th}, and 5^{th}, Pareto options. 62
4.20 Results of the compression behaviour of optimized SW lattice with (a) stress-strain curve and energy efficiency curve and (b) cumulative energy absorption versus stress curve. 63
4.21 Comparison of the stress-strain curves of the SW lattice and four other conventional lattices. 64
4.22 Comparison of mechanical properties between the SW lattice and four other conventional lattices are shown for (a) Energy absorption capacity and (b) energy absorption efficiency. 65
4.23 Comparison of energy absorption capacity of the designed SW lattice with other lattices reported in previous studies. 66
4.24 Optimized SW structure for (a):PLA and (b):Ti-6Al-4V. 67

5.1 Spider web model used in this study with geometrical parameters. Solid cyan lines show possible positions where the spider can detect incoming signals which are called leg nodes. A fly can be captured at any point on the solid magenta line which is called a signal node. 72
5.2 Tension adjustment algorithm flowchart. 74
5.3 Displacements and tension change values near the hub, shown by the red and blue colours respectively, caused by the signal source located at the red dot. Web's response to transverse excitation is shown at (i), to longitudinal excitation at (ii) and to lateral excitation at (iii). In the case of (a), no mass or weight force caused by the spider is applied to anywhere in the system. (b) shows spider web with 490 μN downward force applied to the hub but no inertia and (c) 50 mg spider at the hub. For transverse waves tension change on the radii are tens of nano newtons at maximum, and do not show any significant change for different cases. The displacement is affected by addition of inertia and positional information for the signal location becomes significantly better compared to no inertia case. Similar observations are present for the tension change values due to the lateral and longitudinal waves. 77

5.4 Prestresses in the web with $T_{rad} = 100\ \mu N$, (a) no spider present at the hub, (b) 490 μN and (c) 980 μN weight applied at the web centre, representing two different spider's weight in y direction. The numbers present the pretension values of radii close to the frame. All the values shown including the colorbar have units of μN. 79

5.5 Average displacement and tension change of leg nodes on two radii closest to the signal location is shown with changing spider mass for $T_{rad} = 100\ \mu N$. The signal source is located at the bottom region, shown by the red dot on the spider web model (a), and the wave type of the vibration are transverse, longitudinal and lateral for (b), (c), (d) respectively. For transverse waves the displacement decreases as the mass of the spider increases. For lateral and longitudinal cases tension change is not observable for 75 mg and 100 mg cases and the increase in displacement comes from the silk that sags, and is not under any tension. 80

5.6 Contour map of signal amplitude with respect to the spider weight and radii pretension (T_{rad}) for the vibration generated at the bottom part of the web, with white lines showing the equivalue points. Three points on the map are shown as web models. The signal source is shown as the red dot and the displacements on the radii are shown with red solid lines, where a larger distance from the hub represent larger value on the radial. 81

5.7 Contour maps for (a) longitudinal and (b) lateral waves. The signal amplitude is represented as tension change on radii, with colorbar representing the values with units of μN, plotted with respect to spider weight and radii pretension (T_{rad}). Model representation corresponding to the areas marked on the contour map are shown below, (c) for longitudinal and (d) for lateral waves. The signal source is shown as the red dot and the tension change on the radii are shown with blue solid lines, with greater distance from the hub representing a larger amplitude. The signal amplitude created by the longitudinal waves do not seem to change much with changing tension (a), however as the tension on the radii becomes too low the signal is completely lost. Lateral waves also lose signal transmission below a certain (radii tension)/(spider weight) ratio threshold as seen in (b). Unlike the longitudinal excitation, for the lateral excitation case, higher tension of the radii affects signal transmission negatively, and the locational information becomes less precise above a certain value. 82

List of Tables

4.1 Material properties of PLA. 45
4.2 Johnson–Cook plasticity and damage model parameters from [13]. 45
4.3 Experimental Result of the optimized SW-lattice manufactured with PLA material 57

5.1 Pretension values and diameter of the threads in the model. . . . 74

Chapter 1

Introduction

For both scientists and engineers, looking at the organisms in nature should cause a familiar yet elusive reaction: why are things the way they are? Why are trees shaped like trees? Why do bees do not fly straight? Why are mud crack shapes similar to leaf venation shapes? These questions can teach us something profound about how the world works. However, it is very easy to brush them off with slightly less interesting questions about the intricacies of how(not why) evolution led them there or how you can use them for graphene research. Hopefully, in this thesis, I can provide a fascinating insight into one of the 'why' questions that can come to your mind while looking at nature and will show one way we took inspiration from it. The leading role for this mission is the spider orb-web.

Spider orb web is a highly efficient prey-capturing net that also acts as a sensing tool for the spider. For the web to be an efficient sensing tool, it should serve two purposes: detecting and locating the prey, and for it to be an effective trap, it should absorb the prey's kinetic energy while being resilient to damage. For these purposes, spider silk and its properties are studied extensively, and the research shows that it indeed has impressive properties, such as very high extensibility and excellent strength. Its toughness, which measures how much energy a material can absorb per volume, exceeds that of the best synthetic products humans can craft, including steel and Kevlar [14]. However its structure also contributes to

the durability and resilience of the spider web. For example, the framing used in spider orb webs allows the web to endure higher loads and impacts [10].

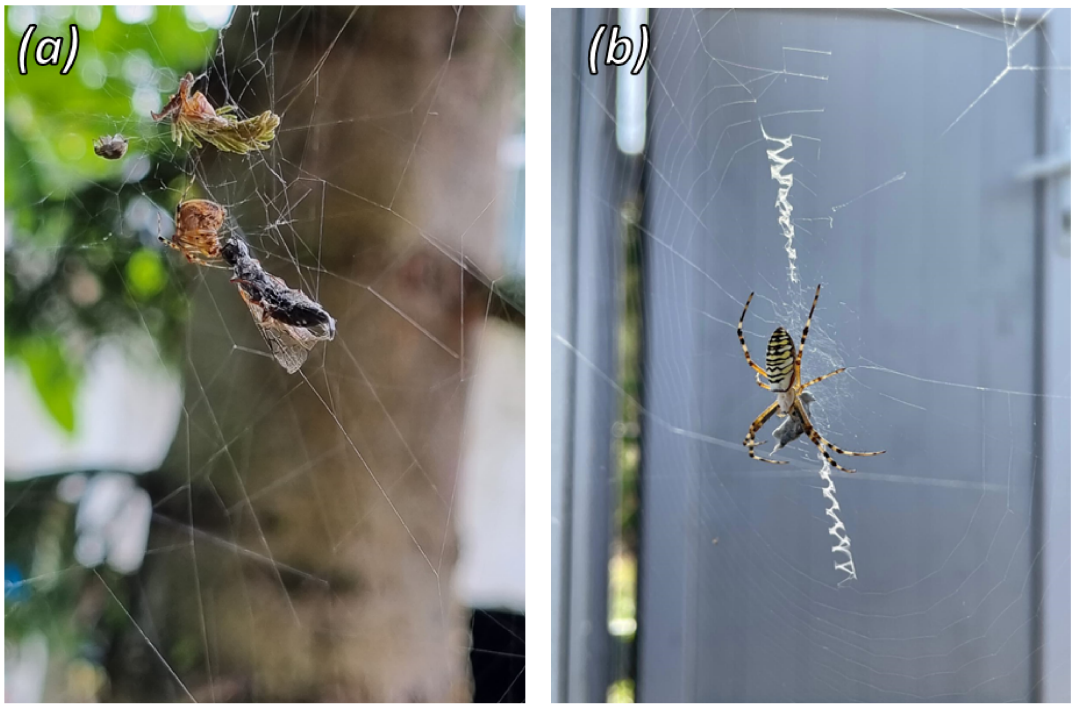


Figure 1.1: (a): An impressive catch for a small spider. I took the picture in Giresun, north-east of Turkiye however I don't know what species it is. (b): Spider sitting at its web's hub with wrapped prey. A photo by my friend Begun Erbaba, spider looks like a member of genus Argiope.

However, there is not as much data as a computational researcher might hope; there are very few studies on the structural "numbers", such as the tension or thickness of each thread. Furthermore, some of the observations made for the spider web structure are not answered in a physical sense, such as spiders' tendency to increase the tension when wind is present or when its weight is increased[15, 16].

Why are these questions important? If we can learn more about this resilient structure, I believe we can start to understand the behavioural web-building process of spiders, which can help us create more resilient structures that are very hard to create with the current techniques [17]. However, without even going that further, there might be design inspirations we can take for applications such as cellular structures.

Cellular structures are used widely in modern industries. Metallic and polymer foams, which are types of cellular structures, find extensive use in aircraft and automotive industries, along with fields such as biomechanics [18]. This prevalence is because of their extraordinary properties; they can have comparable strength and other mechanical properties to conventional structural materials while being lightweight. Cellular structures can be made into sandwich panels or designed to be used as energy absorbers, so they can also be used as crash elements. With the developments in additive manufacturing, it is possible to create complex structures that were impossible with conventional techniques [19]. This feature allows high design flexibility, which allows optimization for different applications. Thus, there is an increased research interest in designs with improved stiffness, strength, heat exchange or energy absorption properties.

1.0.1 Types of Cellular Structures

Foams are not the only type of cellular structure; they are part of the category called stochastic cellular structures. These structures can be made with techniques such as using foaming agents or bubbling gas inside the molten material [20]. With these types of processes, random empty spaces occur inside the material, making the structure "stochastic". These structures can then be used for applications such as acoustic or thermal insulators, vibration absorbers, mechanical dampers, etc. Non-stochastic structures have some kind of periodic architecture, which can be made out of truss-strut assemblies, which are referred to as lattice materials, or they can have two-dimensional periodic walls, which then be called prismatic structures [21]. Compared to their stochastic analogues, non-stochastic structures generally have superior mechanical properties at the same relative density or weight [21]. However, manufacturing them can be more expensive. A collection of different types of cellular structures is shown in Fig.1.2.

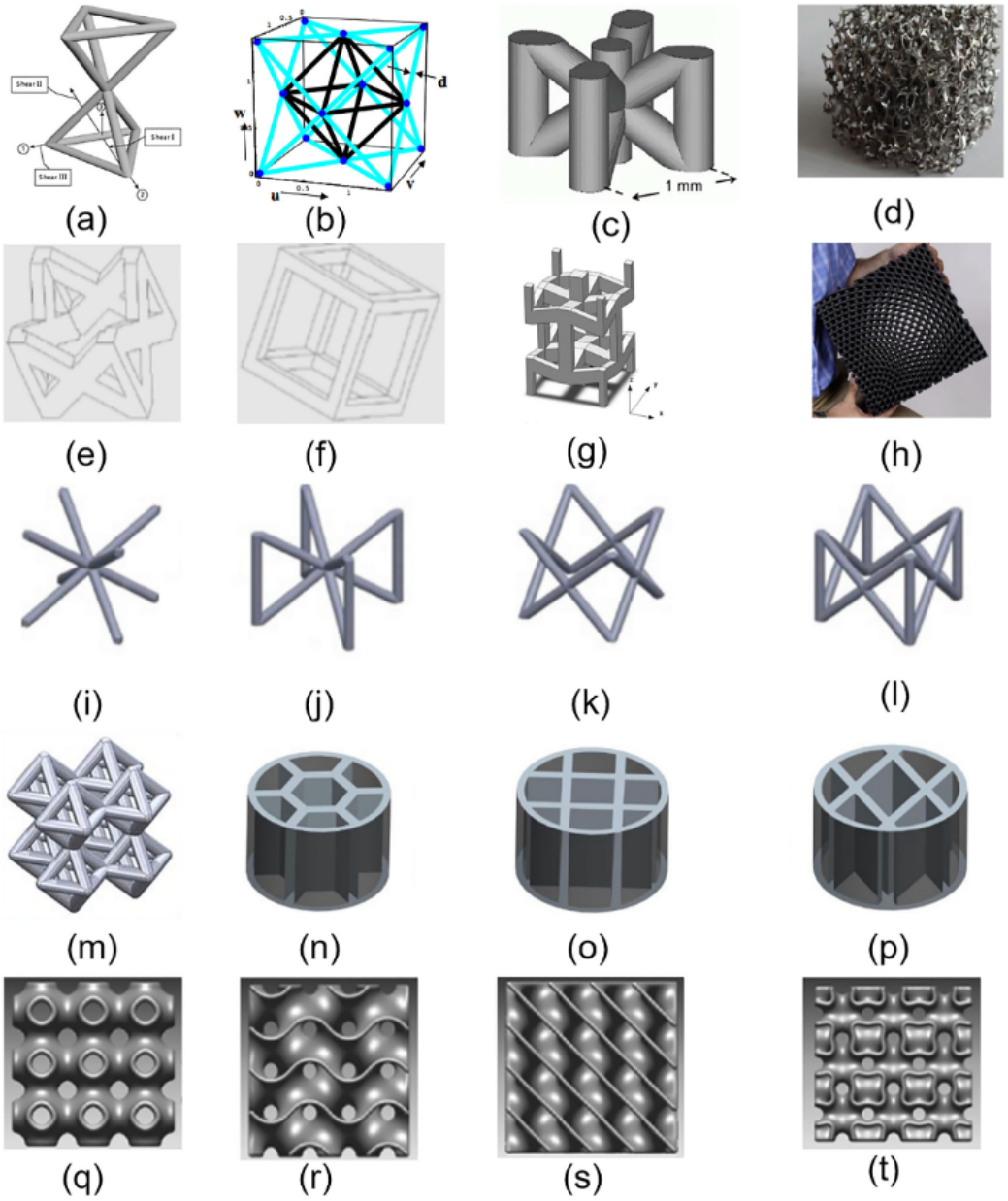


Figure 1.2: Different types of cellular structures are presented. (a) Kagome. (b) Octet truss. (c) MS1 lattice structure. (d) Stochastic foam. (e) Pillar textile. (f) Square collinear/cubic. (g) Re-entrant auxetic. (h) Spatially variant self-collimating lattice. (i) Body-centered cubic (BCC). (j) BCC with vertical strut in z-axis (BCCZ). (k) Face-centered cubic (FCC). (l) FCC with vertical strut in z-axis (FCCZ). (m) Octahedron. (n) Honeycomb. (o) Square. (p) Diamond. (q) TPMS P-type. (r) TPMS gyroid. (s) TPMS D-type. (t) TPMS I-WP type. Reprinted from ref.:[1] with permission.

1.0.2 Cellular Structures in nature

Nature is always an inspiration for scientists and engineers, and for designing cellular structures, it is very common to look at nature. For example, conventional strut-based lattices such as body-centred cubic (BCC), face-centred cubic (FCC) and simple cubic (SC) are all types of crystal structures found in solids, and they became some of the most well-known structures in the community. Apart from the inorganic materials, organisms can also possess cellular structures, which have evolved for various roles the organism might need.

Cellular structures are everywhere in nature, from the trabecular bone structure to bird beaks, from leaf venation to wood cross sections; nature optimizes the structural integrity of its parts by using the minimum amount of material to do its job most efficiently. A popular quote from Prof. Julian Vincent points to this phenomenon, "in nature, material is expensive, and shape is cheap".

While many of these structures are quite detailed, and there is still much to learn about how they form, however, we can still study these structures and carry some features into our designs. This methodology of taking design inspiration from nature and implementing it in an application is called biomimicry.

1.0.3 Biomimickry

Biological organisms have to adapt to changing environments, the ones that cannot, will perish. This makes nature one of the best sources to steal ideas since, generally, the ones with the best solutions get to live, and those are the ones we get to know about (...of course there are also fossils, but the information you can extract from them is limited). Of course, the fields that can use this methodology include cellular structures. In the literature, some of the structures that inspired scientists can be counted are the beetle elytra [22], cuttlefish bone [23] and luffa sponge [24].

Taking geometrical inspiration is a part of biomimicry. However, we also

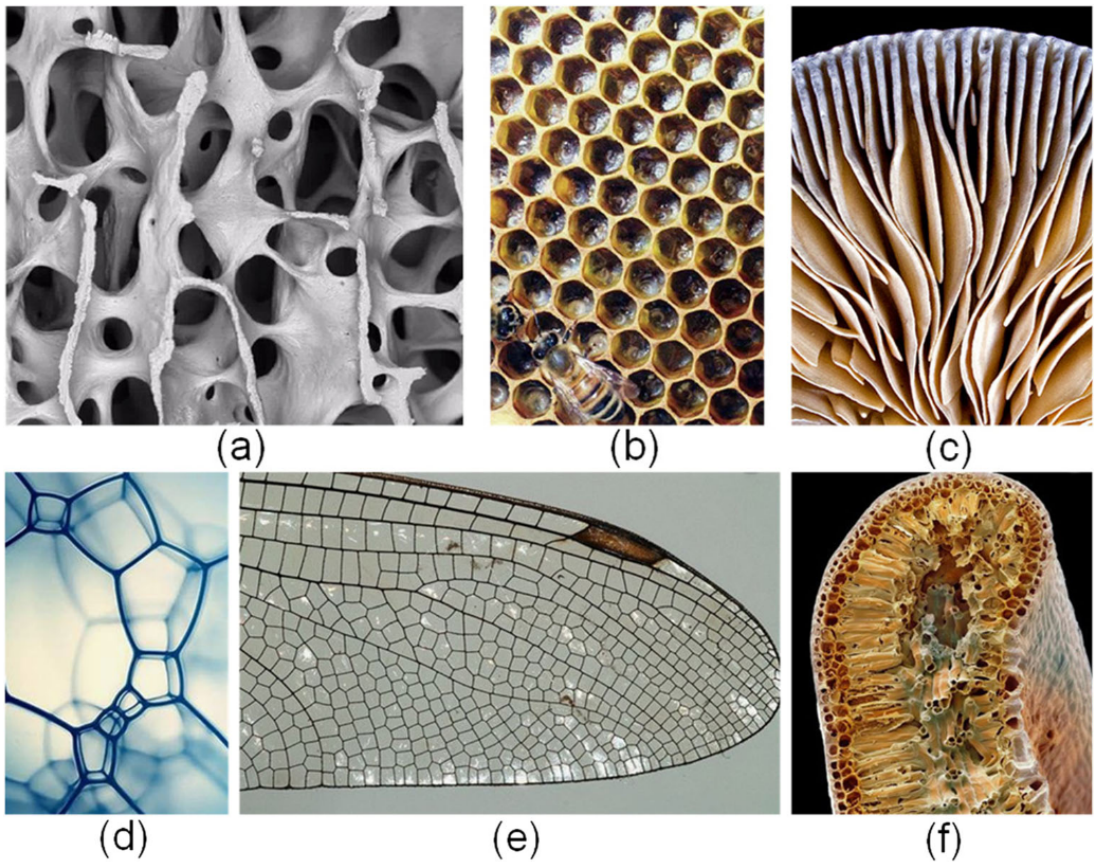


Figure 1.3: Different types of cellular structures found in nature. (a) Human trabecular bone sgtructure. (b) Honeycomb. (c) Mushroom cap. (d) Stochastic structure of bubbles. (e) Dragonfly wing. (f) Leaf cross-section. Reprinted from ref.:[1] with permission.

wanted to take ideas from it, and a ubiquitous architectural concept found in nature is hierarchical structures, where the different parts have different thickness/stiffness in order to have better stress sharing between the components. Examples of this kind of strategy can be seen in Fig.1.4. Spider orb-web also possesses a similar hierarchy.



Figure 1.4: Different organisms showing structural hierarchy, (a) Dead trees in the terraces of Mammoth Hot Springs [2]. The trunk is divided into branches with thickness getting smaller with each level. Similar hierarchy is found in (b) *Sialis lutaria* wing venation pattern [3] and (c) *Victoria amazonica* venation pattern [4].

Spider orb-web has evolved to absorb the energy of impacting prey along with other modifications that help the spider to catch and retain prey. As we will discuss in more detail in the relevant chapters, the spider orb-web's hierarchical structure, with its ordered tension, thickness, and connectivity differences between different thread groups, might help absorb the kinetic energy of the impacting prey. In one of our projects, we designed an infill lattice structure with a similar hierarchy inspired by spider orb webs.

We also studied an observation made on spider orb-webs, mainly the tension and spider's weight having a direct correlation. This means that the tension of the threads increases as the spider's weight increases, for a reason that was not explained with structural arguments before, to our knowledge.

While these two projects might be perceived as very different, we have used similar techniques, such as finite element analysis, and we used the knowledge we get from the spider orb-webs in both cases. Moreover, both of these projects serve our main quest: to better understand this biological structure that evolved for millions of years for two important objectives: capturing prey and being a

sensing tool.

This thesis consists of 6 chapters. The second chapter will give brief general information about spiders and the spider orb web. Then, the tools and models used in our projects will be presented, which can be considered a rough manual on dynamic finite element analysis and material models used in our projects. Next, we will present our new lattice design inspired by spider orb webs. Chapter 5 presents our answer to the question that was presented in the above paragraphs, "Why do heavier spiders increase the tension of their webs?". Lastly, the overall conclusions of the doctoral thesis and planned future work will be presented.

Chapter 2

Orb-Weaver Spiders and Their Web

2.0.1 Spiders

Spiders are Arthropods, from the class of Arachnida, which has the meaning of spider in Greek; however, species such as scorpions and ticks are also included in this class. Spiders, as we know them, from tarantulas with their distinguishing hairs to garden spiders with their elaborate web designs, are from the order Araneae. The word Araneae again means spider, but this time in Latin. As of writing these lines, order Araneae consists of 52338 different species [25], which makes them among the most diverse animal lineages.

Like other Anthropopods, spiders have an exoskeleton made of chitin. However, they are easy to distinguish from other insects because they lack antennae and have two segments or "tagmata" instead of three. The frontal tagma (singular of tagmata) is named prosoma (cephalothorax) and is connected via a stalk-like pedicle to the opisthosoma (abdomen). Prosoma hosts the central nervous system and is responsible for nervous integration. The eyes, mouth and a pair of chelicerae are all attached to the prosoma, along with four pairs of legs. Opisthosoma has a sack-like appearance and is mainly responsible for vegetative

functions, such as digestion, respiration, circulation and silk production [26]. Silk-producing organs are located at the rear end of the opisthosoma and are called spinnerets [27].

All spiders produce silk, which can be used for different purposes, from building capture webs to making egg sacs. Most spiders have three pairs of functioning spinnerets, such as Araneomorphae spiders, which Araneus Diadematus is a part of [28]. The silk produced by the spider is known as a marvellous material that is stronger than steel and is able to withstand larger strains than nylon. This thesis focuses on the structures made with spider silk, so a brief discussion of its properties is necessary.

2.0.1.1 Spider Silk

Spider silks are made up of proteins, and nearly all have evolved from a single ancestral "spidroin" gene [27]. Through evolution, there are many different types of silk produced from at least ten different types of glands. When biologists talk about spider silk, they might include all of the different secretions from these organs, even though any other scientist from another field, like material science, would not recognize them as silk, which can behave more like a liquid rather than a proper elastic solid. Since all of the spinneret organs are homologous, in the biological context, they are all considered spider silk [29].

One typical example of the not-so-silk-like secretion from the spinnerets is the organic adhesive that forms droplets on the capture spiral of Araneid and Tetragnathid orb weavers, which is produced by the Aggregate glands of the spider. These sticky droplets cover the sticky spirals of araneoids, which are produced from the Flagelliform glands. Dragline silk that the spiders use as a safety line is produced from Major-ampullate glands; also, the anchor and the frames of the recognizable orb webs use the silk from the same source. However, the radii of the orb-webs usually contain Major ampullate silk along with Minor ampullate silk [27]. When spider silk is mentioned in popular culture and about its strength and marvellous characteristics, they usually mean Major-ampullate

silk. It is a very strong material; for example, its strength-to-weight ratio is 5 times greater than steel [30]. Dragline silk from Darwin's bark spider (*Caerostris darwini*) can reach up to 520 Mj/m^3, which is 10 times larger than Kevlar® [31]. Some other types of silk of orb-weavers are as follows: piriform, aciniform, and tubuliform. Piriform silk is used to bind the anchor threads to the environment. Aciniform silk is used for wrapping prey and making stabilimentum (web decorations). Tubuliform silk is used to cover spider eggs, which protects them from damage [6].

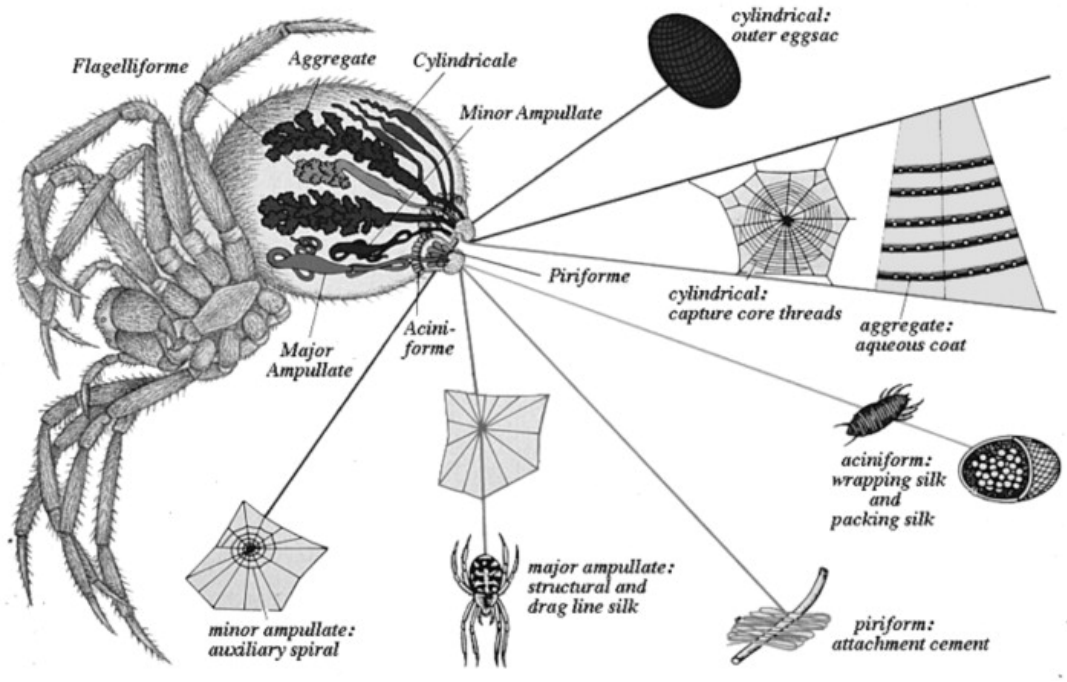


Figure 2.1: Different silk types that can be produced from a variety of glands. Reproduced by permission from ref. [5].

Spider silk has non-linear material properties and behaves differently than conventional materials. When a tensile force is applied, conventional materials have a constant stiffness at the elastic region, and after the yield point, stiffness decreases gradually. For spider silk, there is still a softening at the yield point, but at higher strain, there is substantial stiffening. This phenomenon makes the spider web more resilient to damage, as it provides better resistance to structural defects compared to conventional material behaviour and helps to preserve the web's structural integrity under loads such as wind [32]. This type of response under

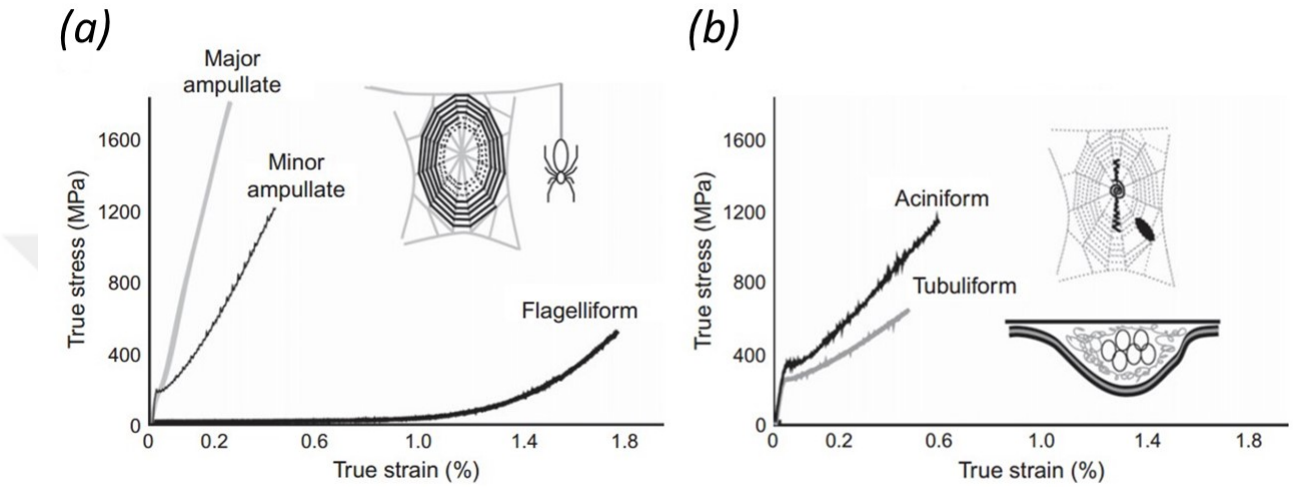
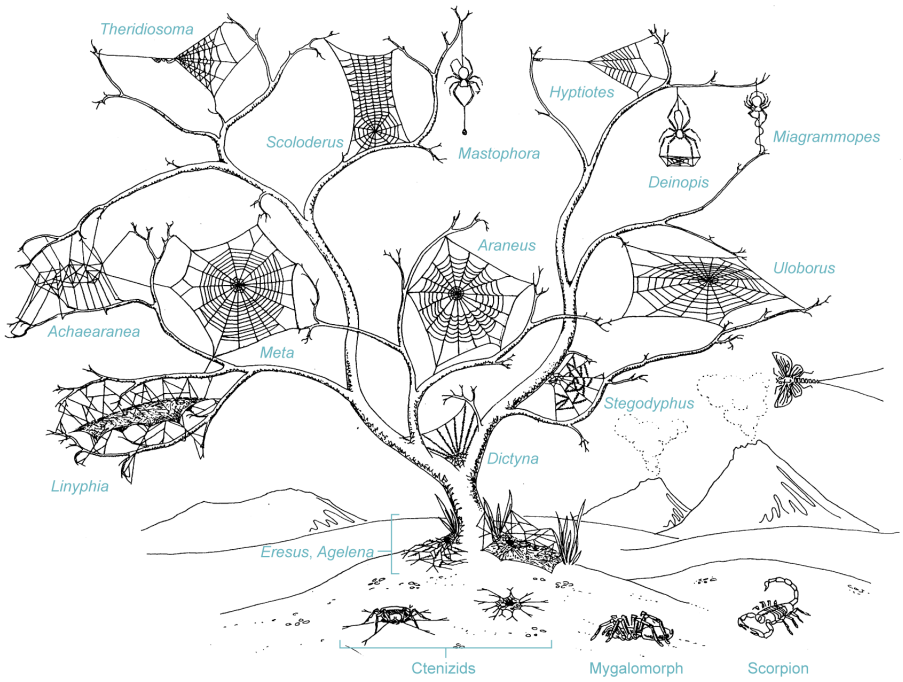


Figure 2.2: Material properties of different silk types. Reproduced by permission from ref.: [6].

stress is the result of the relation between two different structural parts in the silk; one is made up of amorphous proteins, and the other is crystallized protein structures called β-sheets. which can be characterized by the microstructure-based continuum model proposed by De Tomassi et al. (2010) [33]. This model considers the silk to have two basic parts, a hard and a soft fraction. The soft fraction refers to the amorphous network of proteins. The hard fraction refers to the ordered network that is rich in stiff crystals formed with hydrogen bonds, and they are made up of polyalanine sequences arranged in β-sheets. As the silk protein chain is stretched beyond a specific limit, the hydrogen bonds of the hard fraction start to unravel, thus turning into a soft fraction in the process. This makes the spider silk have the mentioned unusual response to stress; as the crystals unravel the contour length increases, so the silk can stretch more before failing. In the next part, we will talk about the interesting structures spiders can make using this material.

2.0.2 Spider Orb-web



Vollrath F, Selden P. 2007.
Annu. Rev. Ecol. Evol. Syst. 38:819–46

Figure 2.3: A collection of different spider webs. Reproduced with permission from ref.:[7].

Probably the most well-known aspect of spider behaviour is the web making. While the most recognizable form of the web is the orb-web, not all spiders make webs, such as wolf spiders(Lycosoid), and some of the webs are quite different from the orbweb, which can include the sheet web of linyphiidae or tangle web of theridiidae. Some of the different web types can be seen in Fig.2.3. This thesis focuses on spider orb webs, the main reason being that they are the most studied web structurally; however, in the future, many other mysteries of the behaviour of spider web-making can be uncovered by studying other types of webs as well. At this point in time, we are not aware of how the web-making algorithm of the spiders relates to each other, but before reaching that point, there are many things to learn about the orb web itself, even if it is the most studied type. So, in this section, I will talk about some of the aspects of the orb-web structure and the web-spinning behaviour.

2.0.2.1 Structural Elements of Spider Orb-web

In the previous section, the dragline silk and its extraordinary properties were discussed. The main structural framework of the spider orb-webs is close to the dragline silk and can be divided into three parts: the anchor, frame and radial threads. They are made by major and minor ampullate glands, but the contribution of each type and the thickness of the bundles made vary a lot; such variations of silk making are not well understood [34]. In a study by Peters et al. (1991), nine different radii from three mature female Araneus diadematus spiders were analyzed, and two of them only had major ampullate strands while the other seven were a combination of both [27]. Silk from the ampullate glands provides the main structural support for the spider web and absorbs most of the prey's kinetic energy [35]. After the prey is stopped, it must also stay put, i.e. not fall to the environment or free itself. This goal is achieved by the capture spiral or sticky spiral. These spirals can be spun by sticky silk from cribellum glands for the cribellate spiders(mixed with minor ampullate) or non-sticky silk from flagelliform glands and then covered by sticky droplets that are made by aggregate glands for araneoid spiders [27]. Compared to the ampullate silks, capture spirals are much more extensible (Fig.2.2).

2.0.2.2 Building steps and the Architecture of the Orb-web

Spider orb-web building is thought to have a monophyletic origin and thus shares some similar patterns. Spider first lays a bridge line and then creates a proto-hub where the threads that connect to the environment come together. After adjusting the position of the hub, the spider lays the frame and the other radii threads. After this framework is done, starting from the hub, the auxiliary spiral is laid, which acts as a support and physical guide for the sticky spiral. In many species, this spiral is removed; however, some species such as *Nephilidae* preserve them [36]. The last step is the laying of the sticky spiral. Web building steps of *Araneus Diadematus* spider can be seen from Fig.2.5.

Every spider web is different, and structural differences can be observed even when they are made by the same spider. However, some common structural features can be observed. The first one is how the framework is laid, with a thicker and stronger anchor thread lying outside and not directly attached to the radii. Instead, they are connected via the frame threads, which are thicker than radii and generally thinner than the anchors.

This separation between the anchors and the radii helps with acquired damage to the web, not resulting in catastrophic failure [37]. This way, a hierarchical support system happens in the web, which makes the web structurally more resilient, and it helps the web to be able to absorb more energy, thus helping to catch heavier prey [10]. Inspired by this web-building behaviour, I have designed an infill lattice that has promising energy absorption capabilities, which is discussed in Chapter 4.

Another aspect of the spider web structure is the asymmetry, where heavier spiders build webs with larger asymmetry [38],[39]. The web asymmetry refers to the difference between the bottom and the top areas of the web. This is thought to be created by the running speed difference of the heavier spiders, which run faster to the bottom compared to the top. Thus by placing the web hub, where the spider generally rests, to an upper position, it optimizes the time to reach every point of the edge. Along with asymmetry, there is another aspect of the spider web that strongly correlates with the change in the spider's weight, which is the observed increase in tension. This phenomenon is observed in vertical orb-web weavers, such as *Araneus Diadematus* or *Nephila Clavipes*. Wirth et al. observed that the ratio of spider's mass to radial force was largely the same for the same species and even had the same order of magnitude for different species [16]. This is an interesting and unexpected behaviour, as higher tension would make the web more prone to damage by prey impact [40], [41]. We claim this behaviour is due to spiders instinctively optimizing the web for signal transmission, as we will discuss in Chapter 5.

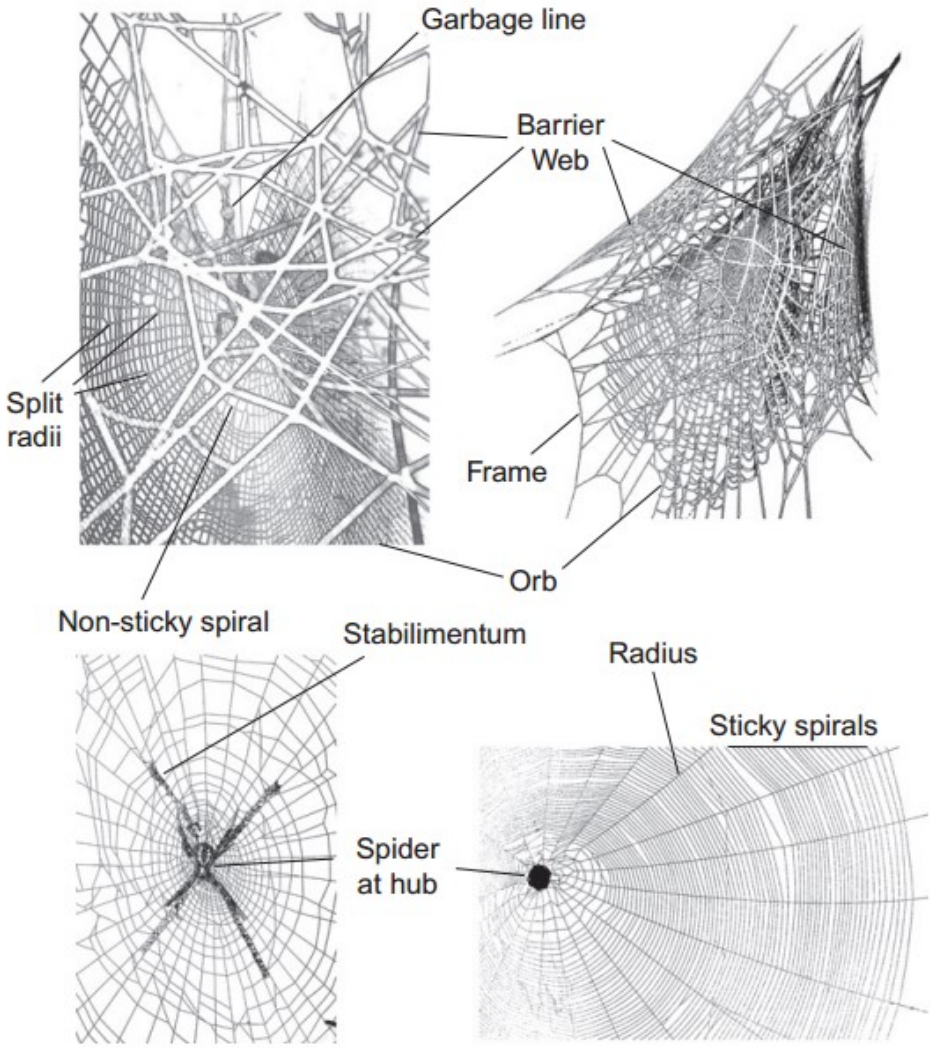


Figure 2.4: Some of the terminology related with orbwebs are shown on diverse nephilid and araneid webs: Top left: *Nephila clavipes* web from Belize, top right: juvenile *Nephila pilipes* from Singapore, bottom left: *Argiope* spider from China, and bottom right:*Poltys* spider from China. Reproduced by permission from ref. [6].

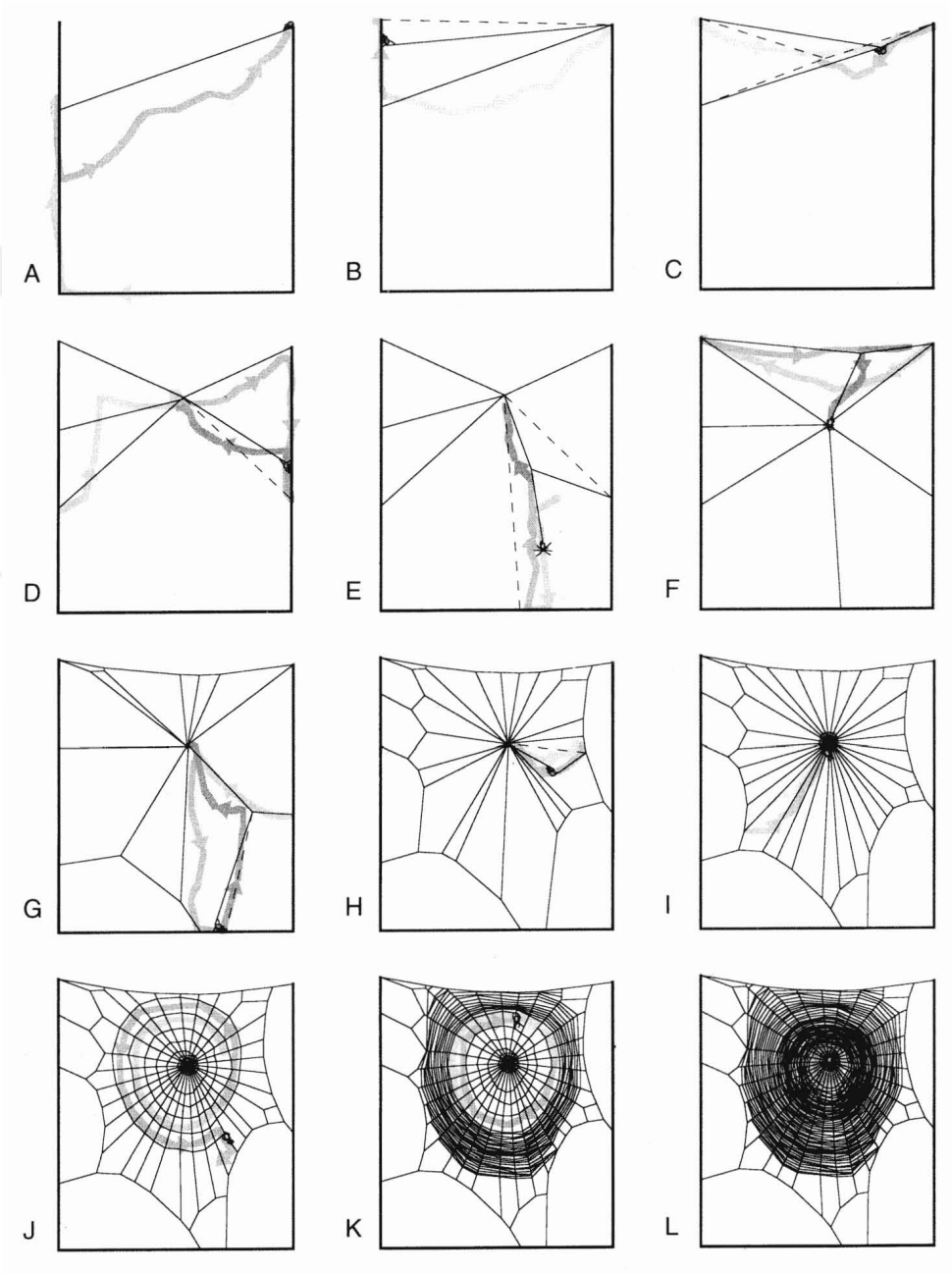


Figure 2.5: Web building steps of *Araneus Diadematus*, reproduced from ref.: [8].

Chapter 3

Finite Element Methods

3.1 Introduction

This thesis is mainly about trying to understand spider web structure with the limited scope of the time and effort allowed. Understanding goes both ways: being able to recognize the reasoning behind certain structural features and being able to use such features in order to improve the capabilities of human-made designs. For both of these challenges, I have used the computational finite element method. This technique provides us with simulations for deformable solids, which can have very high strains and non-linear material models, and it is helpful to the point that it becomes necessary. So, it deserves a brief chapter of its own to familiarize the reader with the main tool utilized in the rest of the thesis. I will briefly write about the parent subjects of finite element analysis. After that, I will discuss the calculations behind the scenes of a finite element analysis tool such as Abaqus that we used for our projects. This will involve a basic understanding of the algorithms for dynamic simulations and the material models used in our simulations to describe the behaviour of solids. Lastly, I will briefly talk about the mesh elements used.

3.2 Continuum Mechanics

Continuum mechanics is the study of certain materials' mechanical behaviour and kinematics that can be considered as a continuous medium or continuum. A continuous medium can be made up of solids, liquid or gas and fills the body it occupies. At macro scales, we can neglect that these materials are made up of discrete parts. These discrete parts can be exemplified as atoms for every material, pores and air bubbles in the case of concrete, or grain boundaries in the case of steel. Neglecting these discrepancies can create a framework that explains material behaviour sufficiently at the macro scale.

Continuum mechanics rely heavily on solving differential equations. These differential equations are called constitutive equations and can be specific to a particular material. Some of them are more general, and they are the result of fundamental physical laws. The continuity equation and equations of motion and equilibrium can be listed as examples, which are based on conservation of mass and conservation of momentum [42].

3.3 Solid Mechanics

Solid mechanics is a subcategory of Continuum mechanics, which only deals with solid materials and their behaviour. Many branches of science and engineering utilize this field extensively. Applications such as earthquake prediction made by geophysicists, designing implants for knee joints or designing cars with better crash-worthiness are all a part of this field.

3.4 Finite element analysis

The bread and butter of this thesis is finite element analysis. While it is very easy to be lost in the practicalities of a commercial software, it is important to

understand what we are actually calculating. This chapter is largely a compilation of the sources: Applied Solid Mechanics by [43] and Abaqus manuals [44, 45, 46]; which I think are some of the best sources available to connect the gap between the theory and the practice that is using a commercial finite element method software.

3.4.1 Static and Dynamic problems

There are essentially two main types of FEA analysis in Solid Mechanics. Static analysis is used for cases where there is a static equilibrium. The equilibrium state of a structure under load can be given as an example for this type of problem. On the other hand, in both of our works, we were interested in the dynamic behaviour of the system, simulating a fly struggling in the web and compression test of a lattice structure.

Static analysis essentially solves the equilibrium condition of total forces all adding up to zero:

$$\sum \mathbf{F} = 0 \tag{3.1}$$

For dynamic analysis, we are interested in how the solid structure changes dynamically, so finite element method solves equations of motion for a continuum. These equations are at the core, a more detailed version of Newton's second law:

$$\sum \mathbf{F} = m\mathbf{a} \tag{3.2}$$

which is used to describe the motion of solid as a function of time.

3.4.2 Implicit and Explicit methods

There are two different approaches to solving dynamic problems: implicit and explicit methods. For the dynamic problems, displacement $u(x, t)$ should be calculated as a function of time, and the equations of motion take the general

form:

$$\mathbf{M}\frac{\partial^2 \mathbf{u}}{\partial t^2} + \mathbf{K}\mathbf{u} = \mathbf{F}(t) \tag{3.3}$$

where M and K are mass and stiffness matrices, respectively. For dynamic calculations such as compression test, the values of $\mathbf{u}$ and $\mathbf{v} = \frac{\partial \mathbf{u}}{\partial t}$ are known from the start, i.e. $t = 0$. If we want to solve this problem using explicit method, we can calculate $\mathbf{M}$ and $\mathbf{K}$ for $t = 0$ and find:

$$a = \frac{\partial^2 \mathbf{u}}{\partial t^2} = \mathbf{M}^{-1}(\mathbf{F}(t) - \mathbf{K}\mathbf{u}) \tag{3.4}$$

which gives the nodal acceleration at every node. From this we can find the velocity $\mathbf{v}(\Delta t)$ and the displacement $\mathbf{u}(\Delta t)$ at time Δt by using

$$\mathbf{v}(\Delta t) = \mathbf{v}(0) + \mathbf{a}\Delta t \tag{3.5}$$

$$\mathbf{u}(\Delta t) = \mathbf{u}(0) + \mathbf{v}\Delta t + \frac{1}{2}\mathbf{a}\Delta t^2 \tag{3.6}$$

Using the same procedure for the next steps, we can deduct the motion of the elements of the structure through time.

The other method is called implicit method, which instead of calculating the mass $\mathbf{M}$ and stiffness $\mathbf{K}$ matrices at $t = 0$, they are calculated at time $t = \Delta t$. This is generally done by matrix inversion or a similar method, which can get pretty complicated for complex problems. In order to show basics of these methods, we can look at a dynamic linear elastic system.

3.4.3 Newmark-Beta Method

Newmark-Beta method is a very popular numerical integration method used for dynamic simulations of solids. Abaqus uses Hilber-Hughes-Taylor method, which is an extension of Newmark-Beta method. Let's consider a forced, undamped spring-mass system with only one degree of freedom, which would be the simplest case. The equation of motion would be:

$$\ddot{u} + ku - f = 0 \tag{3.7}$$

and suppose $f(t)$, $u(0)$ and $\dot{u}(0)$ are known and we can estimate the acceleration $\ddot{u}(t)$ and $\ddot{u}(\Delta t)$ at the start and at the end of the time step Δt. Using Taylor series expansion, we can get:

$$u(t+\Delta t) \approx u(t) + \Delta t\dot{u}(t) + \frac{\Delta t^2}{2}[(1-\beta_2)\ddot{u}(t) + \beta_2\ddot{u}(t+\Delta t)] \tag{3.8}$$

$$\dot{u}(t+\Delta t) \approx \dot{u}(t) + \Delta t[(1-\beta_1)\ddot{u}(t) + \beta_1\ddot{u}(t+\Delta t)] \tag{3.9}$$

Here, by changing the parameters β_1 and β_2 we can change the nature of the calculation. When $\beta_1 = \beta_2 = 0$, the terms with $t + \Delta t$ disappear and the next step is calculated directly from acceleration at time t, thus an explicit scheme. If we choose $\beta_1 = \beta_2 = 1$ then we would be only using the acceleration term at time $t + \Delta t$ which makes this an implicit scheme.

We need to calculate the acceleration at the start and at the end of the time step, since the equations above use both. For that we can use the equation of motion:

$$\ddot{u}(t) = \frac{1}{m}[-ku(t) + f(t)] \tag{3.10}$$

At time $t + \Delta t$, the equation becomes:

$$m\ddot{u}(t+\Delta t) + \frac{1}{m}[-ku(t) + f(t)] \tag{3.11}$$

Using equations 3.8 and 3.9:

$$m\ddot{u}(t+\Delta t)+k\{u(t)+\Delta t\dot{u}(t)+\frac{\Delta t^2}{2}[(1-\beta_2)\ddot{u}(t)+\beta_2\ddot{u}(t+\Delta t)]-f(t+\Delta t) = 0 \tag{3.12}$$

Isolating the acceleration term:

$$\ddot{u}(t+\Delta t) = \frac{1}{m + k\beta_2\Delta t^2}\{-k[u(t)+\Delta t\dot{u}(t)+\frac{\Delta t^2}{2}[(1-\beta_2)\ddot{u}(t)]+f(t+\Delta t)\} \tag{3.13}$$

We can apply this method easily to n-degrees of freedom. Assuming we know K_{aibk}, M_{ab}, $F_i^a(t)$, $u_i^a(0)$, $\dot{u}_i^a(0)$ we can write:

$$\ddot{u}(0) = M_{ab}^{-1}[-K_{bick}u_k^c(0) + F_i^b(0)] \tag{3.14}$$

for t=0. Then for the next steps:

$$M_{ab}\ddot{u}_i^b(t+\Delta t)+\beta_2\Delta t^2 K_{aibk}\ddot{u}_k^b = -K_{aibk}[u_k^b(t)+\Delta t\dot{u}_k^b(t)+\frac{\Delta t^2}{2}(1-\beta_2)\ddot{u}_k^b(t)]+F_i^a(t+\Delta t) \tag{3.15}$$

should be solved for $\ddot{u}_i^a$. Then the displacement and velocity can be calculated as:

$$u_i^a(t+\Delta t) \approx u_i^a(t) + \Delta t\dot{u}_i^a(t) + \frac{\Delta t^2}{2}[(1-\beta_2)\ddot{u}_i^a(t) + \beta_2\ddot{u}_i^a(t+\Delta t)] \tag{3.16}$$

$$\dot{u}_i^a(t+\Delta t) \approx \dot{u}_i^a(t) + \Delta t[(1-\beta_1)\ddot{u}_i^a(t) + \beta_1\ddot{u}_i^a(t+\Delta t)] \tag{3.17}$$

For dynamic calculations, Abaqus uses Hilber-Hughes-Taylor method which is an extension of Newmark-β method, which introduces another parameter that works as controllable numerical damping. As mentioned before, by changing the β values the nature of the method can be changed, and if $\beta_1 = \beta_2 = 0$ then the integration scheme is fully explicit. The explicit method in Abaqus uses central difference operator for calculations, and as the explicit methods go, it is only conditionally stable. The stability limit on step time is roughly equal to the time it takes for an elastic wave to cross the smallest element in the structure. However the implicit method is unconditionally stable, and the step time can be much larger than the explicit methods. However there can be a different problem with the kind of implicit method used in Newark-β where β values are large. While the solution is stable, it may not be accurate, due to energy showing dissipation due to the integration scheme. In order to make it accurate, Abaqus uses a controllable numerical damping parameter α, which was first introduced by Hughes et al. [47].

3.4.4 Choosing a Solver

Our work involves non-linear material models such as spider silk and very high deformations involving damage models. Implicit method, while is very stable, involves matrix inversions, which is harder to implement and more complicated than the basic stepping algorithms of the explicit method. The computational power needed for complex structures with lots of contact points and high deformations becomes very large. Thus, for our projects, explicit method gives the best results in terms of time and manageability.

3.5 Material Models for FEA

For static FEA simulations, a simple linear stress-strain relation might suffice, as the maximum strain achieved in the system is generally still in the elastic range. However, Lattice compression tests involve the plastic region; later, they can break, so a more comprehensive approach should be taken. This involves the plastic behaviour and damage behaviour of the material to be implemented into the material model. For this thesis, three different materials are used for dynamic simulations: Polylactic acid (PLA) used in 3D printers, an alloy of titanium Ti-6Al-V4 that is used in electron beam melting (EBM) additive manufacturing and finally, spider silk. First two materials can be described by using the tools available in Abaqus software however spider silk calls for implementation using a custom made FORTRAN subroutine.

3.5.1 Differing Measures for Stress and Strain

The terms nominal, true and plastic stress-strain are used regularly, and describe different ways of calculating the stress and strain values. When a material is under tension or compression, its cross sectional area changes according to its Poisson's ratio. If the stress and strain is calculated using the original cross sectional area

of the material, then it is called the nominal or engineering stress (σ_{nom}).

$$\sigma_{nom} = \frac{F}{A_0} \tag{3.18}$$

$$\varepsilon_{nom} = \frac{\Delta l}{l_0} \tag{3.19}$$

However a material under tension generally has less cross sectional area as it elongates or more if it's under compression so true stress (σ) and true strain (ε) takes this under consideration. So the strains under compression or tension is equal to true strain only when $\Delta l \ll 0$. When deformation is not negligible, the true strain can be calculated by integrating the strain path. Considering a very small strain:

$$\delta\varepsilon = \frac{\delta l}{l_0} \tag{3.20}$$

$$\int \delta\varepsilon = \int_{l_0}^{l} \frac{\delta l}{l_0} \tag{3.21}$$

$$\varepsilon = ln\left(\frac{l}{l_0}\right) \tag{3.22}$$

The relationship between true and nominal strain can be calculated as:

$$\varepsilon_{nom} = \frac{l - l_0}{l_0} \tag{3.23}$$

$$\varepsilon_{nom} = \frac{l}{l_0} - 1 \tag{3.24}$$

$$\varepsilon_{nom} + 1 = \frac{l}{l_0} \tag{3.25}$$

and by substituting this to equation 3.22 we get:

$$\varepsilon = ln\left(\frac{l}{l_0} + 1\right) \tag{3.26}$$

Considering the volume stays the same during the plastic region, we can also write:

$$A_0 l_0 = Al \tag{3.27}$$

Where A and l are the cross sectional area and length of the material respectively, with 0 subscript is pointing to the original form of the same parameters. Then the area becomes:

$$A = \frac{A_0 l_0}{l} \tag{3.28}$$

So substituting this definition to equation for true stress:

$$\sigma = \frac{F}{A} = \frac{Fl}{A_0 l_0} = \sigma_{nom}\left(\frac{l}{l_0}\right) \tag{3.29}$$

Alternatively we can also write:

$$\sigma = \sigma_{nom}(1 + \varepsilon) \tag{3.30}$$

For defining plasticity in some materials such as PLA, we also need plasticity data which takes the strain as plastic strain (ε^{pl}). Generally the stress-strain data is shown with total strain and should be isolated as:

$$\varepsilon^{pl} = \varepsilon^{t} - \varepsilon^{e} \tag{3.31}$$

Where ε^{e} is elastic strain and ε^{t} is total strain. In Fig.? this terms are shown.

While this section can be seen as very basic by people in engineering field, I feel it is important to show some of the differences in stress and strain definitions. As a physics student in university I wasn't very familiar with these differences as it was not a concern for most of our curriculum, and some of the articles written by

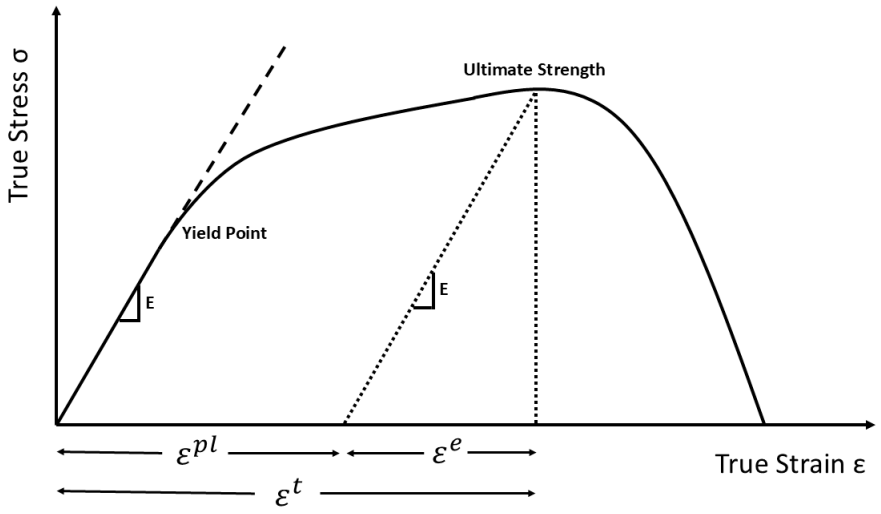


Figure 3.1: Generalized graph for the stress-strain graph of a dog specimen of a material.

biologists can ignore these differences and use them interchangeably. It shouldn't be forgotten when using FEA software such as Abaqus, or writing an algorithm for a custom material, such as in our case for the spider silk, true stress and true strain values should be used.

3.5.2 Material Model for PLA

PLA is a popular material used in 3D printers, and it is one of the popular materials to be utilized in infill lattice design research. In the elastic region the relation between the stress and strain linear and the ratio between them is defined by Young's modulus, $\sigma = E\varepsilon$. For the plastic region, the linear relation changes to a non-linear one, and it can be defined by taking data points from that region, which then would be regularized by Abaqus. This input date would be taken as the true stress value versus true plastic strain.

The damage model is created by the ductile damage criterion in Abaqus. For the damage behaviour, which states that the equivalent plastic strain at the onset of the damage ($\bar{(\varepsilon)}^{pl}$) is a function of the strain rate and stress triaxiality.

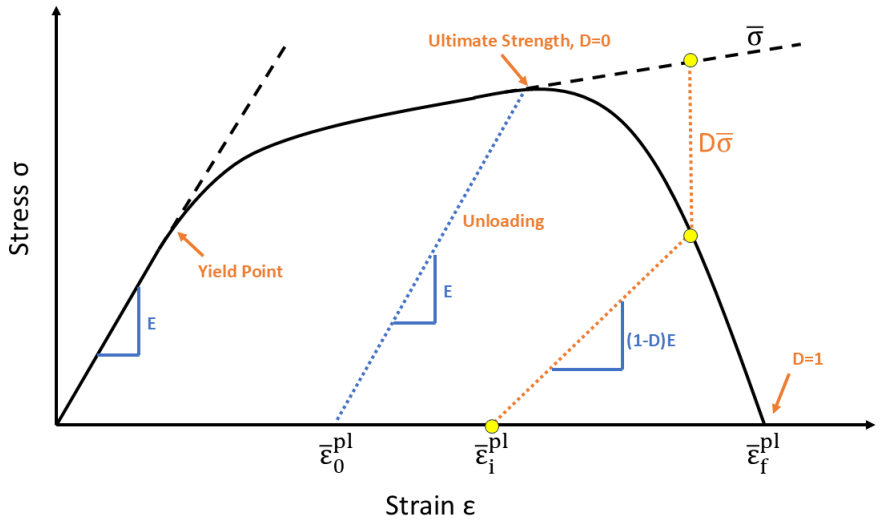


Figure 3.2: Generalized graph for the stress-strain graph of a dog specimen of a material.

Stress triaxiality is a concept that is required to make better predictions for the fracture resistance of a material, which can vary by its geometry, size and the type of loading it endures, such as bending or stretching[48]. A common way of defining this parameter is the ratio of hydrostatic stress to von mises stress. Von mises stress takes into the consideration that in metals plastic flow is induced by shear stresses, which ends up creating dislocation movement in the material[49]. It is evaluated as:

$$\sigma_{eq} = \sqrt{\frac{(\sigma_1 - \sigma_2)^2 + (\sigma_2 - \sigma_3)^2 + (\sigma_3 - \sigma_1)^2}{2}} \tag{3.32}$$

The hydrostatic or mean stress defined as

$$\sigma_m = \frac{\sigma_1 + \sigma_2 + \sigma_3}{3} \tag{3.33}$$

Then the stress triaxiality is defined as a unitless ratio:

$$\eta = \frac{\sigma_m}{\sigma_e q} \tag{3.34}$$

The damage initiation starts when the condition below is satisfied:

$$\omega_D = \int \frac{d\bar{(}\varepsilon)^{pl}}{\bar{(}\varepsilon)^{pl}_D(\eta, \dot{\bar{\varepsilon}}^{pl})} \tag{3.35}$$

When the element fails, Abaqus has the capability of deleting the element that has failed. To use this feature damage accumulation parameter D should be defined, which would decide the evolution of the damage from the onset to failure. This parameter starts from 0 at the ultimate strength value, then goes up to 1 at the failure of the material, which then the software deletes the element. The change from 0 to 1 can be linear, or exponential or any other form that can describe the experimental data the best. In our case we used a simple linear damage evolution.

3.5.3 Material Model for Ti-6Al-4V alloy

Originally developed for use in aerospace industries, Ti-6Al-4V (Ti64) today compromise nearly 50% of the market share of the titanium products [50]. Ti64 has amazing corrosion resistance, high strength with very low density and very good biocompatibility, thus it has a very wide application area. Some examples can be listed as aircraft parts such as jet engines, gas turbines, airframe components [[51], [52], [53]], high-end automobile parts such as spring suspension, intake and exhaust valves and troll platforms for marine industry [54] or implants in biomedical industry [55]. We did simulations for the optimization of its use in energy absorption applications.

Johnson-Cook plasticity model was established by Gordon R. Johnson and Wiiliam H. Cook in order to describe material behaviour under large strains, high strain rates and high temperatures [56]. Its equation is given as:

$$\sigma = [A + B\epsilon^n][1 + cln(\dot{\epsilon}^*)][1 - T^{*m}] \tag{3.36}$$

Here σ is the Johnson-Cook flow stress, $\dot{\epsilon}^* = \dot{\epsilon}/\dot{\epsilon}_0$ is the dimensionless plastic

strain rate where $\dot{\epsilon}_0$ is a reference strain rate and T^* is homologous temperature. The parameters A, B, n, c, and m are the yield stress, hardening modulus, hardening coefficient, strain rate sensitivity parameter, and thermal softening parameter respectively.

In a similar manner, for materials under high strain rates and high temperature, a complementary damage model exists, that is called Johnson-Cook damage model [57]. Its equation is as follows:

$$\epsilon_{pf} = [D_1 + D_2 e^{D_3 \sigma^*}][1 + D_4 ln(\dot{\epsilon}^*)][1 + D_5 T^*] \tag{3.37}$$

where D_1 is the initial failure strain; D_2 is the exponential factor; D_3 is the triaxiality factor; D_4 is the strain rate factor; and D_5 is the temperature factor, which are determined by experimental data [13].

3.5.4 Material Model for Spider Silk

The material model of the spider silk is a bit more complex than the ones we talked about in the previous part. As it was also mentioned in the second chapter, the stress-strain behaviour of this material is the combination of two different responses from two different 'states' existing inside the silk, one is the amorphous polymer chains and the other is crystalline β-sheets. A model picture can be seen in for visualization.

For our studies we used model developed by Tommasi et al [33]. To explain the constituents of the model, let us first consider a one dimensional system with length L, that has two distinct materials, a soft fraction with its percentage denoted by the variable α. This soft fraction is the amorphous polymer part of the system, and described with the worm-like chain model (WLC). This version of the model was proposed for double-stranded DNA [58] and is written as:

$$\sigma_s = \hat{\sigma}_s(\varepsilon, \varepsilon_c) = E_s \left(\frac{1}{4}(1 - \frac{\varepsilon}{\varepsilon_c}^{-2}) - \frac{1}{4} + \frac{\varepsilon}{\varepsilon_c} \right) \tag{3.38}$$

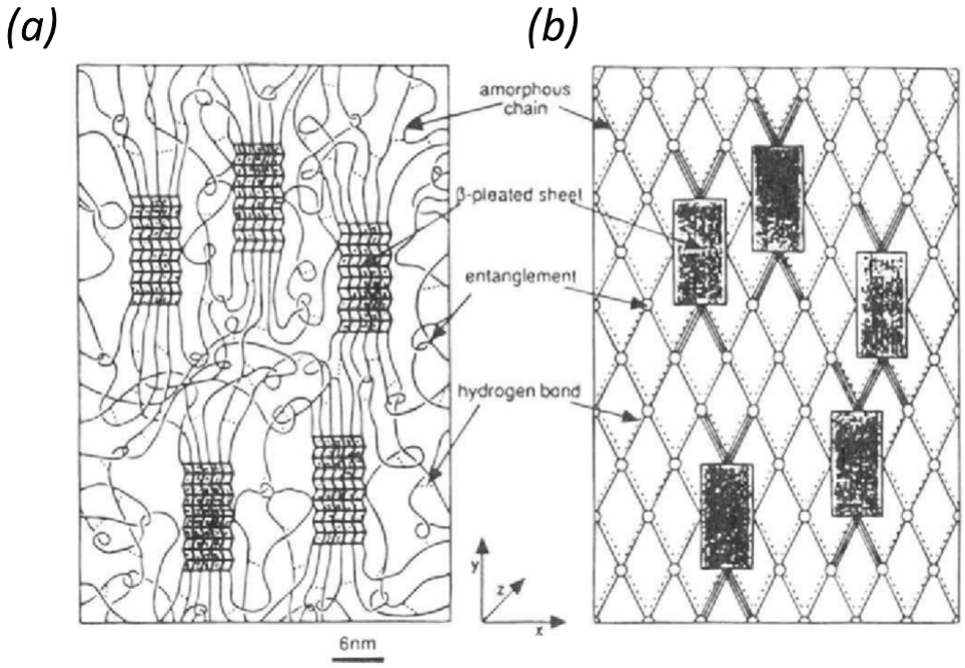


Figure 3.3: A simplified model for the dragline silk of the spider is shown at (a). A more schematic version is shown on the right, with variation among the amorphous chains are not shown. The dotted lines are the hydrogen bonds, and individual bonds have been replaced by "overall" bonds, with a regular bonding between its neighbours. Figure reproduced by permission from ref.: [9]

Here, σ_s gives the stress of the soft fraction and it depends on E_s, ε and ε_c which are the elastic modulus of the soft model, strain and limit strain respectively.

Other part of the structure is the crystalline hard fraction, which has a linear elastic behaviour. Stress relation of the hard fraction is calculated as:

$$\sigma_h(\varepsilon) = \begin{cases} 0, & \text{if } \varepsilon \leq \varepsilon_a \\ E_h(\varepsilon - \varepsilon_a), & \text{if } \varepsilon_a < \varepsilon < \varepsilon_t \\ \sigma_s(\varepsilon, \varepsilon_c), & \text{if } \varepsilon \geq \varepsilon_t \end{cases} \tag{3.39}$$

and σ_h, E_h are the stress and elastic modulus of the hard fraction, respectively. The values ε_a and ε_t represents the activation and transition thresholds, so that the material is 'activated' when $\varepsilon = \varepsilon_a$ and goes through a transition at $\varepsilon = \varepsilon_t$. This transition is in the form of the β-sheets unravelling from their crystalline

form to an amorphous structure, which requires the breakage of the hydrogen bonds. These crystallite can have quite different structures, so they can also have different activation and transition thresholds. Thus we need to consider a distribution of different crystallite structures inside the system. While these threshold values can change for each structure, it is assumed that it takes same amount of strain for each structure to go from activation to transition strain, i.e.:

$$\varepsilon_t - \varepsilon_a = \delta \tag{3.40}$$

This assumption allows us to represent distribution of the hard material to be represented as a single-parameter probability function with Gaussian type distribution as shown below:

$$p(\varepsilon_t) = \xi e^{-\beta(\varepsilon_t - \gamma)^2} \tag{3.41}$$

Here, ξ is needed for the normalization of the probability function as $\int_0^\infty p(\varepsilon_t)\, d\varepsilon_t = 1$.

As these hard fraction unravels, the contour length increases, which means the maximum length of the polymer chain increase. For this reason, as the percentage of the soft fraction in the system increase, so:

$$\varepsilon_c = \hat{\varepsilon}_c(\alpha) \tag{3.42}$$

where $\hat{\varepsilon}_c$ is an increasing function.

Without strain, let the soft fraction in the material be α_0. Then under loading, when strain starts to increase, the fraction becomes:

$$\alpha = \alpha^l(\epsilon) = \alpha_0 + \int_0^\varepsilon p(\varepsilon_t) d\varepsilon_t \tag{3.43}$$

Now remembering the previous statement about the varying structures of the hard material, not all of them are under stress. So, the amount of active hard structures inside the system is $\int_{\varepsilon}^{\varepsilon+\delta} p(\varepsilon_t)\, d\varepsilon_t$ and the amount of inactive is $\int_{\varepsilon+\delta}^{\infty} p(\varepsilon_t)\, d\varepsilon_t$. So the stress-strain relation under loading is given by:

$$\sigma = \alpha^l(\varepsilon)\hat{\sigma}_s(\varepsilon, \hat{\varepsilon}_c(\alpha^l(\varepsilon))) + E_h \left(\int_{\varepsilon}^{\delta} \varepsilon p(\varepsilon_t) d\varepsilon_t + \int_{\max(\varepsilon,\delta)}^{\varepsilon+\delta} (\varepsilon - (\varepsilon_t - \delta)) p(\varepsilon_t) d\varepsilon_t \right) \tag{3.44}$$

Here, the first integral represents a hard material with its $\varepsilon_t < \delta$ and its $\varepsilon_a = 0$. For the second integral, $\varepsilon_t > \delta$ and the activation and $\varepsilon_a = \varepsilon_t - \delta$

As can be seen in Fig.?. the unloading path is different than the loading case for the spider silk. For the case of unloading, let's assume a strain path of $\varepsilon : \varepsilon_M \to 0$. In this process all the hard material with $\varepsilon_t < \varepsilon_M$ turns into soft material. Thus we have:

$$\alpha = \alpha^u(\epsilon_M) = \alpha_0 + \int_0^{\varepsilon_M} p(\varepsilon_t) d\varepsilon_t \tag{3.45}$$

And, the contribution coming from the hard material is the ones that are still not fully stretched out, so $\varepsilon_t < \varepsilon_M$ but also $\varepsilon = \varepsilon_t - \delta < \varepsilon$ so that it is partially unravelled. Thus the equation becomes:

$$\sigma = \alpha^u(\varepsilon_M)\hat{\sigma}_s(\varepsilon, \hat{\varepsilon}_c(\alpha^u(\varepsilon_M))) + E_h(\int_{\varepsilon_M}^{\varepsilon+\delta} (\varepsilon - (\varepsilon_t - \delta)) p(\varepsilon_t) d\varepsilon_t \tag{3.46}$$

Soler et al.[10] implemented this model in their spider web simulations, with an important modification:

$$\begin{aligned} \sigma(\varepsilon, \varepsilon_M) &= \alpha_s \sigma_s + \alpha_h \sigma_h \\ &= \alpha_s(\varepsilon_M)\sigma_s(\varepsilon, \varepsilon_c(\alpha_s)) + E_h \left(\int_{\varepsilon_M}^{\delta} \varepsilon p(\varepsilon_t) d\varepsilon_t + \int_{max(\varepsilon_M,\delta)}^{\varepsilon+\delta} (\varepsilon - (\varepsilon_t - \delta)) p(\varepsilon_t) d\varepsilon_t \right) \end{aligned} \tag{3.47}$$

This modification helps us to use a single single equation to calculate both the loading and unloading stages, where for the Tommasi et al.[33] there were three different equations. This is also the version we used in our research. The stress-strain graph of the resulting curves can be seen in Fig.3.4.

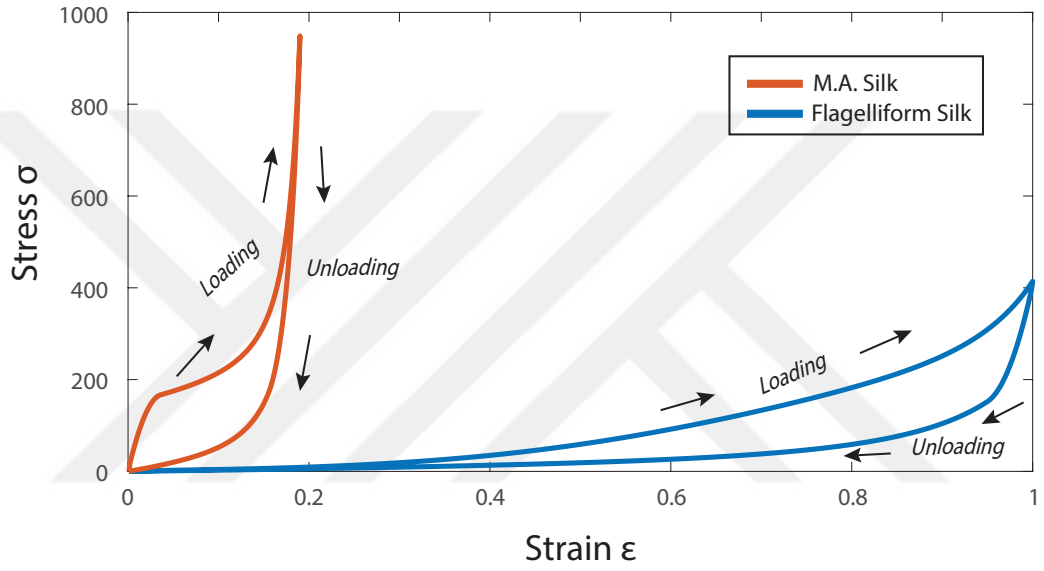


Figure 3.4: Stress strain graph for the Major Ampullate and the Flagelliform silk, showing the loading and unloading behaviour of the material model used in our work, also in [10].

Chapter 4

Spider Web Lattice

4.1 Introduction

Cellular materials such as metallic foams and hexagonal lattice are utilized for their outstanding mechanical properties and weight-saving benefits in industries such as aerospace and automotive. Lattice structures are a subgroup of cellular materials that are characterized by their interconnected network of struts or beams, as well as minimal surface structures which have exceptional strength-to-weight ratios and customizable geometries, making them ideal for engineering applications requiring lightweight yet durable components for applications such as energy absorption[59][60], heat exchange[61][62] or vibration damping[63][64]. Because of their mechanical performance and advantages in saving weight and material, they find use in a wide range of fields involving aerospace[65], biomedical engineering [66] and automotive industry [67].

The mechanical performance of lattice structures depends on many variables such as the material used, porosity of the structure, unit cell size, and topological shape, which is one of the major contributors to its mechanical properties. The topology of the unit cell can be generalized into two categories: bending dominated and stretch dominated, with both having different mechanical behaviour

under deformation [68]. Stretch-dominated lattice structures have a large initial stress peak under compression, which makes them suitable for applications that require high stiffness. Examples of this type can be listed as simple cubic [69] and octet lattices [70]. Conversely, bending-dominated cells do not have large stress fluctuations under compression, which is desirable for energy absorption applications. However, their compression stress is relatively weak compared to stretch-dominated counterparts, such as body-centred cubic [71] and rhombic dodecahedron [69, 70] lattices. So, without any modification, these structures perform worse in each other's domain, limiting their possible multifunctional use.

With the developments in additive manufacturing, it is possible to create complex lattice structures that were not possible with the conventional techniques [19], so designs can be tailored to enhance the mechanical properties of lattices. A great deal of research has been done on altering existing lattice designs to improve their mechanical properties and remove their weaknesses. Some of the examples of these alterations are adding struts [72], using hollow struts [73] or tweaking their geometry, such as changing strut geometry [74, 75]. There is also much work to be done to create new designs that can have superior mechanical properties, and one of the sources researchers take inspiration from is nature.

Natural selection drives biological organisms to develop different solutions to cope with environmental stress, and using biomimicry, scientists try to implement these solutions to solve similar problems in engineering. In recent years, biomimicking new lattice designs have emerged to create more efficient lightweight structures for energy absorption applications, with better compressive strength and total energy absorbed compared to conventional designs. For example, An et al. created luffa sponge-like hierarchical foam cylindrical structures, which have improved specific energy absorption (SEA) compared to the pure aluminium foam cylinder[24]. Yu et al. designed a crush box inspired by the beetle elytra, which shows 5 times better energy absorption and 2.6 better compression force efficiency compared to a conventional crush box[22]. Mao et al. proposed a cuttlefish bone-like cellular lattice that shows better energy-absorption capability than octet-truss lattice and conventional polymer and metal foams[23]. Guo et.

al. created diamond TPMS lattice inspired by the skeleton of the starfish Protoreaster nodosus, which shows good specific energy absorption and remarkable damage tolerance[76].

In this study, we propose a new lattice design(SW) for energy absorption inspired by one of nature's best energy absorbers, spider webs. SW lattice design tries to imitate the hierarchical structure of the spider orb web, which is then optimized to make its energy absorption capability as high as possible while not diverting too much from an ideal energy absorber, which avoids violent stress undulations.

4.2 Materials and Methods

This section presents the design strategy, finite element analysis, and experimental methods. Two different materials are tried with our new design, and while the optimization parameters are the same, the optimized structures and their results will be different. So, the reader must be aware of this fact and expect two different studies based on the same design principles.

4.2.1 Design Strategy

Spiders construct different types of silken structures for different roles, such as shelters for moulting or protective sacs for their eggs, but they are mostly known for creating webs to capture prey[6]. One of the most recognizable forms of spider web is the spider orb web, which is a hierarchical structure made up of mainly four structural elements: anchor, frame, radii and spiral threads[77, 78]. Anchors, frames and radii form the structural framework for spirals and are secreted from major ampullate glands, which produce tougher and stiffer silk compared to sticky spirals. Thus, our inspiration for the lattice design comes from the three structures made from major ampullate silk, anchor, frame and radii[7][79]. While

these structures have similar chemistry, their thicknesses are varied and generally decrease from exterior to interior, i.e., anchor thread is thicker than frame threads, and frame threads are thicker than radials[77][80]. Another feature of this structure is that the spider avoids direct connection between anchors and radials, which makes the web resilient to external stressors such as wind or impact of large insects[37] and compared to systems where radials are connected to anchors, the stress is shared more evenly across the web which allows absorbing more energy before fail[10]. We tried to imitate the spider web's design features by making a strut-based lattice where three separate parts, anchor, frame, and radii, are considered. The "anchor" struts sit at the corners of the cubic design space, and direct connection between them and radii struts are avoided by putting frame struts between them(Fig 4.1(b)).

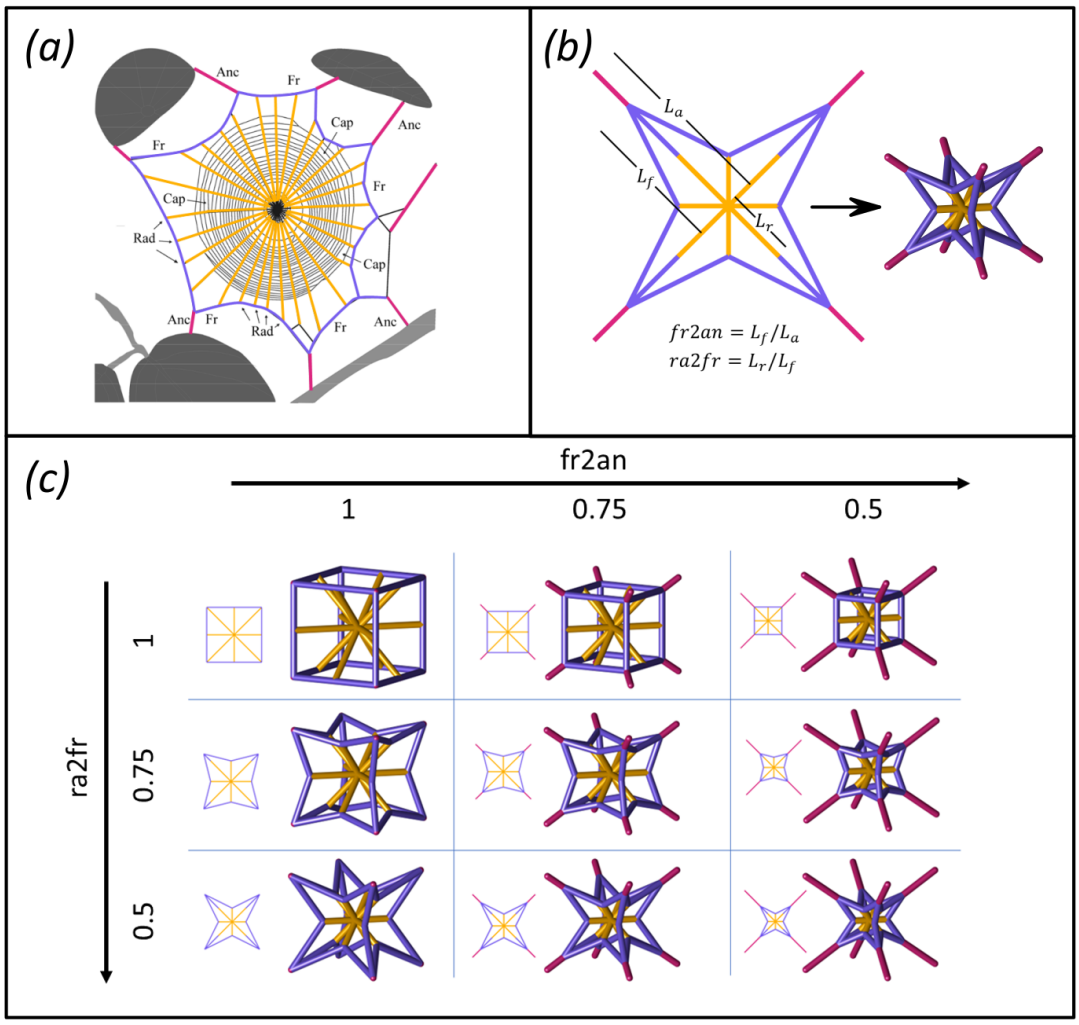


Figure 4.1: (a) Main structural elements of a spider orb web of Cyclosa Caroli is shown. Anchor threads (Anc) attach to the surrounding vegetation and connects to frame threads (Fr). Radii (Rad) radiates from hub to frame threads thus there is no direct link to anchor threads. Capture spirals (Cap) are connected to radii. Redrawn with permission, after Hesselberg (2015). (b) 2D design scheme of SW-p lattice is shown which is the view from the top of the 3D lattice. Anchor struts are connected to frame struts which connect to radii with no direct link between radii and anchors. L_a, L_f and L_r are defined as the length from the hub to corner of the unit cell, corner of the frame struts and corner of the radii struts respectively. Then two geometric parameters are defined as their ratios, $fr2an = L_f/L_a$ and $ra2fr = L_r/L_f$ which adjusts the anchor strut length and convexity of the frame struts respectively. (c) The resulting shapes with changing fr2an and ra2fr values are shown.

As observed in the spider web, we also included a thickness hierarchy in our design that is similar to the natural spider orb web structure. Our observation during the optimization trials was that when the thickness of the struts decreased from exterior to interior, energy absorption metrics such as total energy absorption and energy absorption efficiency were affected positively. We also defined two different parameters that change the form of the design, making the size of each of the three structural elements, anchor, frame and radii, variable. These parameters are chosen to make a more efficient design and will be discussed in more detail under the optimization formulation part.

4.2.2 Energy Absorption Metrics

Compressive stress-strain plot is widely used to show the compressive behaviour of a cellular structure. A generalized example of such plot is shown in Fig 4.2. Compressive stress(σ) is calculated by dividing the compressive load carried by the cellular structure to its cross sectional area that is perpendicular to load direction at any point in time during the compression. Compressive strain(ε) is defined as the displacement caused by compression divided by the total length of the cellular structure parallel to the load direction.

There are three regimes described during the deformation of a structure, first one being the elastic regime which lasts until the strain reaches to yield strain (ε_y) where plastic deformation starts. The second regime is called the plateau regime and it describes the region between the yield strain and densification strain (ε_d) where stress value generally fluctuates. The average stress value at the plateau regime is called plateau stress(σ_{pl}) calculated by Eq.(4.1):

$$\sigma_{pl} = \frac{\int_0^{\varepsilon} \sigma(\varepsilon) d\varepsilon}{\varepsilon_d - \varepsilon_y} \tag{4.1}$$

The last part of the compression is called the densification regime. After a certain strain value is reached ($\varepsilon = \varepsilon_d$) the stress stops to fluctuate and starts to increase rapidly, caused by the collapse of all the lattice structures.

Several metrics are used for the evaluation of the energy absorption performance. One of these metrics is energy absorption (EA) that is calculated by the area under the stress-strain curve up to a specific strain value shown in Eq.(4.2):

$$EA = \int_0^{\varepsilon} \sigma(\varepsilon) d\varepsilon \tag{4.2}$$

Another important metric is called energy absorption efficiency (EAE), which is related with the concept of ideality for an energy absorber. Ideality is defined as the ability of an energy absorber to keep constant force while being compressed[81]. Thus an Ideal energy absorber has constant stress σ throughout its compression which is equal to the peak stress (σ_p). Thus EAE is represented as the ratio between the energy absorbed and σ_p given by Eq.(3):

$$EAE = \frac{\int_0^{\varepsilon} \sigma(\epsilon) d\varepsilon}{\sigma_p} \tag{4.3}$$

Fig 4.2 shows an exemplary stress-strain curve with efficiency-strain curve drawn together. From experimental data, maximum value of the efficiency strain curve is equal to the EAE value, and the strain value it reaches to maximum will be at the densification strain. For an ideal energy absorber, EAE would be equal to 100%. This would mean there are no stress fluctuations at the plateau regime. Then, crushing force efficiency, calculated by the formula:

$$CSE = \frac{\sigma_{pl}}{\sigma_p} \tag{4.4}$$

would be equal to one.

EA is generally given in the units of energy over volume. However different types of lattices can have different materials used or can have different relative densities. In this case, specific energy absorption value should be used for comparison, which has units of energy over mass and calculated as:

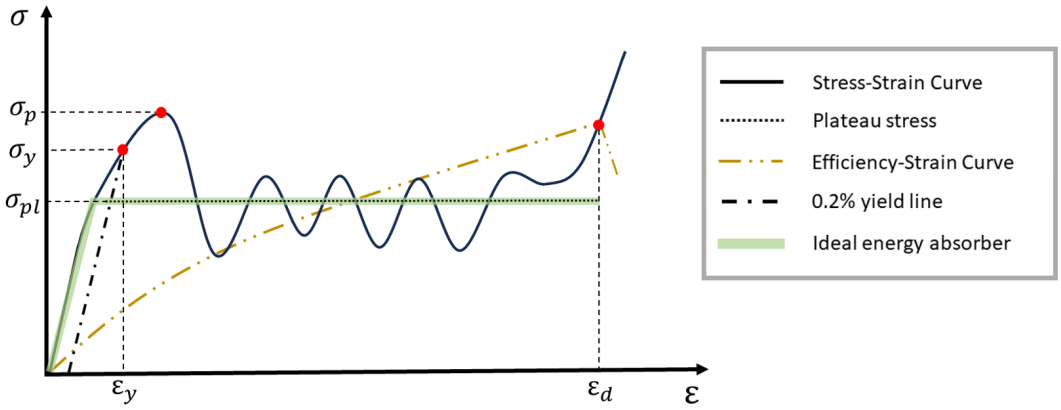


Figure 4.2: An exemplary stress-strain curve for compression test.

$$SEA = \frac{\int_0^{\varepsilon} \sigma(\varepsilon) d\varepsilon}{\bar{\rho}\rho_m} \tag{4.5}$$

where $\bar{\rho}$ is the relative density and ρ_m i the density of the material used.

4.2.3 Finite Element Analysis

Lattice compression simulations were done using the commercial software ABAQUS. Two rigid plates were modelled; one is placed under the lattice model and constrained on all degrees of freedom to act as a stable platform. The other plate is used as a loading plate that moves with predefined velocities. The lattice models were first created using two-node linear Timoshenko beam elements (element type B31), which enables a much lower computational burden compared to 3D solid elements, thus decreasing the time spent on the optimization process. However, beam element models show delayed onset for densification due to how the beam elements are connected at a single node in ABAQUS, disregarding any complex interactions at the joints. So after the optimization, a 3D lattice model is created via Cadquery[82] and meshed using second-order tetrahedral solid elements (C3D10M), resulting in better alignment with the experimental values.

For the energy absorption experiments, the deformation rate is generally chosen to be low enough that the compression will be quasi-static. However, quasi-static deformation rates in finite element simulations would have considerably high computation times. To lower the computational costs of the simulations, methods such as mass scaling or increasing the deformation rate can be utilized as long as the inertial effects are low enough that they will not affect the result. If the kinetic energy in the lattice is small in relation to the total internal energy, the simulation is considered to be quasi-static and produces similar results [83]; for this reason, the ratio of kinetic energy to internal energy should not exceed 5% [84]. In order to achieve both the inertial effects remaining negligible while having acceptable computational expense, the velocity of the top plate is chosen accordingly. For the simulations with beam elements, the velocity of the top plate is chosen to be a value corresponding to a strain rate of $100s^{-1}$ and for tetragonal elements, a strain rate of $10s^{-1}$. At the initial phases, the internal energy is generally low, so the prescribed velocity is increased gradually at the very start. Hence, the kinetic energy to internal energy ratio stays below 5%.

The interaction between the rigid shell and the lattice model, as well as between the struts themselves, is defined with a general explicit contact algorithm.

4.2.3.1 Beam elements vs. 3D solid elements

While beam elements are used extensively in the literature for infill lattice design research, it is important not to look past what kind of designs they should be used with and in which conditions they would give correct results. A general rule of thumb is that the strut length to diameter ratio should be around 10; however, in the literature, this ratio can be even lower than 3 [85]. With low aspect ratio struts, the result might not be accurate, and in general, some researchers show that the results acquired using beam elements generally have less ultimate strength, plateau stress, and later densification onset than experimental tests.

These inaccuracies are reported in the literature [86, 87, 88, 89, 11, 90], and there are different methods for getting better results using beam elements. Smith

et al. considered that the thickness at the connection nodes of the struts should be higher than the cross-section of the struts, so that increasing the thickness of the nodal regions [89], similar to Labeas et al. [88]. Luxner et al. instead increase the elastic modulus 1000 fold at the nodal regions to account for the larger thickness at these regions[90]. These methods did not produce satisfactory results for our models. Sun et al., in their work, show that this issue comes from the lowering of the contact thickness as the finite element length is shortened [11], which is a response by Abaqus for avoiding overlap of the beam elements' circumference at the connection points (Fig 4.3). This makes mesh convergence analysis unobtainable when using beam elements with a damage model since as the mesh gets smaller, so do the yield stress and plateau stress.

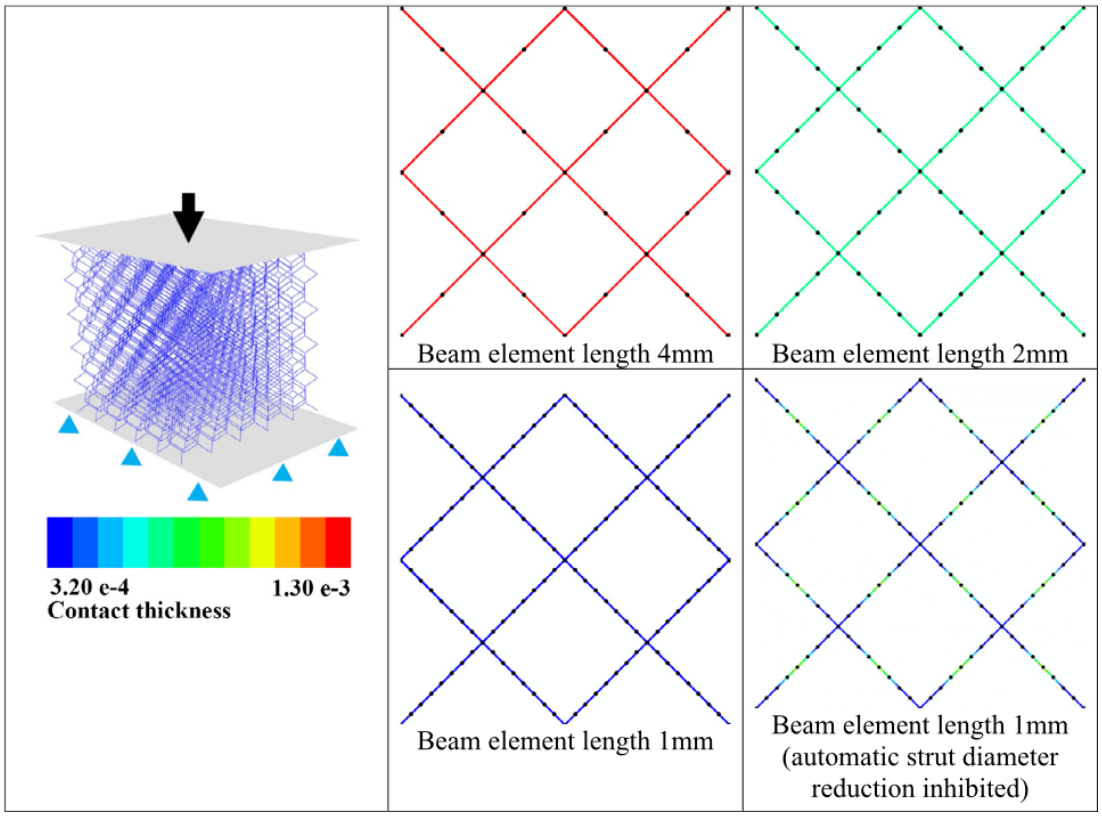


Figure 4.3: Lattice meshed by beam elements of different lengths in Abaqus; colours on the beam show the effective thickness taken by the Abaqus in order to calculate the thickness at contact points. Image used by permission from ref.:[11]

With no satisfactory solution to beam contact thickness problem, we used regular beam model for the optimization process, as it is much faster than 3D

models, however we then confirm our structure's behaviour by 3D model. While the beam models are not accurate, it is no big stretch to consider them suitable for comparing different structures inside the optimization scheme since a comparison between similar (but not identical) structures would not need real values of the parameters such as ultimate strength but the general behaviour of the stress-strain during compression. We then can choose the best solution coming from the optimization process and verify it by simulations using 3D C3D10M element mesh, and also experiments for the manufactured model. This procedure is fully utilized for the PLA lattices.

4.2.3.2 Material model

For the PLA material model, the parameters from the ref:[91] is used. For EBM manufactured Ti-6Al-4V alloy, material parameters are taken from [13] which were Johnson-Cook plasticity and damage models. Parameters used can be seen below.

Table 4.1: Material properties of PLA.

Post-yield true stress vs. true plastic strain						
Stress (MPa)	34.2	37.3	39	41.7	42.9	45.2
Plastic strain	0	0.001	0.002	0.003	0.0037	0.005

Table 4.2: Johnson–Cook plasticity and damage model parameters from [13].

Model Name	$A(MPa)$	$B(MPa)$	n	D_1	D_2
Y-direction	980	919	0.33	0.119	0.109
Z-direction	945	919	0.32	0.07	0.176

The implementation of these material models are explained in detail at chapter 3.5.

4.2.4 Experimental Tests

PLA structures were manufactured and used in compression tests. Because of the high cost Ti-6Al-4V specimens have not been manufactured. The experimental tests of PLA lattice specimens were conducted in a universal testing machine (Instron 600 LX, USA) with a speed of 1mm/min. Image of the set up can be seen in Fig **??**.

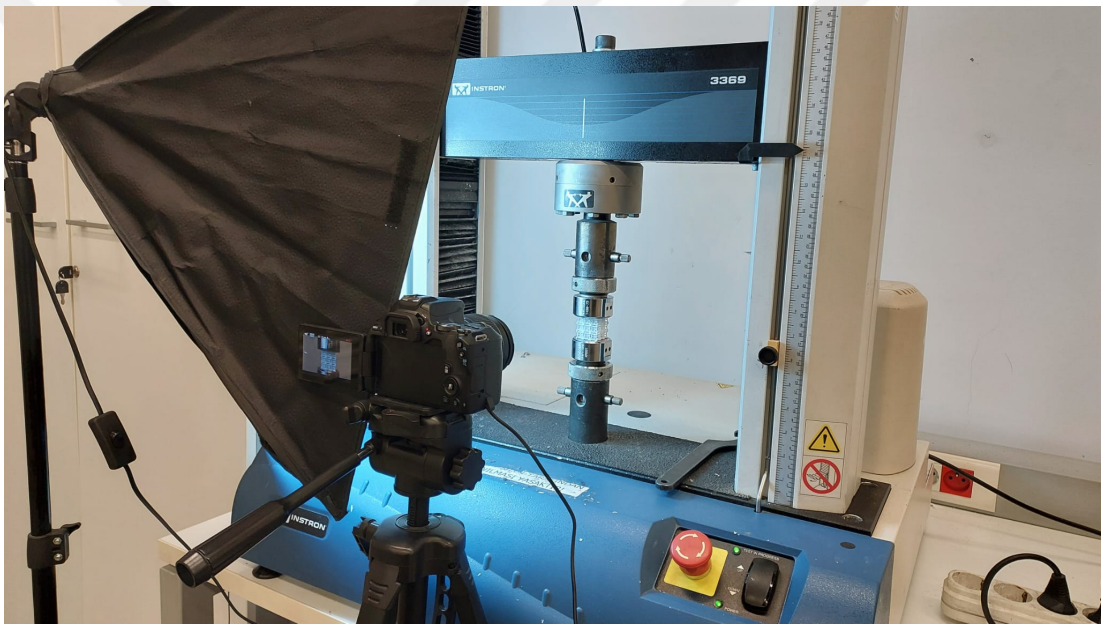


Figure 4.4: Compression test set up.

The compression tests are recorded with a digital camera, which also provide the strain data.

4.2.5 Optimization Formulation

Ideally a good energy absorber possesses both high EAE, where the stress value during compression has low fluctuation and high EA value so that the maximum energy is absorbed before failure. So a multi-objective optimization should be formulated where EAE and EA both can be maximized.

In order to incorporate structural variation to our spider web design we created 2 parameters that can control the length of the anchor struts and convexity of frame struts, as can be seen in fig 4.1(b). From the top view of the design, we define three lengths, that measures from the center to corner of the each structural element, L_a for anchors, L_f for frames and L_r for radial struts. Structural variation parameters then defined as:

$$fr2an = L_f/L_a \tag{4.6}$$

$$ra2fr = L_r/L_f \tag{4.7}$$

By changing these parameters, different variations to the existing design can be created. Visual representation of some of the variations are shown in Fig 4.1(c).

There is also a thickness hierarchy found in spider webs, where anchor threads are thicker than frame threads and frame threads thicker than radii threads. In our own optimization trials, we have observed this hierarchy do help with the EAE of our design. Thus in order to control the hierarchy between the struts, two additional parameters are defined which controls the ratio between the diameters of anchor, frame and radial struts, d_a, d_f and d_r respectively:

$$r_{af} = d_f/d_a \tag{4.8}$$

$$r_{fr} = d_r/d_f \tag{4.9}$$

With four parameters and two objectives in total, the multi objective optimization formulation can be summarized as:

$$\begin{aligned} \text{Find:} \quad & fr2an,\ ra2fr,\ r_{af},\ r_{fr} \\ \text{Maximize:} \quad & EAE,\ EA \\ \text{Subject to:} \quad & 0.5 \leq fr2an,\ ra2fr \leq 1 \\ & 0.05 \leq r_{af},\ r_{fr} \leq 1 \end{aligned} \tag{4.10}$$

Non-linear lattice compression simulations have very high computational costs; thus, common multiobjective optimization algorithms, such as genetic algorithms, are unsuitable because of the large number of inputs they require. For this reason,

we used the Thompson sampling efficient multiobjective optimization (TS-EMO) algorithm created by Bradford et al., which was developed to solve optimization problems with expensive, black-box objective functions [12].

The steps of the TS-EMO algorithm can be summarized as follows: After evaluating a certain number of samples chosen by Latin hypercube sampling, Gaussian process models(GP) are created for each objective. Using spectral sampling, sample functions are created. Then, the Pareto front of these sample functions is calculated, which forms the possible candidates for the next sampling point to evaluate. TS-EMO uses Thompson sampling to have a balanced approach to choosing possible evaluation points, to either explore the high uncertainty regions of the mean functions of the GPs or exploit the low uncertainty regions for finding non-dominated points to improve the dataset. The next evaluation point from the resulting candidate sample set is chosen using the hypervolume criterion.

For the optimization of lattices, we still needed around 140 simulations, so in order to lower the computational cost, 2x2x2 lattice structures were utilized (Fig 4.5). Normally, a larger number of cells should be used for the results to converge. However, the only task here is to compare different structures in an optimization. Then, to better showcase the lattice's capabilities, the remaining simulations and the experiments of the optimized structure utilize a size 3x3x3 lattice. The reason for not going above this number is the computational cost of the simulations comprising three-dimensional elements. As the element number increases exponentially with increasing lattice size, the extra cost can quickly become a problem.

4.2.6 Results for the PLA based SW Lattice

The main work of the SW lattice is made by using PLA, for which we have done simulations using both beam and 3D elements, along with manufacturing of the lattices with 3D printer and compression experiments of the manufactured samples. Here, the mesh analysis, comparisons of various simulations and experiment results of the SW lattice made from PLA are presented.

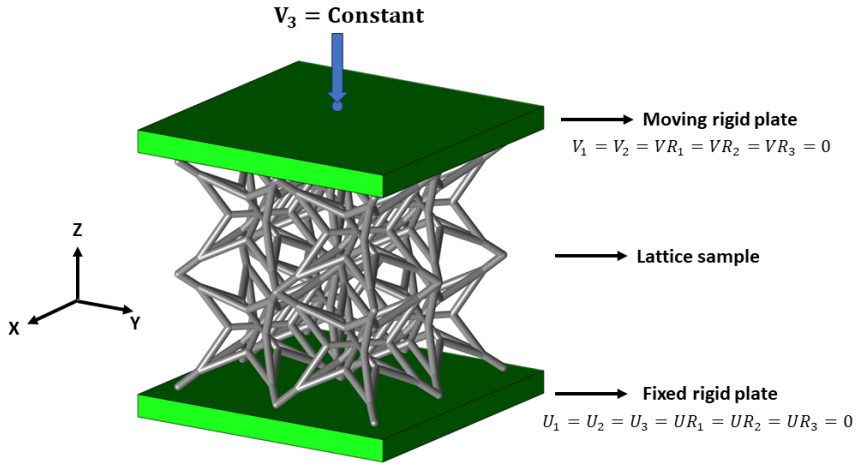


Figure 4.5: Representation of FE model with boundary conditions used in optimization scheme.

4.2.6.1 Mesh Analysis

We have run mesh analysis for both the beam element and the 3D solid mesh elements. For beam elements we used what we call a "generic SW lattice" with all the struts having the same $1mm$ thickness and geometric parameters being the mean value of the possible variations: $fr2an, ra2fr = 0.75$. For the beam elements, as the mesh length becomes shorter, the changes in plateau stress differs less and less and becomes only %3.3 between $0.5mm$ and $0.25mm$(Fig 4.6). In order to have accurate results while keeping computational burden low, $0.5mm$ is chosen for mesh length of the beam elements.

After the optimization step, the optimized model is chosen from the Pareto structures, and convergence analysis for the 3D elements is done on the optimized model. During the analysis, a wide range of element sizes showed very similar results, so we chose our mesh size to be $0.7mm$, which gives the best coverage with good quality mesh while keeping the computational cost low. The reason we did not consider a larger number of different mesh sizes is that our lattice model was structurally complex with many strut connections. This feature makes using

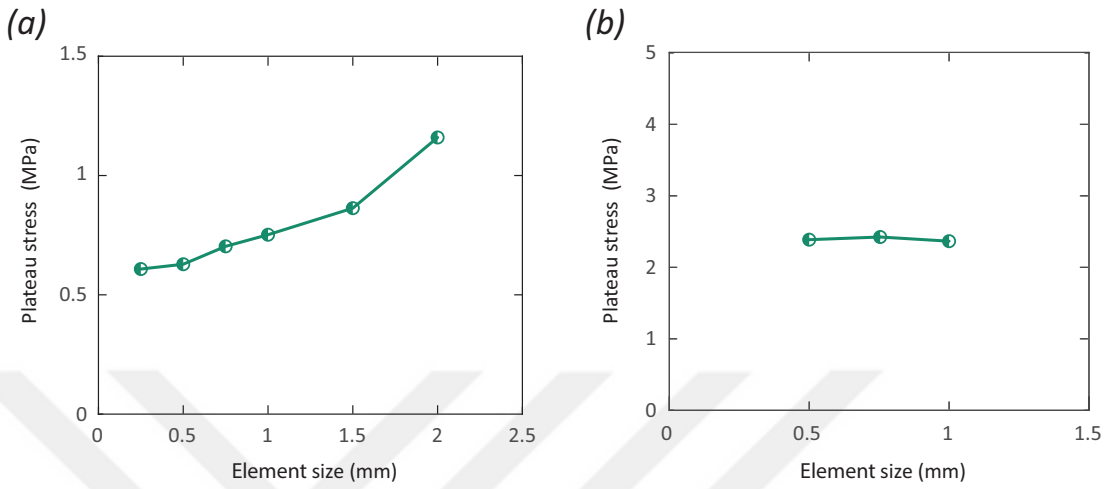


Figure 4.6: Mesh convergence analysis for (a) beam elements and (b) 3D tetrahedral elements.

higher element size impossible to use without a percentage of them being bad quality elements, which cannot cover the model without altering the physical structure of the lattice.

4.2.6.2 Optimization results

The Pareto front of the optimization is shown in Fig 4.7. Among these results, the candidates 3^{rd}, 4^{th}, 5^{th}, and 6^{th} look topologically similar, and 6^{th} candidate looks like the optimal option, as for the later options energy absorption capability falls steeply.

However, the compressive strength of the 3^{rd} option seems higher and its densification point is reached at a higher strain value (Fig. 4.8(a)). Considering the inaccuracy of beam elements as mentioned before, we have compared the 3^{rd} and the 6^{th} options using FEA with 3D tetrahedral elements (Fig. 4.8(b)). For each of the optimization objectives, EA and EAE, 3^{rd} option performs better with better compressive strength. The exact numbers are $EA = 1.19$ and $EAE = 48.28\%$ for 3^{rd} option and $EA = 0.99$ and $EAE = 45.42\%$ for 6^{th} option. Considering these results, 3^{rd} option was picked.

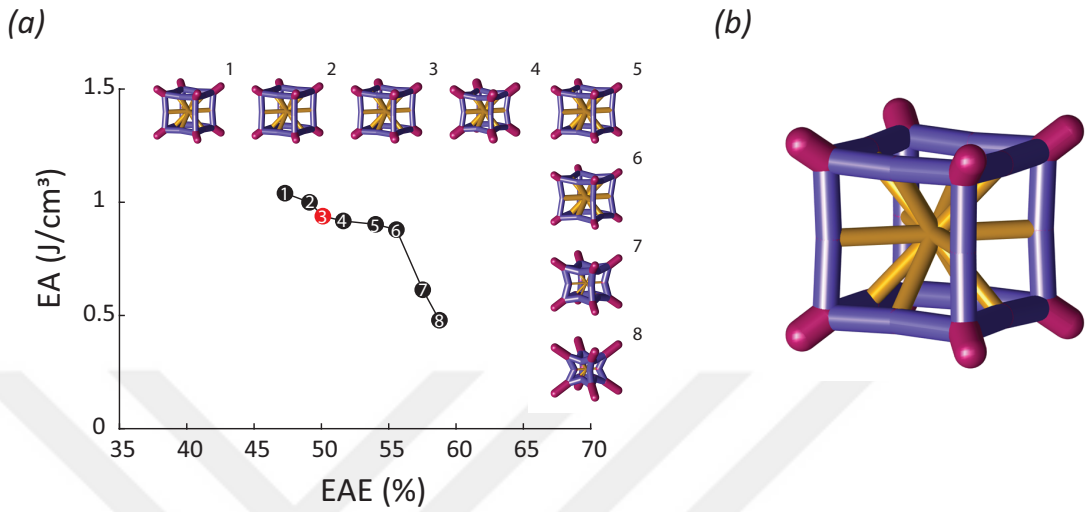


Figure 4.7: (a) Pareto front generated by the optimization [12], the chosen structure is shown with red dot. (b) Unit cell of the chosen structure, with parameters $rad2fr$: 0.95, $fr2an$: 0.85, $r_{af} = 0.65$, $r_{fr} = 0.80$. The results are for SW lattice made from PLA material.

Using cadquery, a three dimensional model of this structure is created. The volume fraction of this lattice was %18, which is obtained through the volume measurements on the digital three dimensional model.

For the optimized model, four different simulations were run in total: dynamic explicit analysis using beam elements, 3D tetrahedron elements with and without damage model included, and static linear perturbation analysis. Linear perturbation analysis shows agreement only with the elastic region, however this agreement shows if our simulations were indeed quasi-static. If our dynamic simulations were to have a higher elastic modulus than what we have picked up by linear perturbation analysis, this would show that either by increasing the compression rate or mass scaling too much, our model has unrealistic stiffness, so our results were inaccurate.

When comparing to the 3D element models, beam element model shows lesser yield strength and plateau stress while having much higher densification strain, as expected. The comparison between them can be seen in Fig 4.9.

We have compared linear perturbation analysis to the 3D simulations with and

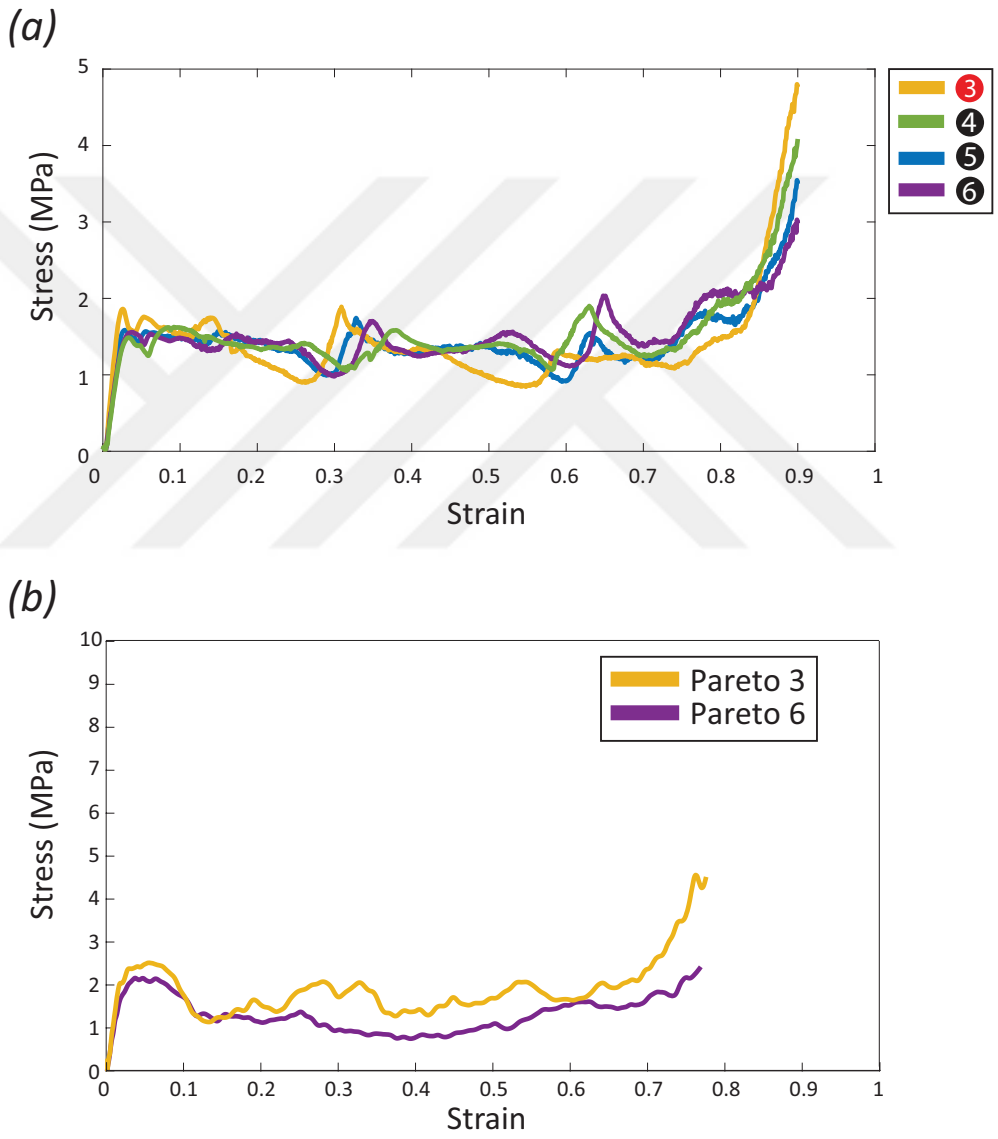


Figure 4.8: (a) FEA result utilizing beam elements, showing 3^{rd}, 4^{th}, 5^{th}, and 6^{th} options from the Pareto front (Fig 4.7), (b) FEA result utilizing 3D tetrahedral elements with damage model, for the 3^{rd} and 6^{th} options.

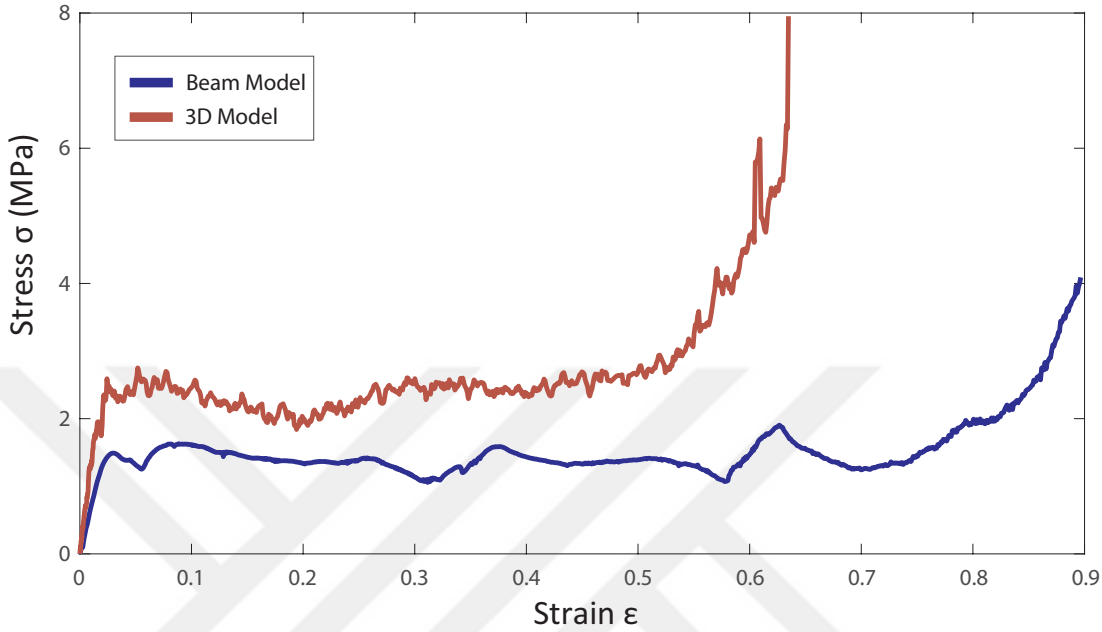


Figure 4.9: Difference in stress-strain behaviour of simulations done with beam and 3D tetrahedral elements.

without the damage model. Our results show that mass scaling and strain rate we used in our simulations didn't affect the quasi-static nature of the compression, and kinetic energy is negligible compared to the internal energy. This is important to make sure that no inertial effects are present in the simulations. When the damage model is not included, the resulting stress-strain behaviour is much more smoother than expected, since without the damage model the breaking of the struts are omitted from the results. The results are shown in Fig 4.10.

Comparing our 3D simulation with damage model result with the experiments, yield stress are largely in agreement, 2.34 and 2.32 MPa respectively. The general behaviour of the stress-strain curve is similar however densification onset is delayed by 0.09 strain. Interestingly, simulation without the damage model shows its densification strain being the same with experiments. One reason might be the implementation of the damage model into the software. Abaqus uses element deletion after complete failure is achieved, and since the material is artificially removed from the system, the densification strain might be delayed.

The comparison between experiments and the 3D simulation with damage

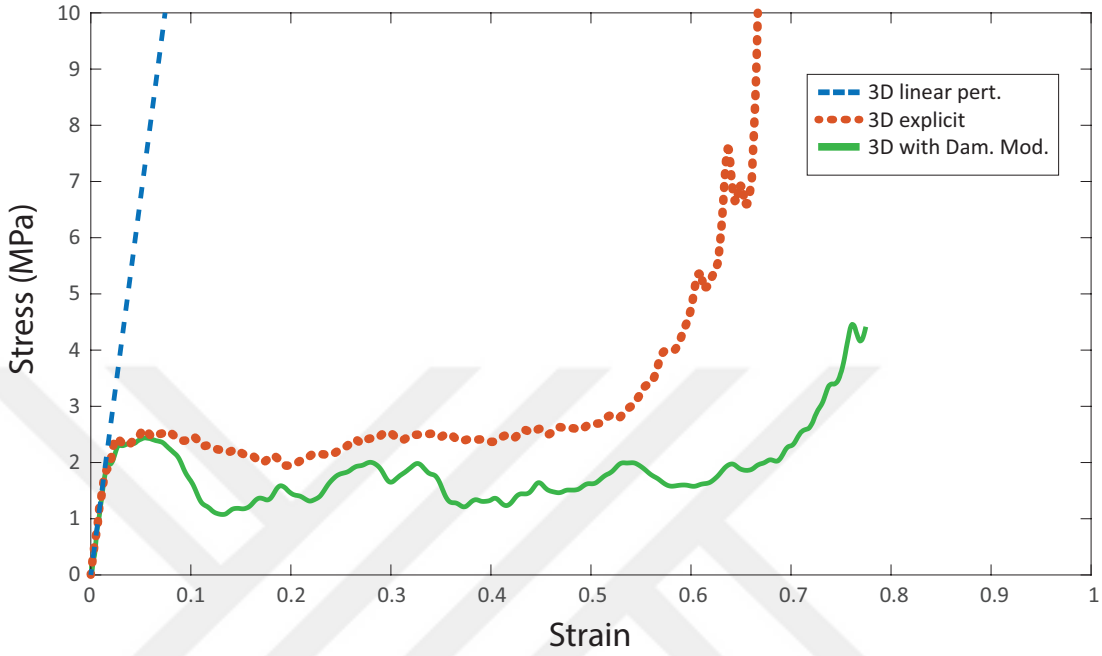


Figure 4.10: Difference in stress-strain behaviour of simulations done with 3D tetrahedral elements, with and without damage model. Linear perturbation simulation shows the elastic modulus of the SW lattice simulations.

model is shown in Fig 4.11. In order to achieve a better fit between the simulation and the experiments, material model of PLA material produced in different angles can be used, which we only used one of the angles. Since different production angles create vastly different material properties (which wasn't the case for EBM manufactured Ti-6Al-4V), inclusion of these difference would aid in the accuracy of the results. For comparison between all of the simulations together with the experiments, reader is referred to Fig 4.12.

The resulting optimized SW lattice has promising capabilities with 0.87 J/cm^3 energy absorption capacity, and specific energy absorption value of $SEA = 3.96 J/g$. In a previous study using the same PLA material a comparison between BCC, strut reinforced BCC and Dodacohedron lattices was done, and highest SEA among them was an optimized Dodacohedron lattice which achieved $3.217 J/g$. Thus SW lattice has 23% higher SEA. The compilation of various energy absorption metrics of the optimized lattice can be seen in table4.3 and its mechanical properties at Fig 4.13.

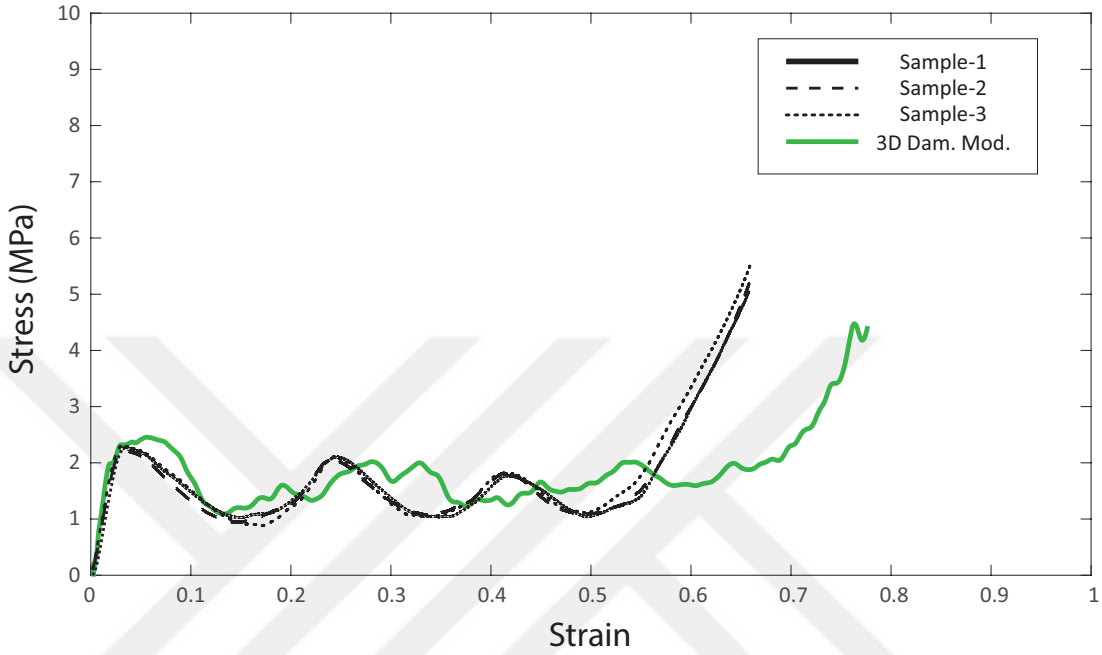


Figure 4.11: Comparison between the compression behaviour of three manufactured samples, and 3D simulation using damage model.

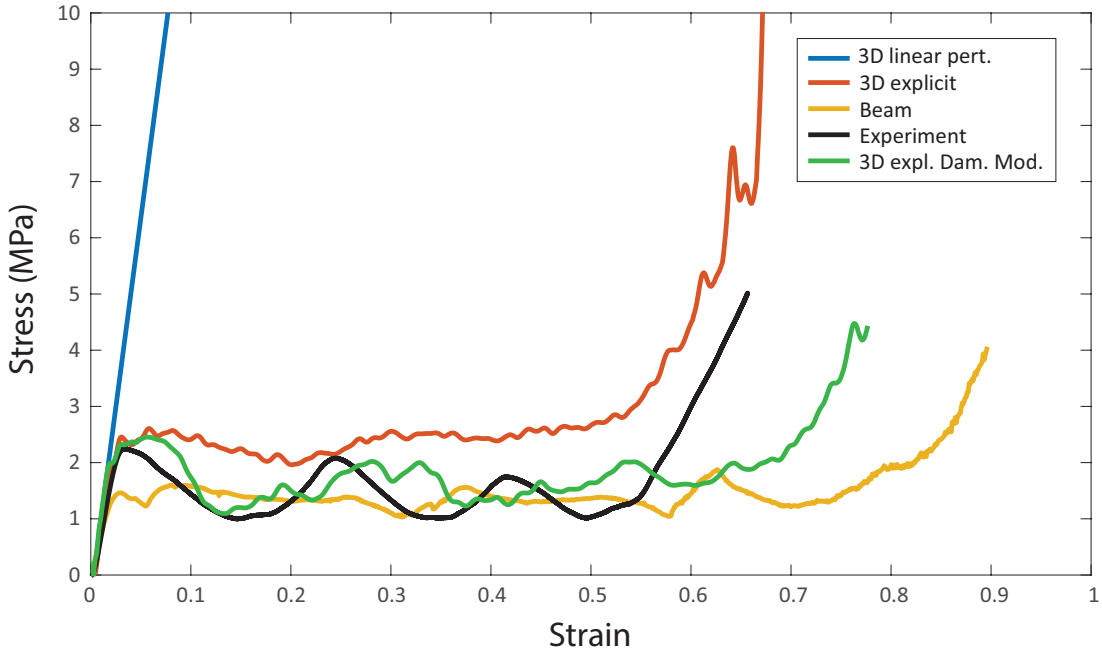


Figure 4.12: Comparison of the stress-strain curves of different simulations and the experiment.

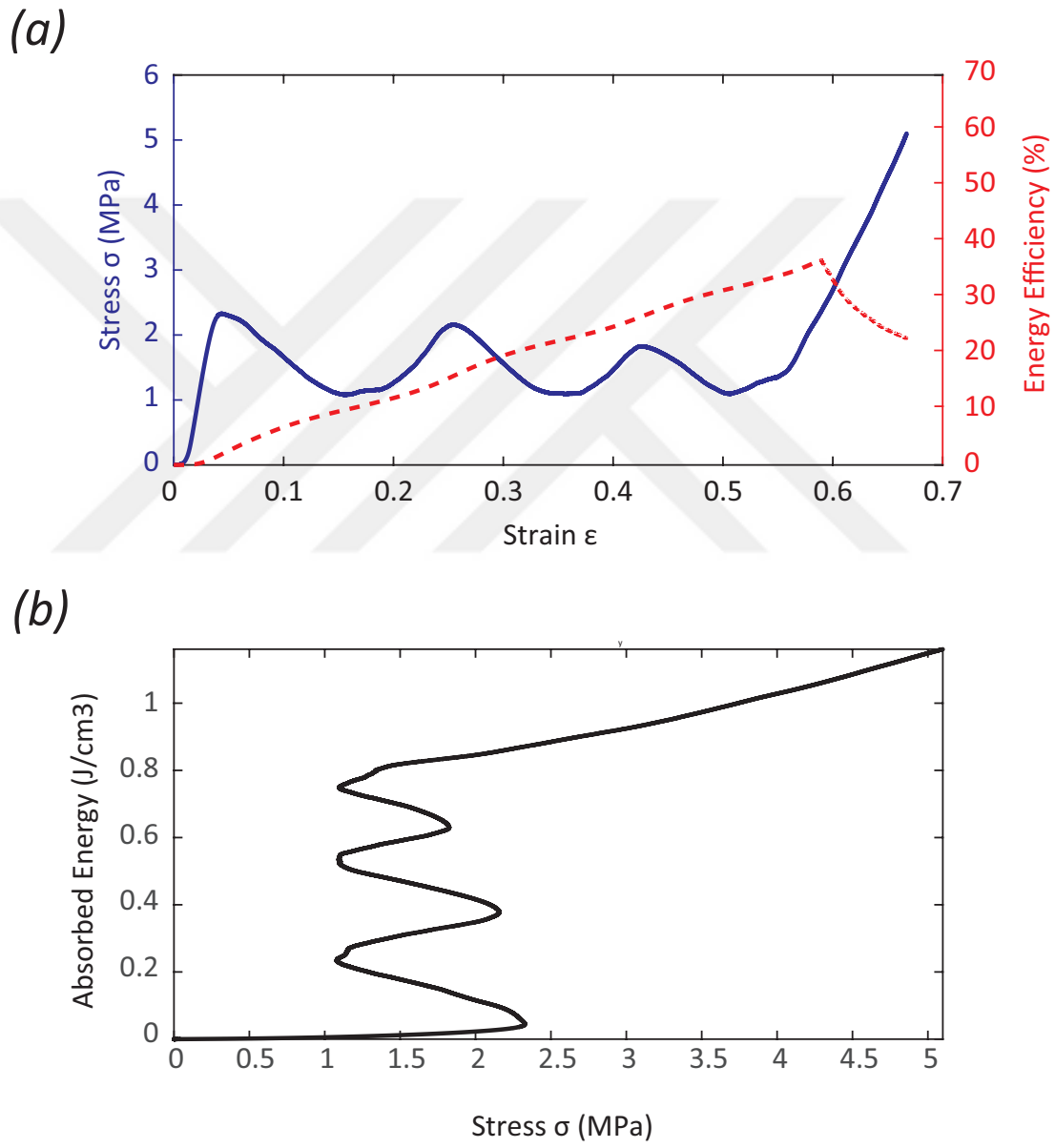


Figure 4.13: Mechanical properties of the SW-lattice, with stress-strain graph(blue) and energy efficiency graph (red) shown in (a). Cumulative energy absorption versus stress curve is shown in (b).

Table 4.3: Experimental Result of the optimized SW-lattice manufactured with PLA material

Yield Stress (MPa)	EA (J/cm^2)	SEA (J/g)	EAE (%)	σ_{pl} (MPa)	ε_d
2.32	0.87	3.96	37.33	1.52	0.59

Deformation modes of the 3D simulation with the damage model and the experiments are not exactly in line. Experiments show layer-by-layer collapse starting from top to mid, then the bottom. In our simulation, we see the first line collapsing first, but then the third line follows it rather than the second line. There are some similarities in the deformation shapes, however the positions they occur are different. This disagreement might be caused by the small number of cells we use for the lattice; a more converged collapse behaviour can be presented with more lattices. However, the most likely candidate for the dissimilarities in the deformation modes is the absence of different material properties for different printing angles of the lattice. The inclusion of the differences caused by the production angle would most likely produce better results due to the correct modelling of the fracture behaviour and mechanical properties of struts with different angles. A comparison of the deformation modes between the experiments and the simulation can be seen in Fig 4.14.

4.2.7 Ashby Map

In order to compare the energy absorption capability of the proposed SW-lattice to various infill designs reported in the literature, a volumetric energy absorption capacity versus density mapping Ashby chart is created. The materials used in these infill designs include PLA [91], PLA based composites[92], metallic foams[93, 94, 95], stainless steel[96], composite lattices[97], thermoplastic plate lattices[98], aluminium alloy[99] and titanium alloys[100] and some other materials that we omit for brevity. Additionally, Ashby map also includes data from sources:[72][101][102][103][104][105][106][107][108][109].

Compared to many polymer based designs, SW lattice shows superior energy absorption capabilities, and performs better than metallic foams such as Ni-foam

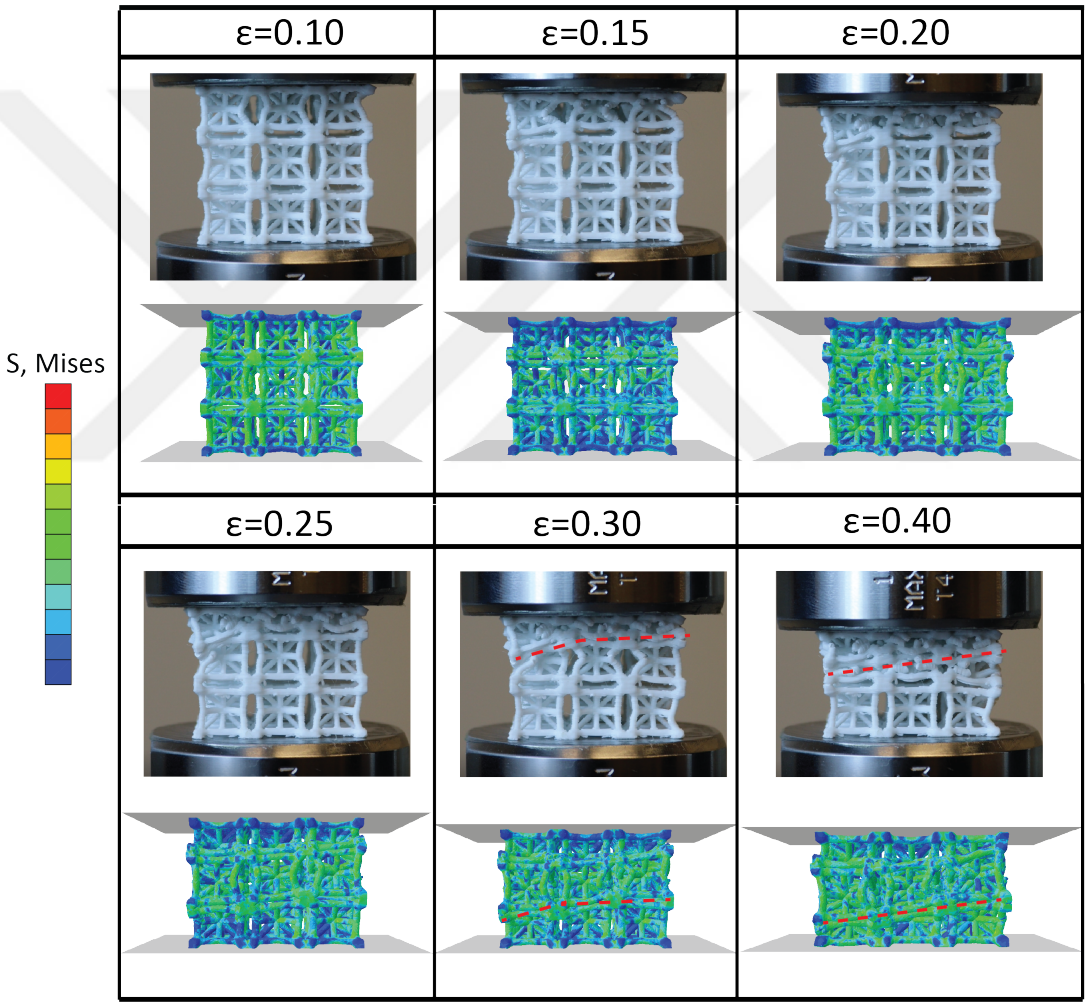


Figure 4.14: Comparison of deformation modes between 3D simulation with damage model and experimental tests.

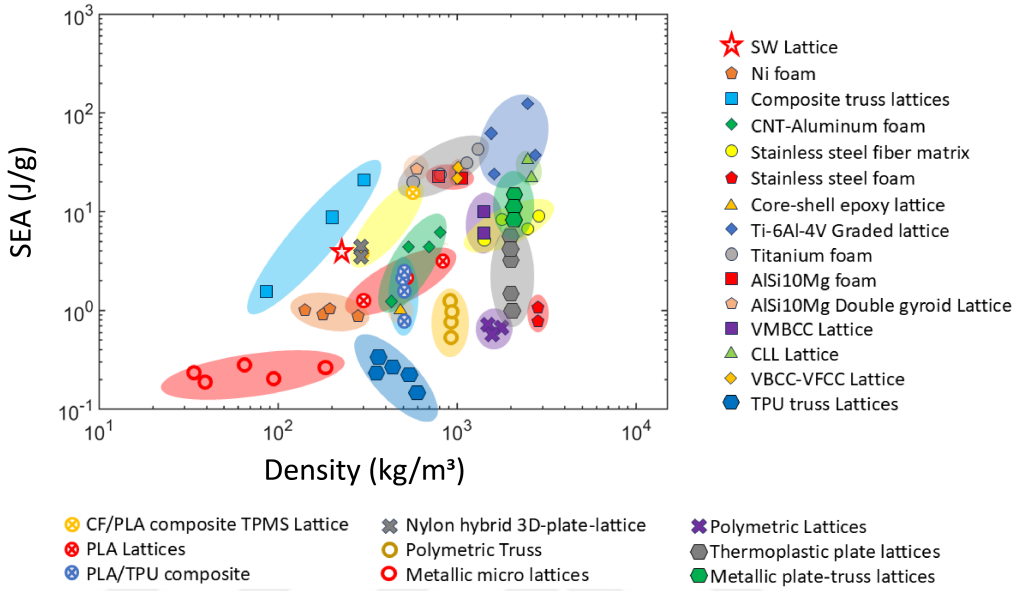


Figure 4.15: Comparison of mechanical properties of the proposed SW lattice with other architected infill materials presented in literature.

or some metallic micro lattices, while having comparable performance to carbon nanotube/Polymer composite lattices. For better performance, materials with superior properties such as composite materials or metallic alloys can be utilized.

4.2.8 Results for the Ti-6Al-4V based SW Lattice

This section covers the same methodology of design and optimization used with a different material, Ti-6Al-4V alloy manufactured using EBM. After optimization, compression simulations using beam elements with damage model is run. Experimental or simulations using 3D elements are not available.

4.2.8.1 Experimental Validation of Beam model

For the Ti-6AL-4V based lattices we have used beam model with Johnson-Cook damage model. In this case, we couldn't able to perform mesh analysis because of the beam contact thickness problem, which is enhanced when damage model

is involved. As mesh sizes get smaller, the plateau stress also gets smaller, thus a convergence is not achieved. However using 1mm mesh size, we were able to replicate experimental results of BCC lattice compression tests put forward by Guden et al. [13]. The comparison of stress-strain curves can be seen in Fig 4.16. Comparison between the modes can be seen in Fig 4.17. We've been able to have better agreement for the deformation modes between the simulation and experiments, since different material properties for different angles were available and was published by Guden et al. [13]. Another thing that should be considered is how little the material properties change for different production angles for Ti-6Al-4V, compared to PLA (table 4.2).

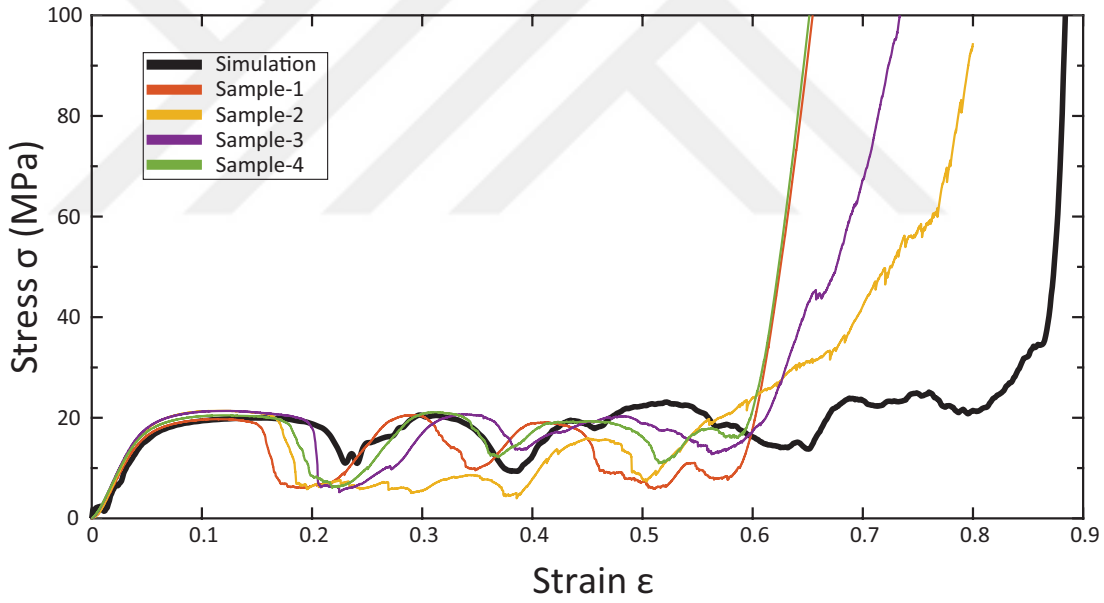


Figure 4.16: Experimental validation of the numerical simulations. The data of the experiment were shared by Prof. Mustafa Guden, which we are thankful for.

4.2.8.2 Optimization

The optimization step is the same as the lattice using PLA material. Using TS-EMO algorithm, a Pareto front using EAE and EA as objectives has been created. The resulting Pareto front is shown in Fig 4.18(a). After the Pareto option 5, the energy absorption capability shows a steep decline, so ideally Pareto-5 should be chosen as the optimal structure.

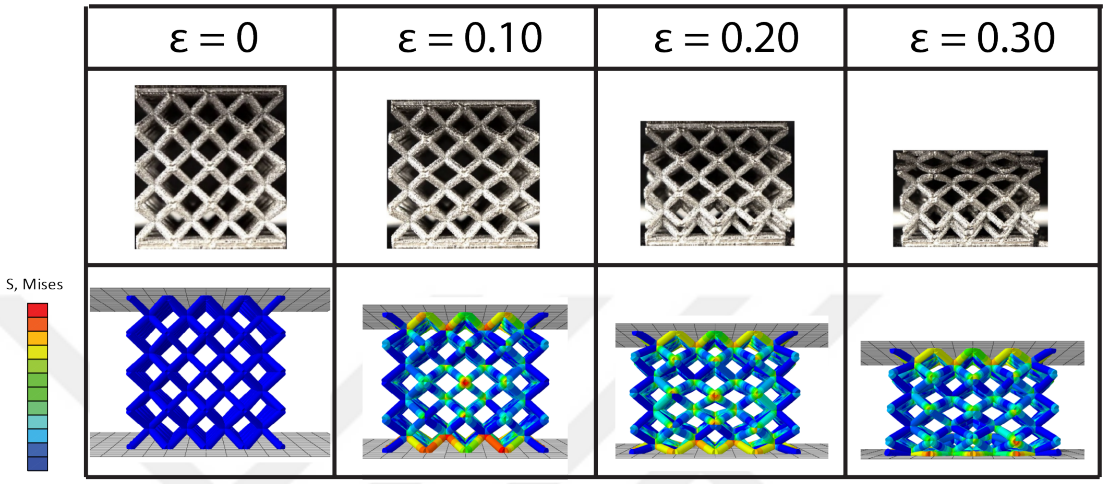


Figure 4.17: Comparison of the deformation modes between the experiment and simulation. Experiment pictures are from ref:[13], reprinted with permission.

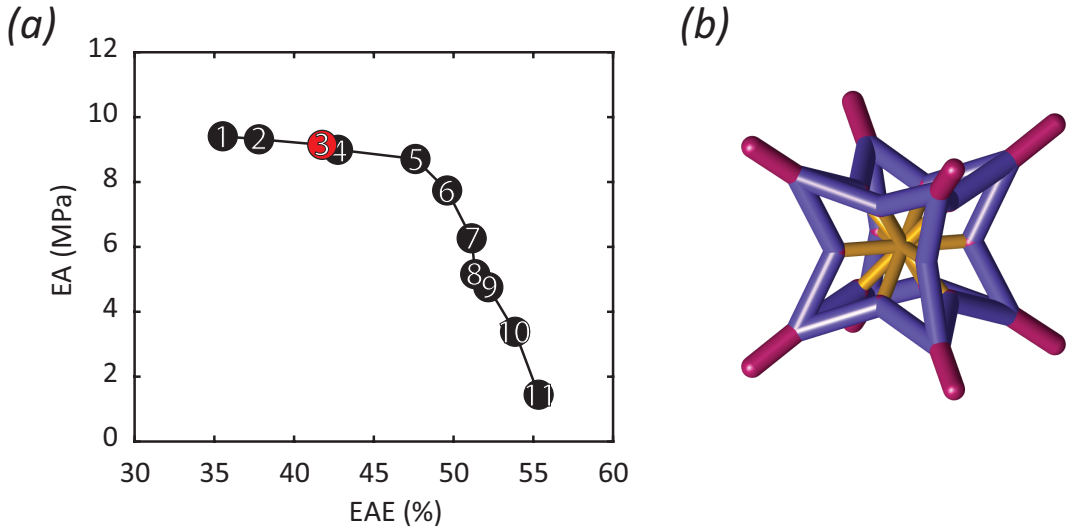


Figure 4.18: (a) Pareto front generated by the optimization [12], the chosen structure is shown with red dot. (b) Unit cell of the chosen structure, with parameters $rad2fr$: 0.86, $fr2an$: 0.66, r_{af} = 0.87, r_{fr} = 0.81. The results are for SW lattice using material property of Ti-6Al-4V alloy manufactured with EBM.

5x5x5 lattice models of the 5^{th}, alongside with the 4^{th} and 3^{rd} options were analyzed, which can be seen in Fig 4.19. 4^{th}, and 5^{th} options show an unwanted stress peak in the mid of the plastic region, so the 3^{rd} was chosen as the optimized structure. Mechanical properties of the chosen lattice is shown in Fig 4.20.

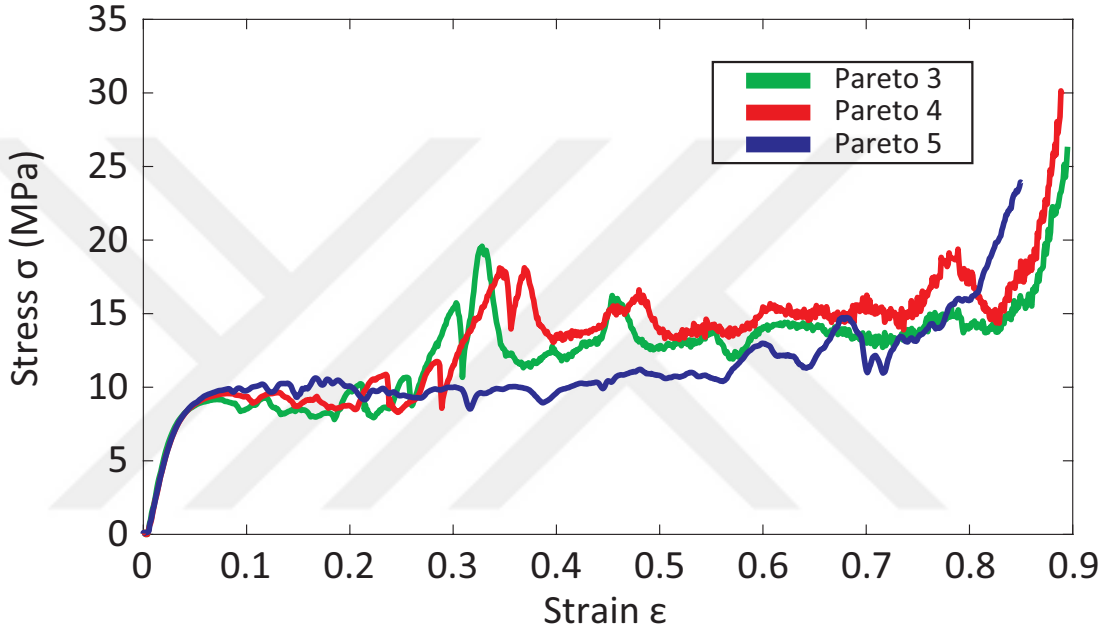


Figure 4.19: Results of the compression behaviour of 3^{rd}, 4^{th}, and 5^{th}, Pareto options.

4.2.8.3 Comparison of SW lattice to common lattices

While the aspect ratio of our struts are in the acceptable range, there is no guarantee for the accuracy of the results acquired from simulations using beam elements. However these results can still be used for comparison between different topologies. For this purpose, four conventional lattice structures were chosen. The lattice structures used were body centered cubic (BCC), face centered cubic (FCC), simple cubic lattice (SC) and octet lattices, and models of them at the same volume fraction (10 %) with SW lattice are created for simulations.

EBM manufactured Ti-6Al-4V alloy is quite brittle, so compared to SW-lattice, all these common lattices except BCC lattice show huge spikes in their stress

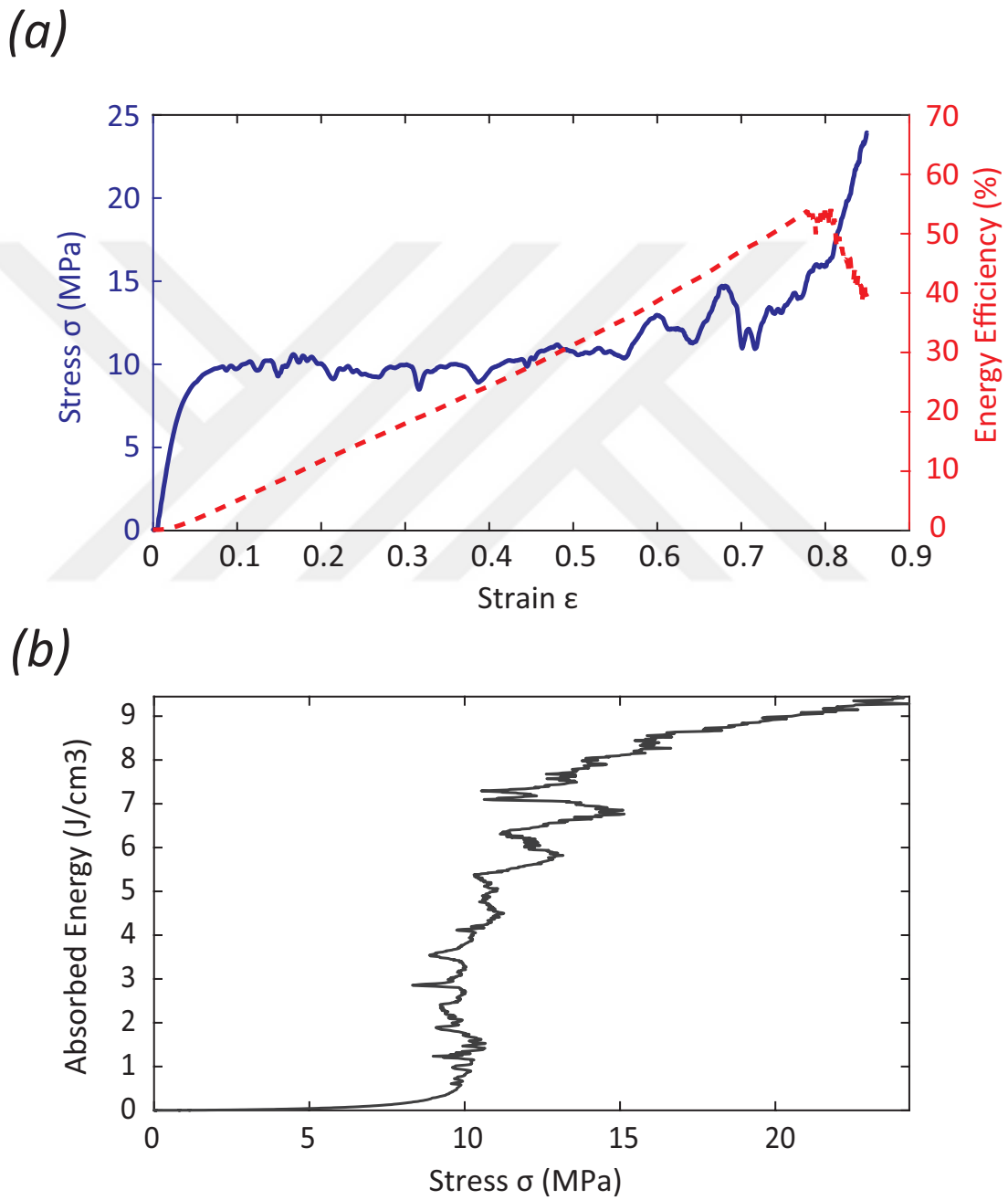


Figure 4.20: Results of the compression behaviour of optimized SW lattice with (a) stress-strain curve and energy efficiency curve and (b) cumulative energy absorption versus stress curve.

strain curve (Fig 4.21). This is caused by the sudden breaking of the struts, and complete failure of the layer. BCC lattice is a bending dominated lattice, and can withstand to larger strains without breaking. SW-lattice on the other hand, utilizes the same strategy the orb-webs are known for, by making the radii struts and anchor struts to not be connected directly, complete failure of the cell is less likely, thus the resiliency of the lattice increases. These features makes the SW lattice and BCC lattice closer to an ideal energy absorber.

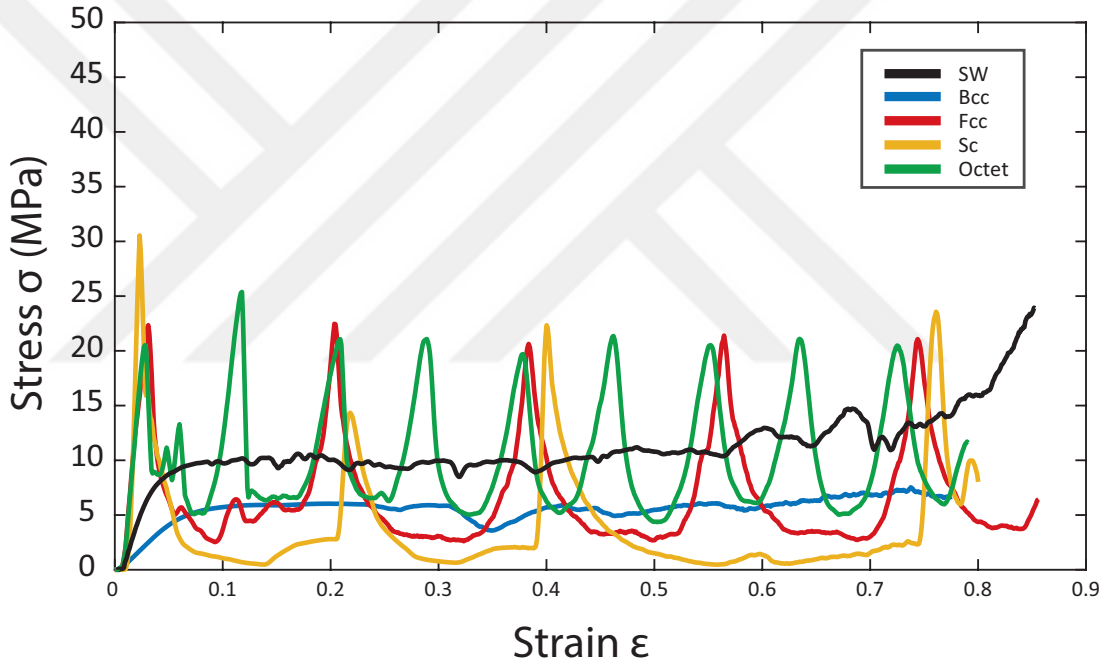


Figure 4.21: Comparison of the stress-strain curves of the SW lattice and four other conventional lattices.

Comparison of EA and EAE of the SW lattices are shown in Fig 4.24. SW-lattice, at the same volume fraction, show the best energy absorption performance. The octet lattice comes a close second place. However EAE of SW and BCC are a lot better compared to octet lattice. While EAE of BCC is highest among the compared lattices, SW lattice has around two-fold energy absorption capacity. This makes the SW-lattice best energy absorber out of the five lattice topologies.

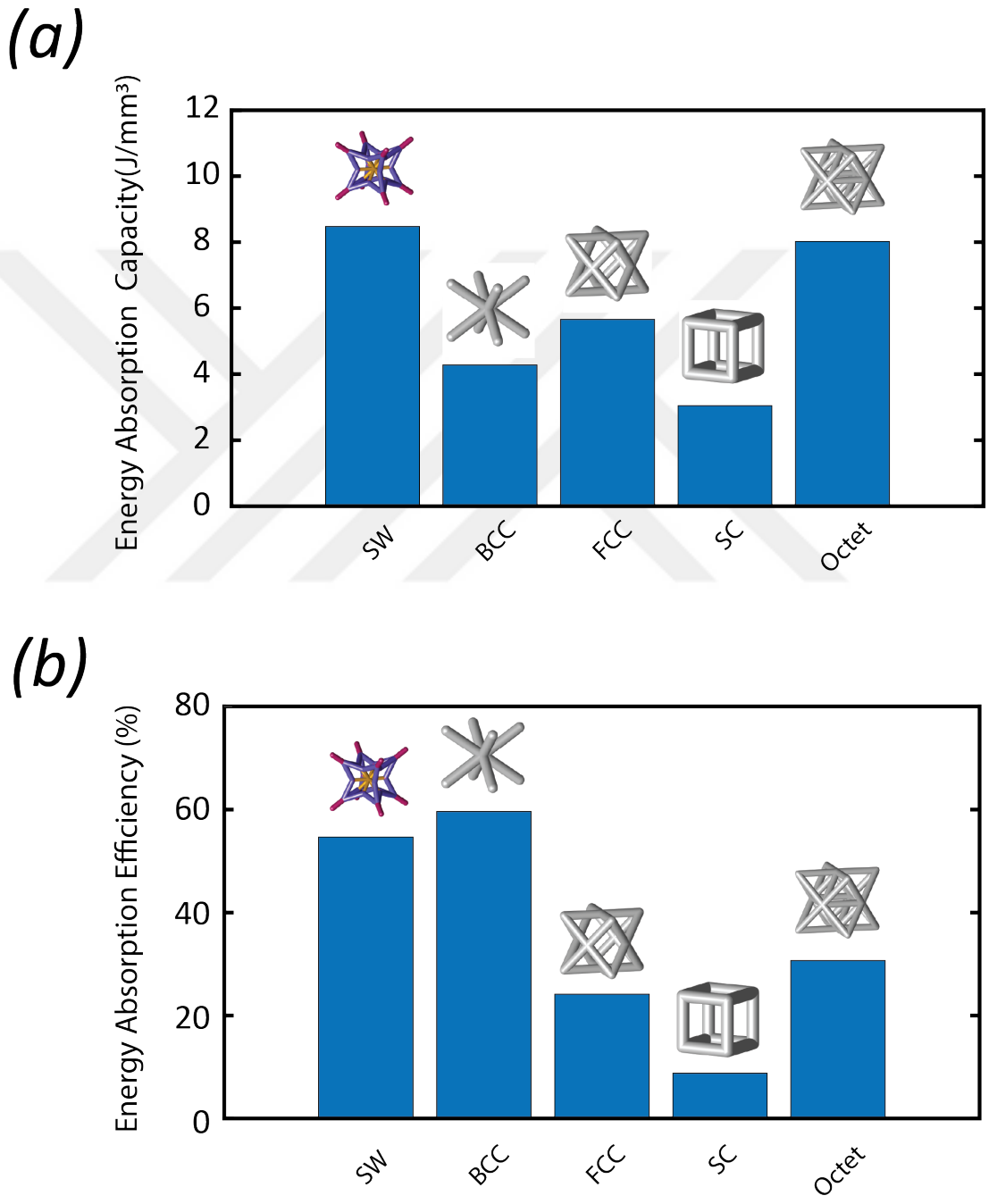


Figure 4.22: Comparison of mechanical properties between the SW lattice and four other conventional lattices are shown for (a) Energy absorption capacity and (b) energy absorption efficiency.

4.2.9 Ashby Map

Ashby chart of the designed Ti-6Al-4V SW lattice is shown in Fig 4.23. It shows promising results, however as it was pointed out, while comparison is good with beam models, the values can be off, and experimental validation is required in order to have accurate claims.

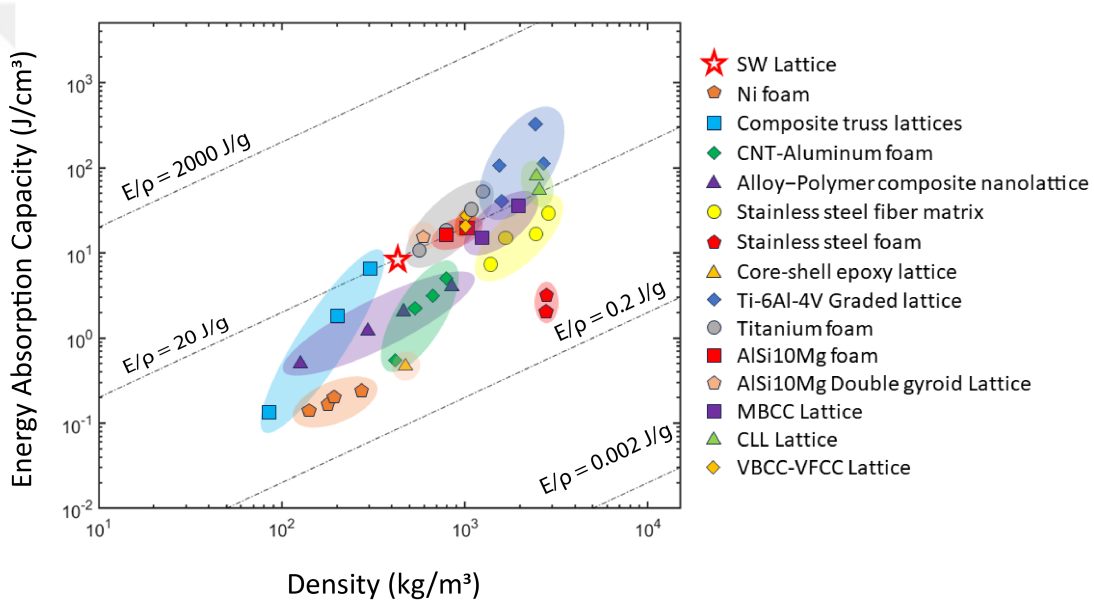


Figure 4.23: Comparison of energy absorption capacity of the designed SW lattice with other lattices reported in previous studies.

4.2.10 Conclusion

Inspired by the hierarchical structure of the spider web, SW lattice shows promising results for energy absorption applications. The hierarchical structure was implemented with different ratios between the struts, which were optimized to have desired qualities, such as high EA and EAE, in order to get closer to an ideal energy absorber. Our proposed lattice shows %23 better energy absorption capability compared to the dodecahedron lattice, which was shown with experimental results using PLA as its material. Also, simulations were done comparing

SW lattice to common lattices, which shows it has the best energy absorbing capability.

Non-linear dynamic simulations need substantial computational power; thus, using one-dimensional beam elements instead of three-dimensional elements saves time and reduces costs. However, three-dimensional simulations with accurate material models and experiments are required to get accurate results. Another thing to note is that the resulting lattices have different parameters, so the procedure we developed here should be done again for different materials.

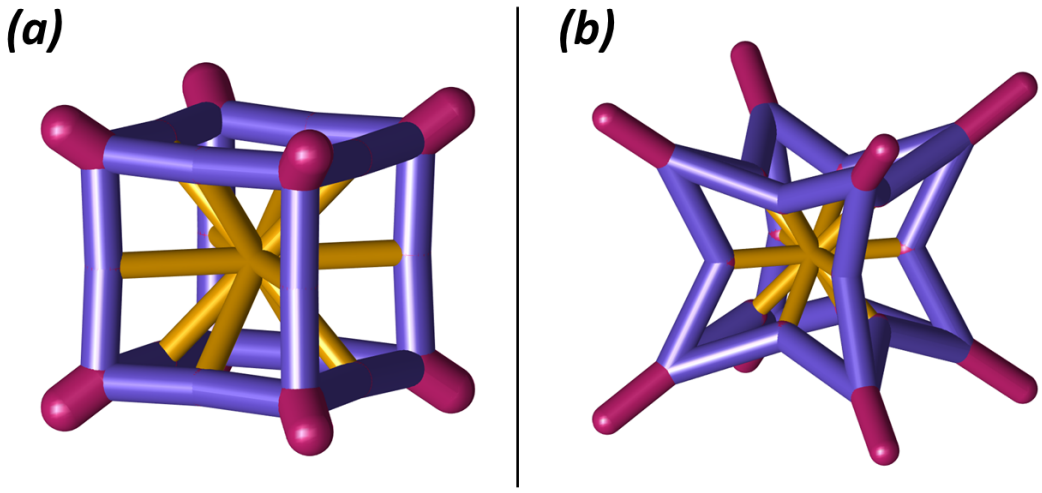


Figure 4.24: Optimized SW structure for (a):PLA and (b):Ti-6Al-4V.

Chapter 5

Effect of spider's weight on signal transmittance in vertical orb webs

5.0.1 Introduction

Spider orb web is a sophisticated structure that needs to fulfil multiple roles, trapping prey as well as transmitting web-borne signals. When building their web, heavier spiders tend to increase the pretension on the web, which seems counter-intuitive since a tighter web would decrease the chances of stopping and retaining prey. In this paper, we claim that heavier orb-weaving spiders increase tension on the web in order to reduce the attenuation of the vibratory signal coming from the bottom part of the web. We support our claim by first building a detailed spider web model, which is tuned by a tension-adjusting algorithm to fit the experimentally observed profiles. Then, the effect of the spider weight and the web tension on the signal transmittance properties are investigated using state-of-the art finite element analysis tools.

5.0.2 Spider Sense

Orb-weaver spiders use their web as a hunting tool, however as their visual perception is not well developed, they rely on their tactile senses, thus their web becomes their sensing tool. In order for the web to be a good sensory tool, it shouldn't hamper vibratory signals coming from any part of the web, as it would affect detecting and locating the prey negatively. In an orb web the radial threads extend from the hub to edge of the web. Thus a prey can be caught at any part of the web, and the vibratory signals they make can be picked up by one or many radii of the web and then reach to the hub. This makes hub the best place to sense disturbances and many orb-weavers prefer to sit at hub, waiting prey to disturb the threads (e.g., *Araneus diadematus*). Some spider species prefer to attach a signal thread to the hub, and wait in a retreat (e.g., *Zygiella X-notata*), so they can be protected from predators.

Spiders also have excellent tactile sense. Their exoskeleton possess mechanoreceptors called slit sensilla which picks up signals from any movement happening in the cuticle [110]. Slit sensilla are spread over the body, they can be isolated or arranged as parallel lines, which are called lyriform organs, referring to their appearence being similar to musical instrument, lyre. These organs are sensitive to strain and majority of them are near the spiders' legs. Sensory threshold of the slit sensilla belonging to a lyriform organ close to the distal joint of the tibia can be between 1.4 nm and 30 nm depending on the slit. And they can be activated for forces as small as 10^{-5} N [111]. These sensory organs allow the spider to sense wide range of vibrations caused by large and small insects, and locate them accurately wherever on the web. But there are still many things left unanswered about the process, and how the web affects the sensation process.

5.0.3 Signal Transmittance on Spider Orb-Web

The role of the web as a sensory tool and its relation to spider's sensing has been investigated with both experimental and computational studies. Klärner

et al (1982). showed that spiders could distinguish between airborne and web vibrations and observed predatory behaviour to both transverse and longitudinal sinusoidal vibrations [112]. Masters (1984) observed the attenuation characteristics of the signals on the web by creating vibrations on the prey-catching region of the web and measuring them near the hub [113]. Landolfa et al. (1996) observed how the geometry of the web affects the signal transmission [114].

Using finite element analysis, Mortimer et al. (2019) studied the wave characteristics and showed that the signal amplitude variance sensed by the spider legs is sufficient for determining the location and the direction of the source [115]. Otto et al. (2018) created both a physical and a finite element model of a spider web without the frame and anchors and studied the effect of the spider's mass and pretension of threads on the frequency response of the web [116]. Morassi et al. (2017) created a continuous membrane model [117], and studied the eco-localization of the prey impact using both a theoretical model and finite element model [118].

Previous numerical models provide valuable information on the signal transmission on an idealized web. However, lack of precise control on the pretension in the web threads prevents comparative studies to understand spider's web-building behaviour from being carried out, such as adjusting the tension when building in windy conditions [40] or weight increase [16]. To our knowledge, accurate pretension adjustment of each element on a finite element analysis of an orb web model with anchor, frame, radii and spiral has not been done. Thus, there is a lack of studies on how the weight of the spider and the tension of the web affect signal transmission.

In this study, we present an algorithm to calculate the pretension of the threads to accurately represent a natural spider orb web and the effect of the spider's weight on signal transmission. Our results show that spider's weight changes the tension distribution of the web, which results in poor signal transmittance on certain threads and affects prey eco-localization negatively. Our results suggest that the direct relation between the web pretension and spider's weight might be related to correcting these issues.

5.1 Methods and Models

The spider web structure used in this study is modelled after *Araneus diadematus* orb web, which has four main structural parts: anchor (or mooring), frame, radial and sticky spiral (Fig.1). Anchor, frame, and radial threads have materials with properties different from those of the sticky spiral, the latter being more extensible and less stiff [79] with each having different thickness and pretension values. Using geometric parameters and pretension values found in literature and implementing the nonlinear mechanical behaviour of spider silk, the model tries to emulate natural webs as closely as possible while using a few simplifications. This model is then subjected to periodic finite deformations representing a captured prey's struggle in the web. Considering the nonlinearities in the system with finite deformations under a short duration, using a finite-element analyzer with an explicit integration scheme would be appropriate. For this purpose, simulations were conducted using Abaqus/Explicit 2020.

This section describes how the model is created and the methodology of the simulations.

5.1.1 Geometry of the orb web

The spider web model has five anchor threads connected to five anchor points that act as the rigid support of the whole web, and they are positioned at equal angular distances from each other. The radials also have equal angular distance between them before pretension; however, after the pretension is applied, frames concave inward, and the angular distance between them changes. The spirals were simplified to concentric circles with a constant distance between them.

Natural orb webs generally have a distinct hub architecture [119]; however, neither the tension values of the threads in the hub nor their specific architecture are studied in detail in the literature, so the radii connect in the hub on a single node. The spider's weight and mass are applied to this node to simulate the effect

of a spider sitting on the hub.

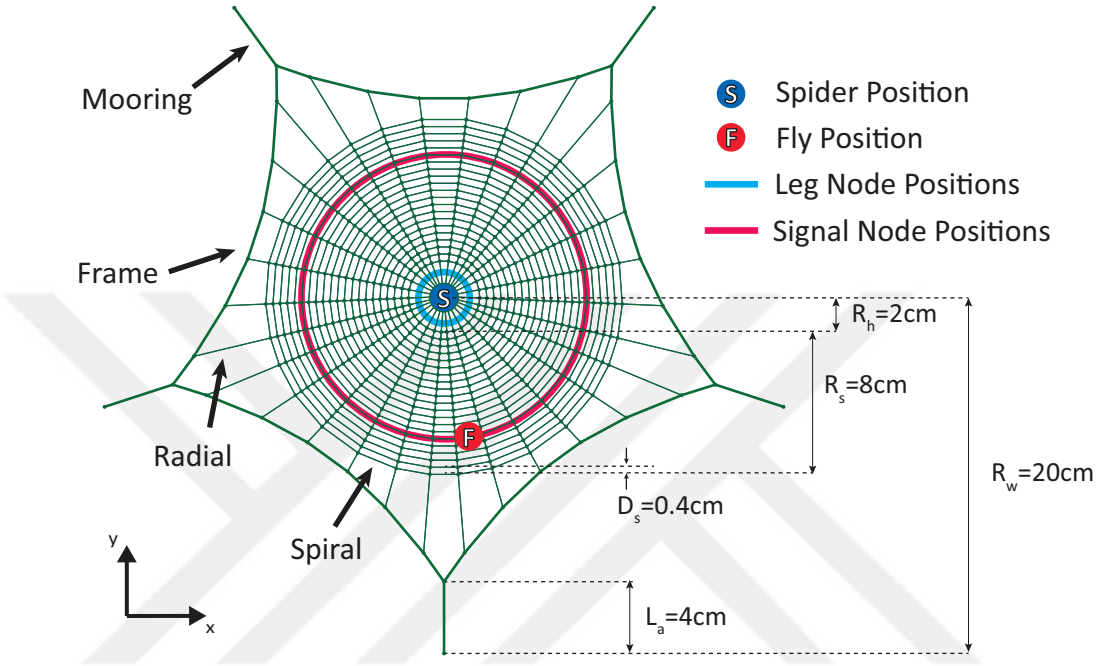


Figure 5.1: Spider web model used in this study with geometrical parameters. Solid cyan lines show possible positions where the spider can detect incoming signals which are called leg nodes. A fly can be captured at any point on the solid magenta line which is called a signal node.

5.1.2 Modeling the silk

Spider silk has non-linear material properties, which can be characterized by the microstructure-based continuum model proposed by De Tomassi et al. (2010) [33]. This model considers the silk to have two basic parts, a hard and a soft fraction. The soft fraction refers to the amorphous network that shows entropic elastic behaviour, and the hard fraction refers to the ordered network that is rich in stiff crystals, made up of polyalanine sequences arranged in β-sheets, which can form hydrogen bonds. As the silk protein chain is stretched beyond a certain limit, the hydrogen bonds of the hard fraction start to break, transforming into the soft fraction, thus increasing the contour length. Both fractions are included in the calculation of the stress-strain behaviour; the soft fraction is considered to be

always active, while the hard fraction consists of active and inactive phases. This study uses a modified version of this model, which was employed in a previous study by Soler et al. (2016) [10].

5.1.3 Pretension procedure

Our goal is to compare various realistic tension distributions with respect to spider weight. To achieve this, we developed a method that systematically tunes pretensions of the threads to a desired profile based on experimental studies on *Araneus diadematus* [80]. Utilizing the material model described in the study by Soler et al. (2016) [10] and using the diameter value of the different silk types presented by Lin et al. (1998) [80], a Matlab algorithm is created to calculate the initial lengths of spiral and radial threads. The algorithm adjusts the length l of each element of the adjusted group in the model to get the desired tension value, $T_{ag} = T_{spi}$ for spirals and $T_{ag} = T_{rad}$ for radii. First, the tension of each element T is found and is compared against the desired tension value T_{ag}. If $T < T_{ag}$, the original (unstretched) length of that element is decreased by an amount δl, which increases its tension. For the opposite case of $T > T_{ag}$, the original length is increased by δl. If T oscillates near the target value, δl is divided by a constant $c_1 > 1$ to get closer to T_{ag}. Otherwise, δl is increased by a constant c_2 to speed up the convergence. The algorithm flowchart is shown in Fig.2. To apply pretension to the whole web, firstly, radii are tensed in a model without any spirals. After adding spirals, the same algorithm is applied to them. The frame and anchor lengths are not modified, and the tension value of the anchor and frame threads are the result of the adjustment of the radii and spiral tensions.

The tension values used in this study are $T_{spi} = 10\ \mu N$ and $T_{rad} = 100\ \mu N$. The resulting average pretension values after the calculated thread lengths are implemented in Abaqus can be seen in Table 1. The radials have different tension values at different parts due to the tension of spirals, and the radial tension is higher than average close to the frame and lower close to the hub, due to the concavity of spiral threads towards the web centre. The average radii tension

close to the frame is 122 μN, and the average spiral tension value is 9.7 μN, which are compatible with the values presented by Lin et al. (1998), 132 μN and 10 μN respectively [80].

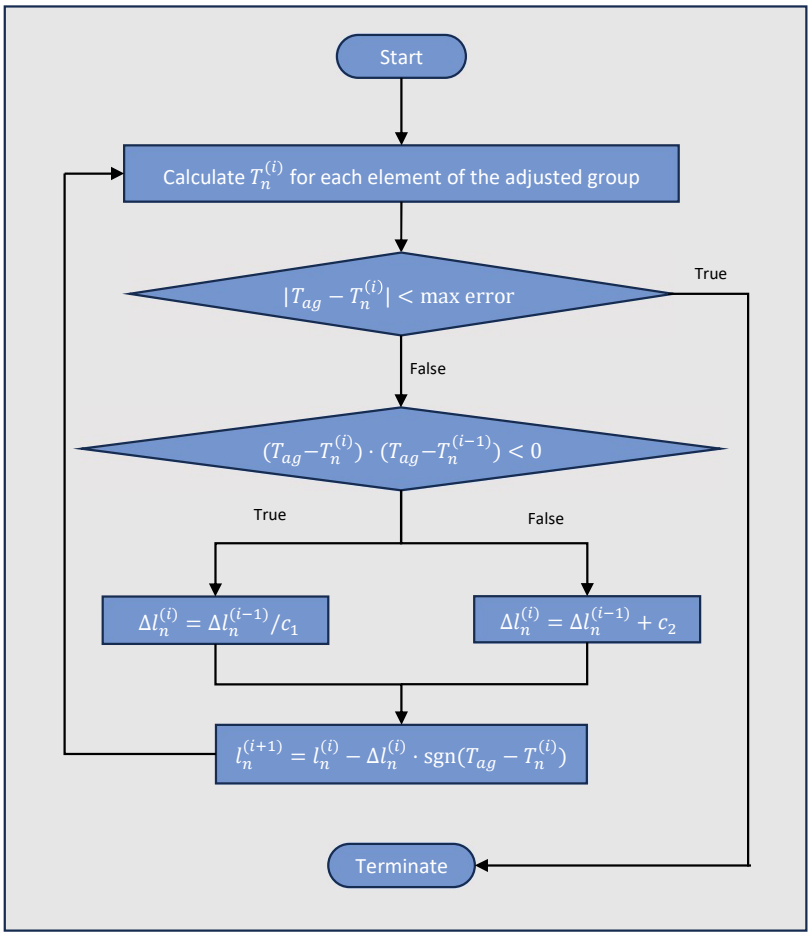


Figure 5.2: Tension adjustment algorithm flowchart.

Table 5.1: Pretension values and diameter of the threads in the model.

Type of thread	Diameter (μm)	Average pretension (μN)	Standard Deviation
Spiral	2.4	9.7	0.11
Radial	3.93	102.5	15.7
Frame	7.23	962.5	62.0
Anchor	8.03	1741	0.66

5.1.4 Modeling the prey

The prey is considered to be a fruit fly stuck to the centre node of the sticky spiral thread that has a distance of 8 cm from the hub. Possible positions of the fly are called signal nodes. The average weight of the fruit fly is 10 μN (BNID 110030; ([120])), which is simulated as a constant downward force at the "signal node" that corresponds to the position where it got stuck. In order to simulate a prey struggling on the web, the signal node is moved in a sinusoidal pattern with 1 mm amplitude at 200 Hz, which is used by Wignall et al. (2011) in real spider webs to create predatory behaviour [121] and is close to the wingbeat frequency of *Drosophila Melanogaster* [122]. The signal node is moved in three ways; for transverse waves the node is moved perpendicular to the web plane, for longitudinal waves it is moved in-plane towards the hub, and for lateral waves the movement is parallel to the spiral it is connected to. The spider is thought to be able to sense the excitations on the radii from points close to the hub, which are referred to as leg nodes. These excitations can be the tension changes on the web silk, or displacement of part of the silk that is under tension. The possible positions of signal nodes and leg nodes can be seen in Fig.1.

5.2 Effect of spider's inertia and weight on signal transmission

The presence of the spider at the centre of the web affects the mechanical response of the web in two different ways. On the one hand, the spider's inertia modifies the system's dynamics and thus the transmission of waves that help the spider recognize the direction of the signal source [118]. On the other hand, the spider's weight exerts a load that alters the distribution of pretensions on the web, which also translates into a modification of its dynamic response, affecting the transmission of the dynamic signal. We wanted to decouple the effect of inertia and the load to understand the effect of each, since for some of the orb weaver spiders such as *Zygiella x-notata*, the spider is not present at the centre, but it

attaches a signalling thread to the hub which it keeps under tension. This behaviour presents a case where only a load is present at the centre of the web. The simulations from Mortimer et al. (2019) showed that this signalling thread does not contain any directional information [115], which is consistent with the observation that once the spider senses a motion from the signal thread, it first runs to the hub, and only then does it heads towards the source of the vibration [112]. In our simulations for transverse waves, we observe a minimal difference in the displacement of radials near the hub when no inertia is present at the hub, even when its weight is present as a downward force at the hub (Fig.5.3(i)). When the spider's inertia (along with its weight) is included, some of the energy created by the vibration is spent accelerating the spider's inertia. This obstructs the vibratory signal and it is not transmitted past the hub, thus directional information becomes much more precise. This is consistent with the result presented by Zaera et al. (2022) [118], but in their model, no weight force was applied. Our result shows that this effect is observable even in vertical orb webs when the spider's weight is applied. Similar precision betterment by inertia can be seen for other wave types, lateral (Fig.5.3(ii)) and longitudinal, albeit to a lesser extent. While we didn't simulate the exact leg structure of the spider, it is not an overstatement that this displacement can induce a strain change for the spider's leg which can stimulate a response from it. However it is not exactly known to us, and as far as I am aware there is no such study in the literature, how the displacement on the web would affect the leg of the spider. Spider's leg, with its inertia would certainly be affected by the displacement of the threads. We should also be considering the pulling the threads which is a very characteristic behaviour. Thus our results at Fig.5.3 should be analysed with this theory in mind, the expected sensation perceived by the spider would be the combination of both the stress and displacement change, however the ratio of the mixture is not something we can have a definite answer with our current understanding.

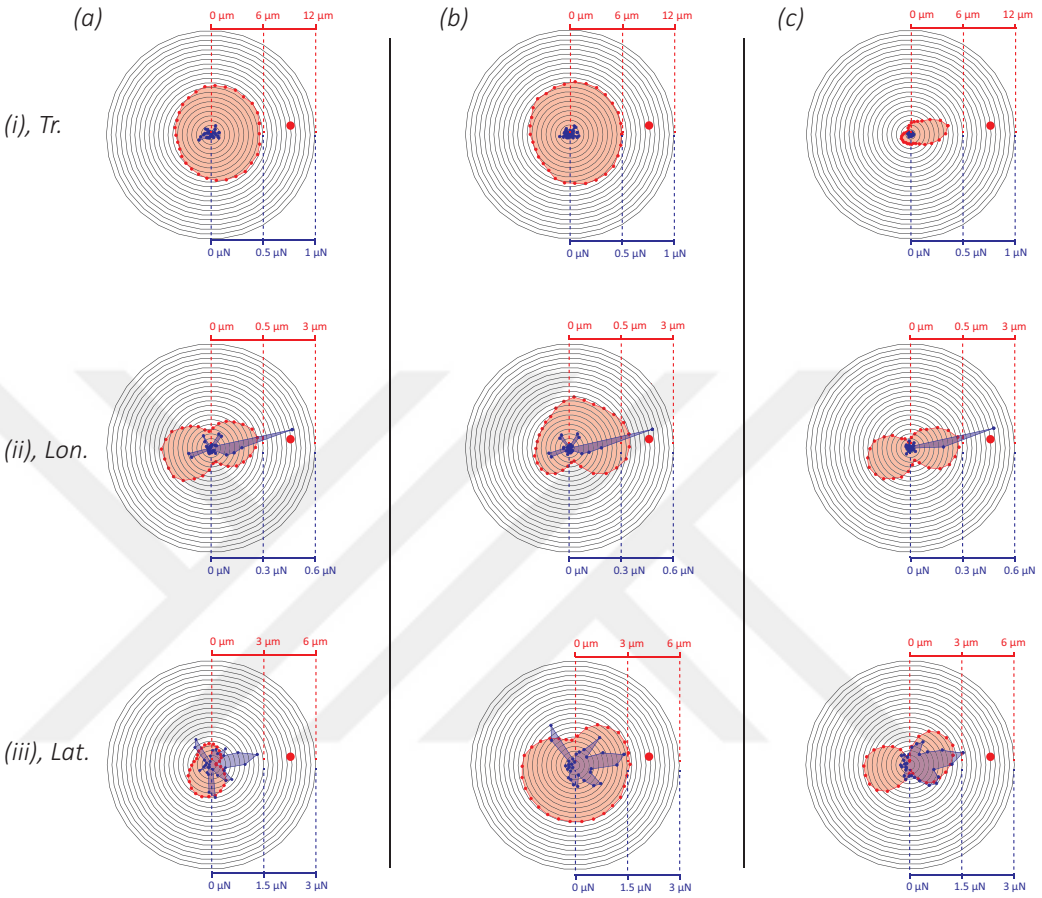


Figure 5.3: Displacements and tension change values near the hub, shown by the red and blue colours respectively, caused by the signal source located at the red dot. Web's response to transverse excitation is shown at (i), to longitudinal excitation at (ii) and to lateral excitation at (iii). In the case of (a), no mass or weight force caused by the spider is applied to anywhere in the system. (b) shows spider web with 490 μN downward force applied to the hub but no inertia and (c) 50 mg spider at the hub. For transverse waves tension change on the radii are tens of nano newtons at maximum, and do not show any significant change for different cases. The displacement is affected by addition of inertia and positional information for the signal location becomes significantly better compared to no inertia case. Similar observations are present for the tension change values due to the lateral and longitudinal waves.

5.3 Effect of spider's presence on the hub on signal transmission

Tension on the web and signal transmission are related. On a single strand of silk, larger tension lowers the signal attenuation [123]. This phenomenon seems to be used by spiders, an orb weaver from family Uloboridae, *Octonoba sybotides*, increases the tension on the web when hungry, which allows it to sense smaller prey [124]. *Cyclosa octotuberculata* pulls the radii while waiting for prey, which increases its chances of sensing and catching the prey [125].

Heavier spiders build webs with higher tension [16]. This is a counter-intuitive response since higher tension on the threads would diminish the spider's chances of stopping and retaining prey [40], [41], and since the majority of the orb weavers sit at the hub, upper radii would have even higher tensions compared to a lighter spider web. We hypothesize that this behaviour might be related to the spider's sensing abilities. As the spider sits on the hub, the tension on the bottom radials would be smaller, and on the top, it would increase. Spiders generally put more importance on the bottom part of the web; the majority of vertical orb web-building spiders sit face downwards on the hubs of their webs, and as the spider gets heavier, it builds webs with more vertical asymmetry where the area of the bottom part is larger than the top part [39], [37]. This is thought to be a result of the spider's ability to run faster downward compared to upwards, and vertical asymmetry is a way of optimization for catching prey as it can reach every part of the web at similar time periods [126]. The bottom part is also different structurally, there are more radials at the bottom and the spiral mesh is denser [127]. Material investment can also be different, which is the case for *Araneus diadematus* webs. Ecribellate orb spiders such as *Araneus diadematus* cover their spirals with a sticky aqueous solution that acts as a glue to ensnare prey caught on the web [128]. This aqueous glue coating quickly forms droplets which are significantly larger at the bottom part [129], thus increasing the chances of capturing prey. These features point to the bottom part of the web being more valuable for catching prey. Therefore, the spider needs to be able to distinguish

signals coming from the whole web but specifically from the bottom part.

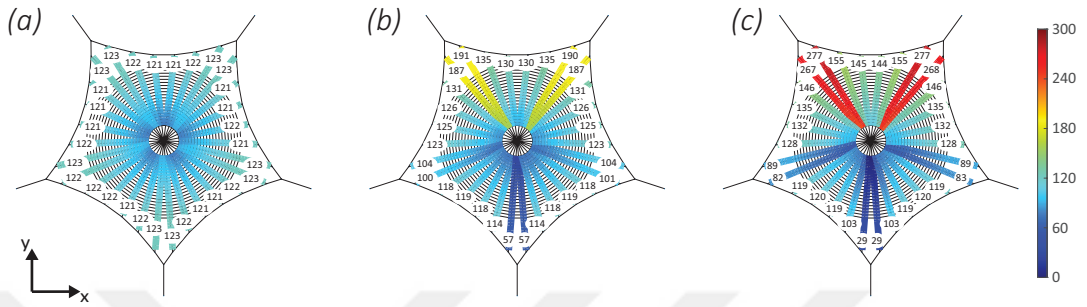


Figure 5.4: Prestresses in the web with $T_{rad} = 100\ \mu N$, (a) no spider present at the hub, (b) 490 μN and (c) 980 μN weight applied at the web centre, representing two different spider's weight in y direction. The numbers present the pretension values of radii close to the frame. All the values shown including the colorbar have units of μN.

In a vertical orb web, the weight of the spider creates a tension variance on the web, with tension values decreasing below the hub and increasing above (Fig.4). If the mass of the spider is higher than 75 mg, the tension of the bottom radii gets so small that the segments close to the hub start to sag and signal transmission to the hub is eliminated completely.

Decreasing tension on the radii negatively affects signal transmission, which can be seen by the responses generated by the all three wave types (Fig.5). This may adversely impact prey capture, especially for a small prey that would generate lower amplitude signals.

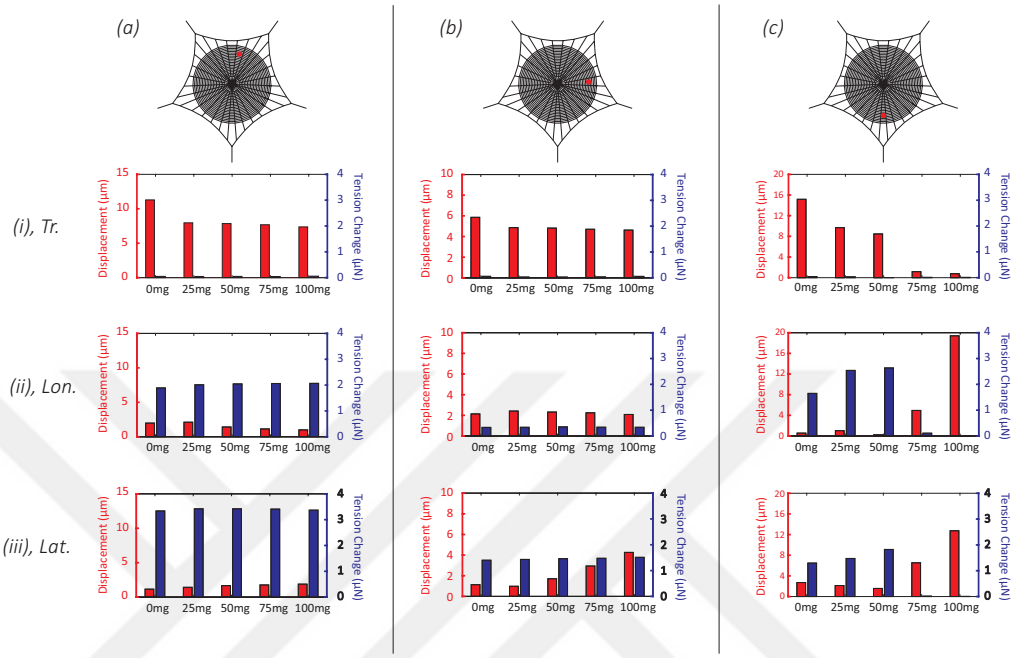


Figure 5.5: Average displacement and tension change of leg nodes on two radii closest to the signal location is shown with changing spider mass for $T_{rad} = 100\ \mu N$. The signal source is located at the bottom region, shown by the red dot on the spider web model (a), and the wave type of the vibration are transverse, longitudinal and lateral for (b), (c), (d) respectively. For transverse waves the displacement decreases as the mass of the spider increases. For lateral and longitudinal cases tension change is not observable for 75 mg and 100 mg cases and the increase in displacement comes from the silk that sags, and is not under any tension.

In order to confirm the previous statement, contour maps of signal transmission amplitudes for different spider masses and radial pretensions are shown in Fig.6 for transverse waves and in Fig.7 for longitudinal and lateral waves. One can see that increasing the radial tension indeed recovers the previous signal amplitudes near the hub. When a part of the web is loose, locational information is lost, which can be seen in the web models presented in Fig.6 and Fig.7. If signal is not transmitted properly from every part of the web, the excitations coming from the other radials might direct the spider onto the wrong sectors of the web, or the signal can be too weak to detect.

All the wave types are affected by the signal transmission problems caused by silk with very low tension, however their responses to higher tension differ. Transverse waves are positively affected by the higher web tension and lateral waves are affected negatively. Out of the three wave types, longitudinal waves are the least affected by the tension change.

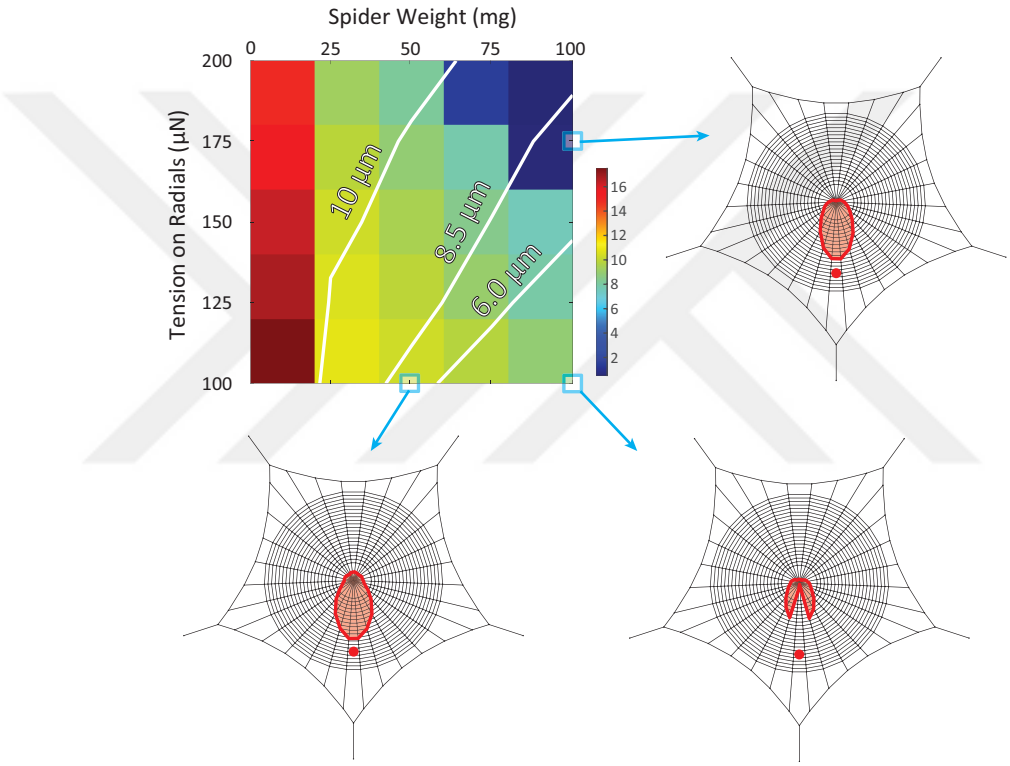


Figure 5.6: Contour map of signal amplitude with respect to the spider weight and radii pretension (T_{rad}) for the vibration generated at the bottom part of the web, with white lines showing the equivalue points. Three points on the map are shown as web models. The signal source is shown as the red dot and the displacements on the radii are shown with red solid lines, where a larger distance from the hub represent larger value on the radial.

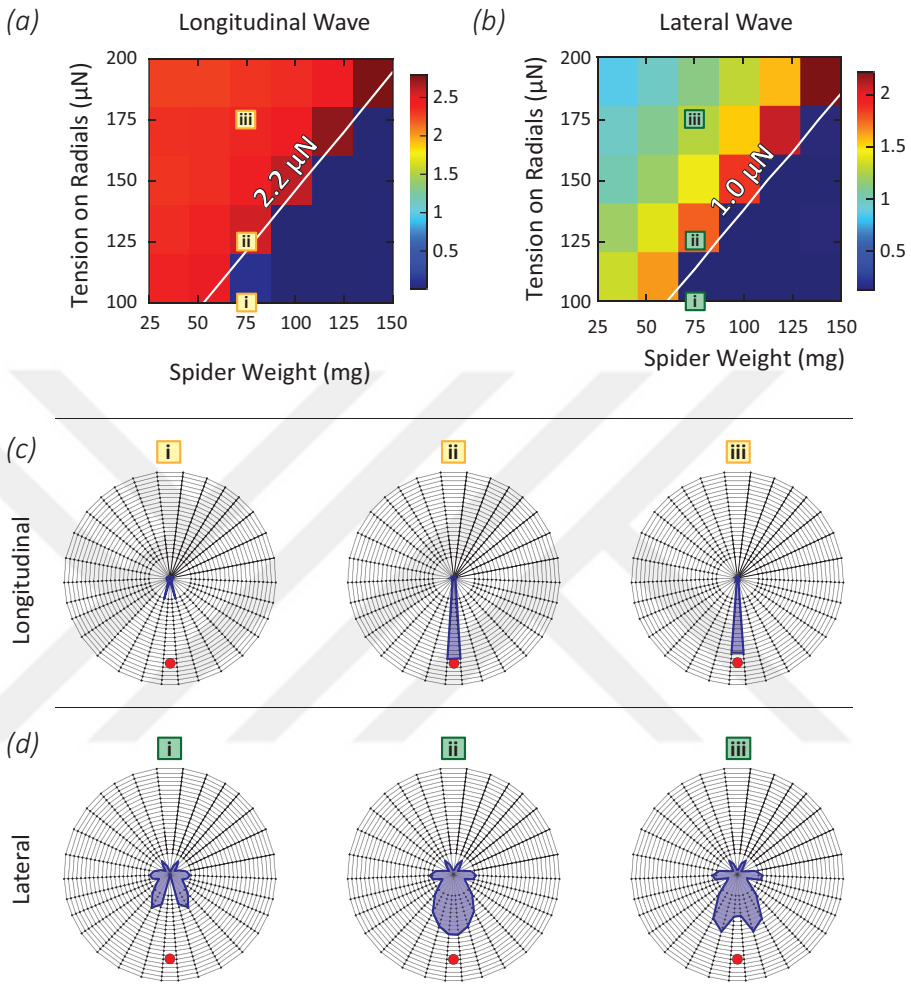


Figure 5.7: Contour maps for (a) longitudinal and (b) lateral waves. The signal amplitude is represented as tension change on radii, with colorbar representing the values with units of μN, plotted with respect to spider weight and radii pretension (T_{rad}). Model representation corresponding to the areas marked on the contour map are shown below, (c) for longitudinal and (d) for lateral waves. The signal source is shown as the red dot and the tension change on the radii are shown with blue solid lines, with greater distance from the hub representing a larger amplitude. The signal amplitude created by the longitudinal waves do not seem to change much with changing tension (a), however as the tension on the radii becomes too low the signal is completely lost. Lateral waves also lose signal transmission below a certain (radii tension)/(spider weight) ratio threshold as seen in (b). Unlike the longitudinal excitation, for the lateral excitation case, higher tension of the radii affects signal transmission negatively, and the locational information becomes less precise above a certain value.

5.4 Conclusion

Using a web model with accurate mechanical non-linear silk properties and controllable pretension, we tried to explain the seemingly contradictory behaviour of vertical orb web weavers building higher tension webs as their weight increases. Our results support our hypothesis that this tension increase is required for the web to transmit vibrations created by captured prey and for the spider to locate its position correctly. We show that when the radial thread tension is low and the spider's weight is high, the web can generate confusing responses by eliminating signal transmission from certain parts of the web. The direct relationship between the signal amplitude and radii tension might also explain the observations made for spiders such as *Cyclosa octotuberculata*, which tenses the radii to increase its chances of detecting prey [125]. Another takeout from this study can be the crucial effect of the spider's inertia assisting in finding the direction of the signal source, which might explain the behaviour of spiders such as Zygiella x-notata first arriving at the hub after sensing a vibratory signal through their signal thread, instead of choosing the shortest path [130, 131].

This study highlights the effect of spider's weight on the tension distribution of the web, which in turn affects the spider's web-building behaviour. Spider's web is considered a sensory organ of the spider in addition to being a trap for prey capture, and spider's own body seems to be linked to its functionality, as discussed in the previous chapters. Our spider web model can be further improved for more realistic results. Different hub architectures can also be included, which might have different properties for improving signal transmittance; however, experimental studies on this particular part are lacking. Another structural simplification in our model is the lack of asymmetry that is naturally present in vertical orb webs, where the bottom part would be larger as the spider gets heavier. The effect of weight on the tension distribution of the web is most likely to be more pronounced in asymmetric webs due to the larger bottom sector with more radii compared to the top. There are various modifications spiders make when a parameter like the weight is changed due to the many roles that the web is required to fulfil. Singling a particular aspect out, like tension distribution in this study,

is generally needed to be able to understand spider's web-building behaviour.

Chapter 6

Conclusions and Future work

The present doctoral thesis is about the work done to understand spider orb-web structures better in two ways. We try to understand an interesting aspect of its structure by asking a simple question, "Why do heavier spiders make webs with higher tension?" and finding a plausible answer. Additionally, we consider its hierarchical structure and try to implement that phenomenon in an engineering application, which is energy-absorbing lattices. The first chapters of this thesis are about introducing the field, both spiders and infill lattice designs, to the reader. Then, in Chapter 3, I compiled the resources and methods I needed to do my research to have a general view of finite element analysis. Some parts of it may come very basic to some researchers, especially the ones from engineering fields. However, coming from a physics background, all of those parts were something I had to learn (or relearn) in order to proceed with my research. After that, I delved into two very different, however in my perspective, very similar projects.

As I also mentioned in the introduction, I believe biomimicking should have two parts to it; we should first understand the organism (or biological structure) as well as we can so that we can use it to enhance our application, whatever it may be, a part of an aircraft or an algorithm to use in the developing of AI tools. We should be looking at the natural phenomena to understand its mechanics, and include more 'whys' instead of just 'hows'. In this sense, there should be more

going behind the scenes compared to a painter trying to paint directly the view in front of him/her.

The biological part of our project is about an observation done by perseverant researchers, which is the web thread tension increase caused by the spider's weight increase. We claim and show with our simulations that this phenomenon results from the spider's sensing ability, which the weight increase affects negatively if the thread tensions stay the same. We have published this work ([132]), and to the best of our knowledge, we are the first to explain this using state-of-the-art FEA techniques.

We also designed a new lattice to be used in energy absorption applications. For optimization, using black-box operations with beam models gives satisfactory results, as the simulation cost is relatively small compared to three-dimensional models. By using better and more detailed material models, we can also create a better fit for the experimental results. However, both have their place; beam models are required because of their low cost and fast run speeds, while three-dimensional models are more accurate. We plan to use the framework we developed here to design more advanced lattices.

This thesis started with a question we could not tackle with our current information: how do spiders make their web? This can then be used for answering (maybe) an even more challenging question, why are the spider web shapes the way they are?

So, hopefully, piece by piece, if it is meant to be, we will tackle these questions in the future. Nevertheless, we still need to answer many smaller questions, such as another aspect of the spider orb web, which is the spider's weight increase resulting in larger asymmetry. With the methods we have developed here, I believe that will be our next quest.

Bibliography

[1] A. Nazir, K. M. Abate, A. Kumar, and J.-Y. Jeng, "A state-of-the-art review on types, design, optimization, and additive manufacturing of cellular structures," *The International Journal of Advanced Manufacturing Technology*, vol. 104, pp. 3489–3510, 2019.

[2] W. Commons, "File:mammothterracetrees.jpg — wikimedia commons, the free media repository," 2022. [Online; accessed 27-November-2024].

[3] W. Commons, "File:sialis.lutaria.wing.detail.jpg — wikimedia commons, the free media repository," 2021. [Online; accessed 27-November-2024].

[4] W. Commons, "File:victoria amazonica back side.jpg — wikimedia commons, the free media repository," 2020. [Online; accessed 27-November-2024].

[5] F. Vollrath and P. Selden, "The role of behavior in the evolution of spiders, silks, and webs," *Annu. Rev. Ecol. Evol. Syst.*, vol. 38, no. 1, pp. 819–846, 2007.

[6] T. A. Blackledge, M. Kuntner, and I. Agnarsson, "The form and function of spider orb webs: evolution from silk to ecosystems," in *Advances in insect physiology*, vol. 41, pp. 175–262, Elsevier, 2011.

[7] F. Vollrath, "Strength and structure of spiders silks," *Reviews in Molecular Biotechnology*, vol. 74, no. 2, pp. 67–83, 2000.

[8] S. Zschokke, "Early stages of orb web construction in araneus diadematus clerck," *Rev Suisse Zool*, vol. 2, pp. 709–720, 1996.

[9] Y. Termonia, "Molecular modeling of spider silk elasticity," *Macromolecules*, vol. 27, no. 25, pp. 7378–7381, 1994.

[10] A. Soler and R. Zaera, "The secondary frame in spider orb webs: the detail that makes the difference," *Scientific reports*, vol. 6, no. 1, p. 31265, 2016.

[11] Z. Sun, Y. Guo, and V. Shim, "Deformation and energy absorption characteristics of additively-manufactured polymeric lattice structures—effects of cell topology and material anisotropy," *Thin-Walled Structures*, vol. 169, p. 108420, 2021.

[12] E. Bradford, A. M. Schweidtmann, and A. Lapkin, "Efficient multiobjective optimization employing gaussian processes, spectral sampling and a genetic algorithm," *Journal of global optimization*, vol. 71, no. 2, pp. 407–438, 2018.

[13] M. Güden, A. B. Riaz, A. K. Toksoy, M. Yıldıztekin, H. İ. Erten, G. Çimen, B. Hızlı, B. S. Çellek, E. Güleç, A. Taşdemirci, *et al.*, "Investigation and validation of the flow stress equation and damage model parameters of an electron beam melted ti6al4v alloy with a martensitic phase," *Materials Science and Engineering: A*, vol. 885, p. 145590, 2023.

[14] G. G. Kerr, H. F. Nahrung, A. Wiegand, J. Kristoffersen, P. Killen, C. Brown, and J. Macdonald, "Mechanical properties of silk of the australian golden orb weavers nephila pilipes and nephila plumipes," *Biology Open*, vol. 7, no. 2, p. bio029249, 2018.

[15] N. Tew and T. Hesselberg, "The effect of wind exposure on the web characteristics of a tetragnathid orb spider," *Journal of insect behavior*, vol. 30, pp. 273–286, 2017.

[16] E. Wirth and F. G. Barth, "Forces in the spider orb web," *Journal of Comparative Physiology A*, vol. 171, pp. 359–371, 1992.

[17] M. Kranz, J. K. Lüdeker, and B. Kriegesmann, "An empirical study on stress-based fail-safe topology optimization and multiple load path design," *Structural and multidisciplinary optimization*, vol. 64, no. 4, pp. 2113–2134, 2021.

[18] H. Altenbach and A. Öchsner, *Cellular and porous materials in structures and processes*, vol. 521. Springer Science & Business Media, 2011.

[19] E. Uribe-Lam, C. D. Treviño-Quintanilla, E. Cuan-Urquizo, and O. Olvera-Silva, "Use of additive manufacturing for the fabrication of cellular and lattice materials: a review," *Materials and Manufacturing Processes*, vol. 36, no. 3, pp. 257–280, 2021.

[20] A. Michael F., E. Tony, F. NA, H. J.W., W. H.N.G., and G. L. J., *Metal Foams: A Design Guide.* Butterworth-Heinemann, 2000.

[21] A. G. Evans, J. W. Hutchinson, N. A. Fleck, M. Ashby, and H. Wadley, "The topological design of multifunctional cellular metals," *Progress in materials science*, vol. 46, no. 3-4, pp. 309–327, 2001.

[22] X. Yu, L. Pan, J. Chen, X. Zhang, and P. Wei, "Experimental and numerical study on the energy absorption abilities of trabecular–honeycomb biomimetic structures inspired by beetle elytra," *Journal of Materials Science*, vol. 54, no. 3, pp. 2193–2204, 2019.

[23] A. Mao, N. Zhao, Y. Liang, and H. Bai, "Mechanically efficient cellular materials inspired by cuttlebone," *Advanced Materials*, vol. 33, no. 15, p. 2007348, 2021.

[24] X. An and H. Fan, "Hybrid design and energy absorption of luffa-sponge-like hierarchical cellular structures," *Materials & Design*, vol. 106, pp. 247–257, 2016.

[25] N. H. M. Bern, "World spider catalog (2024)," 2024. `http://wsc.nmbe.ch` [Accessed: (01.10.2024)].

[26] R. Foelix, *Biology of spiders*. Oxford university press, 2010.

[27] W. Eberhard, *Spider Webs: Behavior, Function, and Evolution*. University of Chicago Press, 12 2020.

[28] P. E. Cushing, *Spiders (Arachnida: Araneae)*. Dordrecht: Springer Netherlands, 2008.

[29] F. Vollrath, "Biology of spider silk," *International Journal of Biological Macromolecules*, vol. 24, no. 2, pp. 81–88, 1999.

[30] I. Agnarsson, A. Dhinojwala, V. Sahni, and T. A. Blackledge, "Spider silk as a novel high performance biomimetic muscle driven by humidity," *Journal of Experimental Biology*, vol. 212, pp. 1990–1994, 07 2009.

[31] I. Agnarsson, M. Kuntner, and T. A. Blackledge, "Bioprospecting finds the toughest biological material: extraordinary silk from a giant riverine orb spider," *PloS one*, vol. 5, no. 9, p. e11234, 2010.

[32] S. W. Cranford, A. Tarakanova, N. M. Pugno, and M. J. Buehler, "Nonlinear material behaviour of spider silk yields robust webs," *Nature*, vol. 482, no. 7383, pp. 72–76, 2012.

[33] D. De Tommasi, G. Puglisi, and G. Saccomandi, "Damage, self-healing, and hysteresis in spider silks," *Biophysical journal*, vol. 98, no. 9, pp. 1941–1948, 2010.

[34] H. M. Peters and J. Kovoor, "The silk-producing system of linyphia triangularis (araneae, linyphiidae) and some comparisons with araneidae: structure, histochemistry and function," *Zoomorphology*, vol. 111, pp. 1–17, 1991.

[35] A. T. Sensenig, K. A. Lorentz, S. P. Kelly, and T. A. Blackledge, "Spider orb webs rely on radial threads to absorb prey kinetic energy," *Journal of the Royal Society Interface*, vol. 9, no. 73, pp. 1880–1891, 2012.

[36] M. Kuntner, J. A. Coddington, and G. Hormiga, "Phylogeny of extant nephilid orb-weaving spiders (araneae, nephilidae): testing morphological and ethological homologies," *Cladistics*, vol. 24, no. 2, pp. 147–217, 2008.

[37] S. Zschokke *et al.*, "Form and function of the orb-web," *European arachnology*, vol. 19, p. 99, 2000.

[38] A. a. Rhisiart and F. Vollrath, "Design features of the orb web of the spider, araneus diadematus," *Behavioral Ecology*, vol. 5, no. 3, pp. 280–287, 1994.

[39] M. Kuntner, M. Gregorič, and D. Li, "Mass predicts web asymmetry in nephila spiders," *Naturwissenschaften*, vol. 97, pp. 1097–1105, 2010.

[40] W. G. Eberhard, "Function and phylogeny of spider webs," *Annual review of Ecology and Systematics*, vol. 21, no. 1, pp. 341–372, 1990.

[41] W. G. Eberhard, "The rare large prey hypothesis for orb web evolution: a critique," *The Journal of Arachnology*, vol. 41, no. 1, pp. 76–80, 2013.

[42] J. Oja and A. Koppel, *Continuum Mechanics.* Nova Science Publishers, Inc, 2010.

[43] A. Bower, "Applied mechanics of solids," 2009.

[44] Hibbitt, Karlsson, and Sorensen, *ABAQUS: Theory manual*, vol. 2. Hibbitt, Karlsson & Sorensen, 1997.

[45] Hibbitt, Karlsson, and Sorensen, *ABAQUS/standard: User's Manual*, vol. 1. Hibbitt, Karlsson & Sorensen, 1997.

[46] Hibbitt, Karlsson, and Sorensen, *ABAQUS/Explicit: user's manual*, vol. 1. Hibbitt, Karlsson and Sorenson Incorporated, 1998.

[47] H. M. Hilber and T. J. Hughes, "Collocation, dissipation and [overshoot] for time integration schemes in structural dynamics," *Earthquake Engineering & Structural Dynamics*, vol. 6, no. 1, pp. 99–117, 1978.

[48] U. Zerbst and M. Madia, "Analytical flaw assessment," *Engineering Fracture Mechanics*, vol. 187, pp. 316–367, 2018. SI: 50th Anniversary Issue.

[49] J. Hancock and A. Mackenzie, "On the mechanisms of ductile failure in high-strength steels subjected to multi-axial stress-states," *Journal of the Mechanics and Physics of Solids*, vol. 24, no. 2-3, pp. 147–160, 1976.

[50] S. Liu and Y. C. Shin, "Additive manufacturing of ti6al4v alloy: A review," *Materials & Design*, vol. 164, p. 107552, 2019.

[51] E. Uhlmann, R. Kersting, T. B. Klein, M. F. Cruz, and A. V. Borille, "Additive manufacturing of titanium alloy for aircraft components," *Procedia CIRP*, vol. 35, pp. 55–60, 2015. MIC2015 â€“ 15th Machining Innovations Conference for Aerospace Industry.

[52] P. Singh, H. Pungotra, and N. S. Kalsi, "On the characteristics of titanium alloys for the aircraft applications," *Materials Today: Proceedings*, vol. 4, no. 8, pp. 8971–8982, 2017. International Conference on Advancements in Aeromechanical Materials for Manufacturing (ICAAMM-2016): Organized by MLR Institute of Technology, Hyderabad, Telangana, India.

[53] R. Boyer, "An overview on the use of titanium in the aerospace industry," *Materials Science and Engineering: A*, vol. 213, no. 1, pp. 103–114, 1996. International Symposium on Metallurgy and Technology of Titanium Alloys.

[54] S. A. Salihu, Y. Suleiman, A. Eyinavi, and A. Usman, "Classification, properties and applications of titanium and its alloys used in aerospace, automotive, biomedical and marine industry-a review," *Int. J. Precious Eng. Res. Appl.*, vol. 4, pp. 23–36, 2019.

[55] C. Cui, B. Hu, L. Zhao, and S. Liu, "Titanium alloy production technology, market prospects and industry development," *Materials & Design*, vol. 32, no. 3, pp. 1684–1691, 2011.

[56] G. R. Johnson and W. H. Cook, "A constitutive model and data for metals subjected to large strains, high strain rates and high temperatures," in *Proceedings of the 7th International Symposium on Ballistics*, p. 541 547, 1983.

[57] G. R. Johnson and W. H. Cook, "Fracture characteristics of three metals subjected to various strains, strain rates, temperatures and pressures," *Engineering fracture mechanics*, vol. 21, no. 1, pp. 31–48, 1985.

[58] J. F. Marko and E. D. Siggia, "Stretching dna," *Macromolecules*, vol. 28, no. 26, pp. 8759–8770, 1995.

[59] J. Zhang, H. Huang, G. Liu, H. Zong, and C. Zhang, "Stiffness and energy absorption of additive manufactured hybrid lattice structures," *Virtual and Physical Prototyping*, vol. 16, no. 4, pp. 428–443, 2021.

[60] Z. Sun, Y. Guo, and V. Shim, "Characterisation and modeling of additively-manufactured polymeric hybrid lattice structures for energy absorption," *International Journal of Mechanical Sciences*, vol. 191, p. 106101, 2021.

[61] L. Cheng, J. Liu, and A. C. To, "Concurrent lattice infill with feature evolution optimization for additive manufactured heat conduction design," *Structural and Multidisciplinary optimization*, vol. 58, pp. 511–535, 2018.

[62] N. Lebaal, A. SettaR, S. Roth, and S. Gomes, "Conjugate heat transfer analysis within in lattice-filled heat exchanger for additive manufacturing," *Mechanics of Advanced Materials and Structures*, vol. 29, no. 10, pp. 1361–1369, 2022.

[63] W. Jiang, G. Yin, L. Xie, and M. Yin, "Multifunctional 3d lattice metamaterials for vibration mitigation and energy absorption," *International Journal of Mechanical Sciences*, vol. 233, p. 107678, 2022.

[64] H. Li, Y. Hu, J. Chen, D. Shou, and B. Li, "Lightweight meta-lattice sandwich panels for remarkable vibration mitigation: Analytical prediction, numerical analysis and experimental validations," *Composites Part A: Applied Science and Manufacturing*, vol. 163, p. 107218, 2022.

[65] J. Liu, H. Ou, J. He, and G. Wen, "Topological design of a lightweight sandwich aircraft spoiler," *Materials*, vol. 12, no. 19, p. 3225, 2019.

[66] J. Corona-Castuera, D. Rodriguez-Delgado, J. Henao, J. C. Castro-Sandoval, and C. A. Poblano-Salas, "Design and fabrication of a customized partial hip prosthesis employing ct-scan data and lattice porous structures," *ACS omega*, vol. 6, no. 10, pp. 6902–6913, 2021.

[67] B. Aslan and A. R. Yıldız, "Optimum design of automobile components using lattice structures for additive manufacturing," *Materials testing*, vol. 62, no. 6, pp. 633–639, 2020.

[68] M. F. Ashby and L. J. Gibson, "Cellular solids: structure and properties," *Press Syndicate of the University of Cambridge, Cambridge, UK*, pp. 175–231, 1997.

[69] S. Li, Q. Xu, Z.-b. Wang, W. Hou, Y. Hao, R. Yang, and L. Murr, "Influence of cell shape on mechanical properties of ti–6al–4v meshes fabricated by electron beam melting method," *Acta biomaterialia*, vol. 10, no. 10, pp. 4537–4547, 2014.

[70] H. D. Carlton, J. Lind, M. C. Messner, N. A. Volkoff-Shoemaker, H. S. Barnard, N. R. Barton, and M. Kumar, "Mapping local deformation behavior in single cell metal lattice structures," *Acta Materialia*, vol. 129, pp. 239–250, 2017.

[71] V. Crupi, E. Kara, G. Epasto, E. Guglielmino, and H. Aykul, "Static behavior of lattice structures produced via direct metal laser sintering technology," *Materials & Design*, vol. 135, pp. 246–256, 2017.

[72] J. Ye, Z. Sun, Y. Ding, Y. Zheng, and F. Zhou, "The deformation mechanism, energy absorption behavior and optimal design of vertical-reinforced lattices," *Thin-Walled Structures*, vol. 190, p. 110988, 2023.

[73] H. Zhong, T. Song, C. Li, R. Das, J. Gu, and M. Qian, "Understanding the superior mechanical properties of hollow-strut metal lattice materials," *Scripta Materialia*, vol. 228, p. 115341, 2023.

[74] X. Cao, S. Duan, J. Liang, W. Wen, and D. Fang, "Mechanical properties of an improved 3d-printed rhombic dodecahedron stainless steel lattice structure of variable cross section," *International Journal of Mechanical Sciences*, vol. 145, pp. 53–63, 2018.

[75] L. Bai, C. Yi, X. Chen, Y. Sun, and J. Zhang, "Effective design of the graded strut of bcc lattice structure for improving mechanical properties," *Materials*, vol. 12, no. 13, p. 2192, 2019.

[76] X. Guo, X. Li, E. Wang, J. Y. Fuh, W. F. Lu, and W. Zhai, "Bioinspired hierarchical diamond triply periodic minimal surface lattices with high energy absorption and damage tolerance," *Additive Manufacturing*, vol. 76, p. 103792, 2023.

[77] M. Denny, "The physical properties of spider's silk and their role in the design of orb-webs," *Journal of Experimental Biology*, vol. 65, no. 2, pp. 483–506, 1976.

[78] S. Zschokke, "Nomenclature of the orb-web," *The Journal of Arachnology*, vol. 27, no. 2, pp. 542–546, 1999.

[79] J. M. Gosline, P. Guerette, C. Ortlepp, and K. Savage, "The mechanical design of spider silks: from fibroin sequence to mechanical function," *Journal of Experimental Biology*, vol. 202, no. 23, pp. 3295–3303, 1999.

[80] L. Lin and W. Sobek, "Structural hierarchy in spider webs and spiderweb-type systems," *Structural Engineer*, vol. 76, pp. 59–64, 1998.

[81] J. Miltz and O. Ramon, "Energy absorption characteristics of polymeric foams used as cushioning materials," *Polymer Engineering & Science*, vol. 30, no. 2, pp. 129–133, 1990.

[82] A. Urbańczyk, J. Wright, D. Cowden, I. T. Solutions, H. Y. ÖZDERYA, M. Boyd, B. Agostini, M. Greminger, J. Buchanan, cactrot, huskier, M. S. de León Peque, P. Boin, W. Saville, B. Weissinger, Ruben, nopria, C. Osterwood, moeb, A. Kono, HLevering, W. Turner, A. Trhoň, G. Christoforo, just georgeb, A. Peterson, A. Grunichev, A. Gregg-Smith, Bernhard, and D. Anderson, "Cadquery/cadquery: Cadquery 2.1," Feb. 2021.

[83] S. P. Santosa, T. Wierzbicki, A. G. Hanssen, and M. Langseth, "Experimental and numerical studies of foam-filled sections," *International journal of impact engineering*, vol. 24, no. 5, pp. 509–534, 2000.

[84] A. Prior, "Applications of implicit and explicit finite element techniques to metal forming," *Journal of Materials Processing Technology*, vol. 45, no. 1, pp. 649–656, 1994.

[85] F. Habib, P. Iovenitti, S. Masood, and M. Nikzad, "Fabrication of polymeric lattice structures for optimum energy absorption using multi jet fusion technology," *Materials & Design*, vol. 155, pp. 86–98, 2018.

[86] C. Ling, A. Cernicchi, M. D. Gilchrist, and P. Cardiff, "Mechanical behaviour of additively-manufactured polymeric octet-truss lattice structures under quasi-static and dynamic compressive loading," *Materials & Design*, vol. 162, pp. 106–118, 2019.

[87] R. Gümrük and R. Mines, "Compressive behaviour of stainless steel micro-lattice structures," *International Journal of Mechanical Sciences*, vol. 68, pp. 125–139, 2013.

[88] G. Labeas and M. Sunaric, "Investigation on the static response and failure process of metallic open lattice cellular structures," *Strain*, vol. 46, no. 2, pp. 195–204, 2010.

[89] M. Smith, Z.-w. Guan, and W. Cantwell, "Finite element modelling of the compressive response of lattice structures manufactured using the selective laser melting technique," *International Journal of Mechanical Sciences*, vol. 67, pp. 28–41, 2013.

[90] M. H. Luxner, J. Stampfl, and H. E. Pettermann, "Finite element modeling concepts and linear analyses of 3d regular open cell structures," *Journal of Materials science*, vol. 40, pp. 5859–5866, 2005.

[91] B. Paygozar and R. M. Gorguluarslan, "Improving the energy absorption capacity of bending-dominated additively manufactured polylactic acid (pla) lattices," *Mechanics of Advanced Materials and Structures*, pp. 1–20, 2023.

[92] M. Saleh, S. Anwar, A. M. Al-Ahmari, and A. Alfaify, "Compression performance and failure analysis of 3d-printed carbon fiber/pla composite tpms lattice structures," *Polymers*, vol. 14, no. 21, p. 4595, 2022.

[93] A. Aldoshan and S. Khanna, "Effect of relative density on the dynamic compressive behavior of carbon nanotube reinforced aluminum foam," *Materials Science and Engineering: A*, vol. 689, pp. 17–24, 2017.

[94] S.-f. Fan, T. Zhang, Y. Kun, H.-j. Fang, H.-q. Xiong, Y.-l. Dai, D.-y. JIANG, H.-l. ZHU, *et al.*, "Compressive properties and energy absorption characteristics of open-cell nickel foams," *Transactions of Nonferrous Metals Society of China*, vol. 27, no. 1, pp. 117–124, 2017.

[95] B. Xie, Y. Fan, T. Mu, and B. Deng, "Fabrication and energy absorption properties of titanium foam with cacl2 as a space holder," *Materials Science and Engineering: A*, vol. 708, pp. 419–423, 2017.

[96] P. Wang, F. Yang, P. Li, W. Zhang, G. Lu, and H. Fan, "Bio-inspired vertex modified lattice with enhanced mechanical properties," *International Journal of Mechanical Sciences*, vol. 244, p. 108081, 2023.

[97] S. Yuan, C. K. Chua, and K. Zhou, "3d-printed mechanical metamaterials with high energy absorption," *Advanced Materials Technologies*, vol. 4, no. 3, p. 1800419, 2019.

[98] J. J. Andrew, J. Schneider, J. Ubaid, R. Velmurugan, N. Gupta, and S. Kumar, "Energy absorption characteristics of additively manufactured plate-lattices under low-velocity impact loading," *International Journal of Impact Engineering*, vol. 149, p. 103768, 2021.

[99] I. Maskery, N. T. Aboulkhair, A. Aremu, C. Tuck, and I. Ashcroft, "Compressive failure modes and energy absorption in additively manufactured double gyroid lattices," *Additive Manufacturing*, vol. 16, pp. 24–29, 2017.

[100] S. Y. Choy, C.-N. Sun, K. F. Leong, and J. Wei, "Compressive properties of functionally graded lattice structures manufactured by selective laser melting," *Materials & Design*, vol. 131, pp. 112–120, 2017.

[101] X. Zhang, J. Yao, B. Liu, J. Yan, L. Lu, Y. Li, H. Gao, and X. Li, "Three-dimensional high-entropy alloy–polymer composite nanolattices that overcome the strength–recoverability trade-off," *Nano letters*, vol. 18, no. 7, pp. 4247–4256, 2018.

[102] J. Mueller, J. R. Raney, K. Shea, and J. A. Lewis, "Architected lattices with high stiffness and toughness via multicore–shell 3d printing," *Advanced Materials*, vol. 30, no. 12, p. 1705001, 2018.

[103] Y. Alvandi-Tabrizi and A. Rabiei, "Use of composite metal foam for improving absorption of collision forces," *Procedia Materials Science*, vol. 4, pp. 377–382, 2014.

[104] Q. JC, X. ZP, W. JY, and Z. JL, "Compressive property and energy absorption of porous sintered fiber metals," *Materials transactions*, vol. 49, no. 12, pp. 2919–2921, 2008.

[105] L. Stanev, B. Drenchev, A. Yotov, and R. Lazarova, "Compressive properties and energy absorption behaviour of alsi10mg open-cell foam," *J. Mater. Sci. Technol*, vol. 22, no. 1, pp. 44–53, 2014.

[106] M. J. Al Rifaie, "Resilience and toughness behavior of 3d-printed polymer lattice structures: Testing and modeling," Master's thesis, Wright State University, 2017.

[107] S. Kumar, B. L. Wardle, M. F. Arif, and J. Ubaid, "Stress reduction of 3d printed compliance-tailored multilayers," *Advanced Engineering Materials*, vol. 20, no. 1, p. 1700883, 2018.

[108] B. Fan, Z. Xu, Y. Lin, and Z. Huang, "Mechanical properties of a novel two-phase hybrid plate-lattice metamaterial," *Mechanics of Advanced Materials and Structures*, vol. 30, no. 23, pp. 4752–4763, 2023.

[109] D. Sharma and S. S. Hiremath, "Experimental and fem study on the in-plane and out-plane loaded reversible dual-material bio-inspired lattice structures with improved energy absorption performance," *Composite Structures*, vol. 303, p. 116353, 2023.

[110] A. S. French, P. H. Torkkeli, and E.-A. Seyfarth, "From stress and strain to spikes: mechanotransduction in spider slit sensilla," *Journal of Comparative Physiology A*, vol. 188, pp. 739–752, 2002.

[111] C. F. Schaber, S. N. Gorb, and F. G. Barth, "Force transformation in spider strain sensors: white light interferometry," *Journal of the Royal Society Interface*, vol. 9, no. 71, pp. 1254–1264, 2012.

[112] D. Klärner and F. G. Barth, "Vibratory signals and prey capture in orb-weaving spiders (zygiella x-notata, nephila clavipes; araneidae)," *Journal of comparative physiology*, vol. 148, pp. 445–455, 1982.

[113] W. M. Masters, "Vibrations in the orbwebs of nuctenea sclopetaria (araneidae) i. transmission through the web," *Behavioral ecology and sociobiology*, vol. 15, pp. 207–215, 1984.

[114] M. Landolfa and F. Barth, "Vibrations in the orb web of the spider nephila clavipes: cues for discrimination and orientation," *Journal of Comparative Physiology A*, vol. 179, pp. 493–508, 1996.

[115] B. Mortimer, A. Soler, L. Wilkins, and F. Vollrath, "Decoding the locational information in the orb web vibrations of araneus diadematus and zygiella x-notata," *Journal of the Royal Society Interface*, vol. 16, no. 154, p. 20190201, 2019.

[116] A. W. Otto, D. O. Elias, and R. L. Hatton, "Modeling transverse vibration in spider webs using frequency-based dynamic substructuring," in *Dynamics of Coupled Structures, Volume 4: Proceedings of the 36th IMAC, A Conference and Exposition on Structural Dynamics 2018*, pp. 143–155, Springer, 2018.

[117] A. Morassi, A. Soler, and R. Zaera, "A continuum membrane model for small deformations of a spider orb-web," *Mechanical Systems and Signal Processing*, vol. 93, pp. 610–633, 2017.

[118] R. Zaera, Ó. Serrano, J. Fernández-Sáez, and A. Morassi, "Eco-localization of a prey in a spider orb web," *Journal of Vibration and Control*, vol. 28, no. 11-12, pp. 1229–1238, 2022.

[119] P. N. Witt, C. F. Reed, D. B. Peakall, P. N. Witt, C. F. Reed, and D. B. Peakall, "Construction of the web," *A Spider s Web: Problems in Regulatory Biology*, pp. 74–93, 1968.

[120] R. Milo, P. Jorgensen, U. Moran, G. Weber, and M. Springer, "Bionumbers the database of key numbers in molecular and cell biology," *Nucleic acids research*, vol. 38, no. suppl_1, pp. D750–D753, 2010.

[121] A. E. Wignall, R. R. Jackson, R. S. Wilcox, and P. W. Taylor, "Exploitation of environmental noise by an araneophagic assassin bug," *Animal behaviour*, vol. 82, no. 5, pp. 1037–1042, 2011.

[122] J. Zanker and K. Götz, "The wing beat of drosophila melanogaster. ii. dynamics," *Philosophical Transactions of the Royal Society of London. B, Biological Sciences*, vol. 327, no. 1238, pp. 19–44, 1990.

[123] C. Frohlich and R. E. Buskirk, "Transmission and attenuation of vibration in orb spider webs," *Journal of Theoretical Biology*, vol. 95, no. 1, pp. 13–36, 1982.

[124] T. Watanabe, "Web tuning of an orb-web spider, octonoba sybotides, regulates prey-catching behaviour," *Proceedings of the Royal Society of London. Series B: Biological Sciences*, vol. 267, no. 1443, pp. 565–569, 2000.

[125] K. Nakata, "Attention focusing in a sit-and-wait forager: a spider controls its prey-detection ability in different web sectors by adjusting thread tension," *Proceedings of the Royal Society B: Biological Sciences*, vol. 277, no. 1678, pp. 29–33, 2010.

[126] K. Nakata and S. Zschokke, "Upside-down spiders build upside-down orb webs: web asymmetry, spider orientation and running speed in cyclosa," *Proceedings of the Royal Society B: Biological Sciences*, vol. 277, no. 1696, pp. 3019–3025, 2010.

[127] S. Zschokke and K. Nakata, "Vertical asymmetries in orb webs," *Biological Journal of the Linnean Society*, vol. 114, pp. 659–672, 02 2015.

[128] F. Vollrath, W. J. Fairbrother, R. J. Williams, E. K. Tillinghast, D. T. Bernstein, K. S. Gallagher, and M. A. Townley, "Compounds in the droplets of the orb spider's viscid spiral," *Nature*, vol. 345, no. 6275, pp. 526–528, 1990.

[129] D. T. Edmonds and F. Vollrath, "The contribution of atmospheric water vapour to the formation and efficiency of a spider s capture web," *Proceedings of the Royal Society of London. Series B: Biological Sciences*, vol. 248, no. 1322, pp. 145–148, 1992.

[130] M. Tarsitano and W. H. Kirchner, "Vibrational courtship signals of zygiella x-notata (clerck)(araneae: Araneidae)," *BULLETIN-BRITISH ARACHNOLOGICAL SOCIETY*, vol. 12, no. 1, pp. 26–31, 2001.

[131] M. Anotaux, C. Toscani, R. Leborgne, N. Châline, and A. Pasquet, "Aging and foraging efficiency in an orb-web spider," *Journal of ethology*, vol. 32, pp. 155–163, 2014.

[132] K. Yavuz, A. M. Soler, R. Zaera, and S. Jahangirov, "Effect of spider's weight on signal transmittance in vertical orb webs," *Royal Society Open Science*, vol. 11, no. 10, p. 240986, 2024.